"Structural Health Monitoring of Fatigue Cracks using Acoustic Emission Technique"

Doctor of Philosophy

Department of Mechanical, Aerospace and Civil Engineering

Mohd Fairuz bin Shamsudin

2019

ABSTRACT

In the oil and gas industry, failure due to vibration-induced fatigue is considered as an important cause of loss of integrity. There have been increasing incidents of vibration-induced fatigue in pipelines both in offshore and onshore petrochemical plants. To mitigate this problem, a Structural Health Monitoring (SHM) method using Acoustic Emission (AE) was developed, using specific damage identification strategies. A number of contributions are highlighted in this research work, which includes the fundamental understanding of wave propagation in thick and thin structures. The application of Rayleigh waves and Lamb waves is important in damage identification, being demonstrated in experimental works and finite element analysis (FEA). The identification of damage by vibration-induced fatigue crack demands a dedicated instrumentation and signal processing techniques. A novel method using Bayesian estimation of the effective coefficient (EC) was introduced, which measure the uncertainties of the located events measured by AE technique, calibrated using the information derived from pencil lead break tests. The EC was formulated in such a way the AE signals from each sensor were cross-correlated and the calculated coefficients were corrected taking into account the minimum coefficients from each sensor combination. Cross-correlation was then used to improve the identification of Lamb waves generated by the crack development. The calculated time difference between the fundamental wave modes increases the accuracy of the located events using a Single Sensor Modal Analysis Localization technique (SSMAL). Using a similar approach, the ratio of symmetric (S0) and asymmetric waves (A0) amplitudes was determined and used for damage extent assessments. In summary the AE is shown to be a very effective method for SHM of vibration-induced fatigue damage.

ACKNOWLEDGMENT

ٱلْـحَـمْـدُ للهِ

I am grateful to be given the strength and patience while doing this research and completed this thesis. Special thanks to my mother who always keeps me motivated whenever I am facing difficulties. I would like to thank my wife for her personal support and great patience. This achievement would not have been possible without her enormous sacrifices. I would like to express my sincere gratitude to my principal supervisor **Dr. Cristinel Mares** for his continuous support and guidance. I gained immense knowledge through his supervision. I wish to express my sincere gratitude to my academic supervisor, **Professor Tat-Hean Gan** for his great support and to my industrial supervisor, **Graham Edwards** for sharing his expertise and knowledge from the industrial perspectives. Lastly, I am thankful to Majlis Amanah Rakyat (MARA), Brunel University London and National Structure Integrity Research Centre (NSIRC) for their financial support.

ACRONYMS

AE	Acoustic Emission
BMA	Bayesian Model Averaging
BN	Bayesian Network
CWT	Continuous Wavelet Transform
DWT	Discrete Wavelet Transform
EC	Effective Coefficient
EI	Energy Institute
FRF	Frequency Response Function
HCR	Hydrocarbon Release
HSE	Health and Safety Executive
IQR	Interquartile Range
LOF	Likelihood of Failure
MAE	Modal Acoustic Emission
MFC	Micro Fibre Composite
MCMC	Markov chain Monte Carlo
NDE	Non-Destructive Evaluation
NDT	Non-Destructive Testing
PLB	Pencil Lead Break
POD	Probability of Detection
PVDF	Polyvinylidene Fluoride
QRA	Quantified Risk Assessment
RMS	Root Mean Square
SIF	Stress Intensity Factor
SBC	Small Bore Connection
SHM	Structural Health Monitoring
SG	Strain Gauge
SSMAL	Single Sensor Modal Analysis

TOA	Time of Arrival
TWI	Technology Welding Institute
WT	Wavelet Transform

NOMENCLATURE

V	Wave speed [m/s]
θ	Angle [°]
dti	The arrival time difference [s]
v_g	Group velocity [m/s]
N′	AE count rate [AE count/cycle]
a′	Crack growth rate [mm/cycle]
ΔK	Stress intensity factor [MPa$\sqrt{\text{m}}$]
ρ_0	Material density [kg/m^3]
a_i	Acceleration of infinitesimal cubic element [m/s^2]
u_i	Displacement of infinitesimal cubic element [m]
x_j	Principal coordinate system
σ_{ij}	Stress tensor
c_{ijkl}	Elastic tensor
ε_{ij}	Strain tensor
k	Wave number [m^{-1}]
ω	Angular frequency [rad/s]
m	Axial nodal pattern
n	Circumferential nodal pattern
g	Gravity [m/s^2]
t	Discrete time of the signals [s]
f	Wave frequency [s^{-1}]
σ	Standard deviation
ϕ_{xy}	The correlation function
$\psi_{a,b}$	Wavelet basis function
τ	Time lag [s]
$\bar{\phi}_{i,j}$	Cross correlation coefficient of signals i and j

TABLE OF CONTENTS

LIST OF FIGURES

LIST OF TABLES

CHAPTER 1

INTRODUCTION

In the oil and gas industry, failure due to vibration-induced fatigue has recently been identified as a potential threat. There have been increasing incidents of vibration-induced fatigue in piping systems both in offshore and onshore petrochemical plants. The Health and Safety Executive (HSE) reported that 21% of the hydrocarbon releases in terms of "immediate cause" for offshore process plants in the North Sea were caused by vibration-induced fatigue [1]. Figure 1-1 shows historical data for number of incidents associated with hydrocarbon releases reported by the HSE [2].

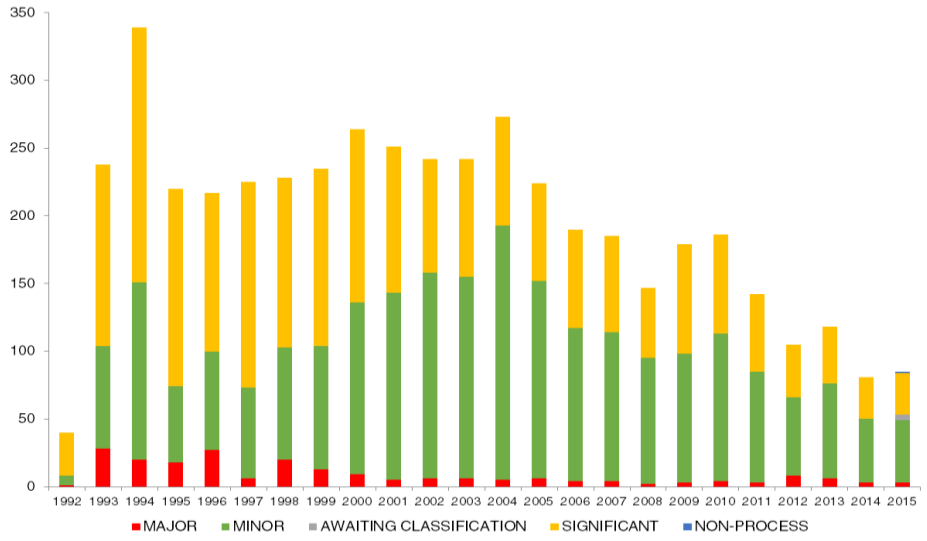

Figure 1-1 Shows histogram of hydrocarbon releases (HCR) database reported by the HSE [2].

Process piping is normally designed on the basis of static analysis without taking into account operational condition. Mitigation of vibration problems is normally considered on ad-hoc basis by reactive action following fatigue failure [3,4]. Incidents related to vibration are usually unforeseen; long-span onshore and subsea pipelines for example suffer fatigue without giving information about the impending failures [5–7]. A solution to this problem is to have a continuous monitoring system that can monitor critical

equipment over time. However, the implementation in operational conditions being complex and difficult, measurements being affected by noise, variations of environmental conditions, these aspects affecting the reliability of any SHM system.

1.1 MOTIVATION

The common causes of pipe vibration can be either direct or indirect. The direct mechanism is usually caused by internal or external fluid flows such as flow turbulence. The indirect mechanism is caused by transmission of vibration energy through pipe supports [3,4]. The main factors that contribute to fatigue failure are improper piping design such as unsupported small bore pipes and poor sizing [3], causing failure at pipe connections. Figure 1-2 shows an example of fatigue crack at pipe connection resulted from acoustic-induced vibration.

Figure 1-2 Fatigue crack due to acoustic induced vibration [8]

Fatigue failure is usually associated with repeated loadings. The impending failure is usually unpredictable such as the incident of Alexander Kielland platform located in the North Sea. The floating drill platform suffered from a fractured cross-brace securing the column, which resulted in overloading of the main column attachment. As a consequence, the column was broken apart from the main structures which caused the platform to collapse. The investigation discovered fractured braces resulting from small

weld cracks in the hydrophone attachment during fabrication. These caused the cracks to propagate gradually under wave loadings.

Figure 1-3 Alexander Kielland platform disaster in 1980 [9]

The consequence of vibration-induced fatigue failure in process piping can be catastrophic. Undetected hydrocarbon leaks may cause fire and explosion. Many factors need to be understood in order to predict fatigue failure. The prediction becomes more complex without knowing the loading condition, anticipated residual stresses, inclusion or defects. Baker and Descamps [10] suggested there should be an economical approach to account for a small probability of fatigue during service life, and continuously minimizing the likelihood of the undetected cracks. This effort requires continuous information over time which is not possible for scheduled inspection.

1.2 AIMS AND OBJECTIVES

The aim of this research work is to develop a structural health monitoring (SHM) technique for the assessment of damage caused by vibration-induced fatigue. The following three main objectives are considered in this project:

- Development of a Structural Health Monitoring method for detection and localization of damage caused by vibration induced fatigue.

- Development of robust approaches for Level 1 and 2 in SHM through signal processing methods taking into account the effect of environmental noise.
- Development of a technique for prediction of damage extent (Level 3, 4 of a SHM system).

1.3 RESEARCH OUTLINES & CHAPTERS SUMMARY

This thesis is structured as follows;

Chapter 2 reviews the past research works on damage identification methods. The theory and principle of fracture mechanics, structural health monitoring, elastic waves and acoustic emission technique for diagnostic and prognostic were studied.

Chapter 3 describes wave propagation in thin and thick structures by experimental approach. This chapter highlights the importance of Rayleigh wave and Lamb waves for detection and localization. The analysis involves wavelet transformation and cross correlation for wave modes decomposition. Linear and planar localization methods for locating acoustic emission sources were studied.

Chapter 4 demonstrates acoustic emission monitoring a resonant fatigue experiment of a pipe. The Acoustic Emission technique was used for detection and localization of fatigue cracks. The assessment involves comparison of Acoustic Emission features derived from with strain and vibration data. Uncertainties associated with localization errors were evaluated using Bayesian estimation. This chapter highlights the novelty of using Bayesian estimation to quantify source localization.

Chapter 5 demonstrates the design of an experiment of fatigue tests for plates and the use of a hybrid approach which involves vibration testing, crack modelling, and wave propagation analysis using Finite Element models for damage detection. The novelty of this approach is the development of a qualitative method for estimation of the damage extent using the analysis of Lamb waves. The damage extent is quantified by comparison

of the dynamics of a calibrated FE model with the experimental data measured for a set of damaged specimens at various crack depths.

Chapter 6 provides the conclusions and proposed future works.

CHAPTER 2

LITERATURE REVIEW

2.1 INTRODUCTION

This chapter provides a literature review and fundamental aspects supporting the current research. The main references used in this work are discussed together with pointers to the theoretical elements allowing understanding of these results.

2.2 STRUCTURAL DAMAGE MECHANISMS

Structural failure due to fatigue can be described from the theory of fracture mechanics. In general, there are three crack separation modes depending on the loading condition as illustrated in Figure 2-1.

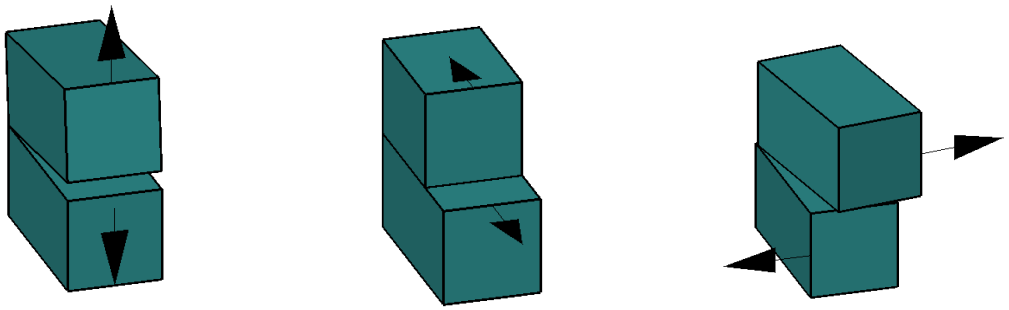

Mode I - Opening mode Mode II - Sliding mode Mode III -Tearing mode

Figure 2-1 Basic crack modes

In most engineering problems, failure due to cracks is not limited to the three independent modes. Often cracks propagate due to combination of modes (i.e. the so called mixed mode). However, mode I crack is considered the most dangerous, where crack can propagate rapidly and trigger brittle fracture. Therefore mode I has been

studied extensively in the published literature. The crack propagation is usually unpredictable and difficult to be detected.

2.3 VIBRATION TECHNIQUES FOR DAMAGE IDENTIFICATION

Vibration-based condition monitoring is commonly used for damage detection associated with vibration problems. In recent years, the demand for more accurate techniques to detect structural defects has been considerably increased due to the associated risk and consequences of structural failures in complex industrial systems. For this reason, early detection of damage is crucial to ensure safe, continuous and reliable operations. Typical vibration method evaluates structural condition through physical properties such as mass, stiffness and damping, or dynamic characteristics such as natural frequency, modal damping and mode shapes. These characteristics are measured by an array of sensors distributed over the structure. However to detect cracks, where the scale of damage is very small compared to the overall physical dimensions, can be difficult since the change of dynamic characteristics is insignificant. Variability in operating condition can also lead to measurement errors. There are number of guidelines and best practices available for the assessment of vibration in pipework. The most applicable for the oil and gas industry was published by the Energy Institute [3]. This guideline focuses on "through life" management that provides assistance for operators to develop their own management systems. The publication [4] was published in response to the growing number of pipework failure resulted from the greater use of thin pipework in new designed offshore and onshore installations. This guideline also provides a mathematical approach used to estimate the Likelihood of Failure (LOF) for mainline and small bore connection for screening purposes in proactive based assessment. The LOF can be determined using process parameters such as fluid density, flow rate etc. However, when such information is not available, the LOF is evaluated based on judgement which can be overly conservative. It shall be noted that LOF is not an absolute probability of failure. The process flow of the assessment is illustrated in Figure 2-2.

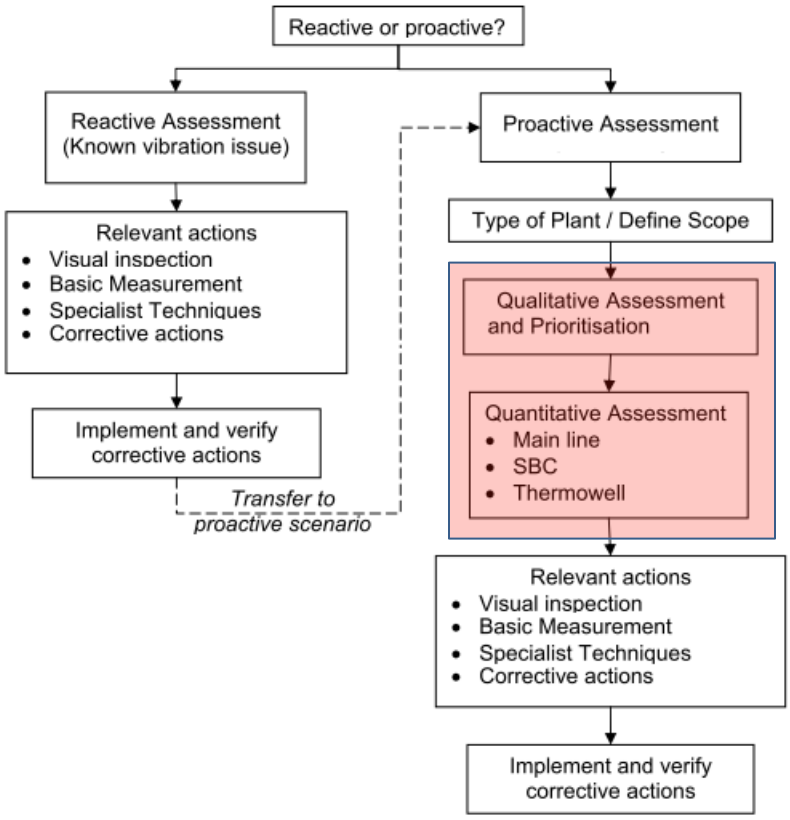

Figure 2-2 Process flow of vibration assessment [3]. The LOF is calculated under qualitative and quantitative assessment (highlighted in red).

The criteria for vibration assessment are defined differently according to each different measurement technique. The accuracy varies from visual inspection technique to highly accurate specialist technique. The basic measurement technique measures vibration velocity but limited to low frequency vibration problems. The assessment criteria for basic measurement are shown in Figure 2-3.

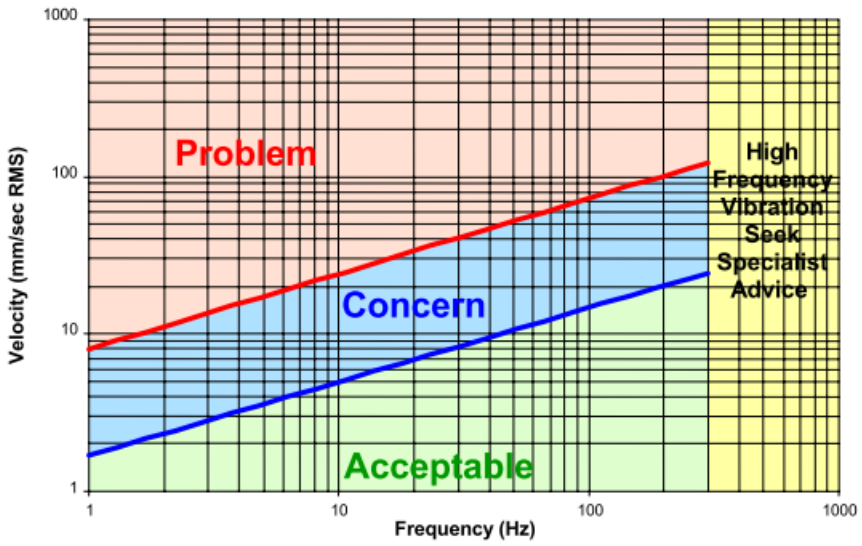

Figure 2-3 Vibration assessment criteria [3].

The major disadvantage of this measurement approach is that the fatigue failure is difficult to be predicted with confidence. The proposed solution to this problem is to measure the dynamic strain, but this can be insensitive to crack propagation if the scale of damage is small compared to the overall size of the structure. Therefore the course of action recommended by these guidelines is to develop specialised measurement and analysis methods allowing to robustly evaluating the severity of damage and the LOF.

2.4 STRUCTURAL HEALTH MONITORING (SHM)

In general, a Structural Health Monitoring (SHM) system focuses on damage identification and prediction through observation over time. The structural condition is evaluated using damage sensitive features derived from measurement with applications in all industrial fields; the aerospace industry, civil engineering, nuclear industry, and oil and gas. The use of SHM to detect damage is paramount as the technology becomes more advanced and cost effective. Example of their advantages in management of operational risk is illustrated by the following diagram which highlights the following elements:

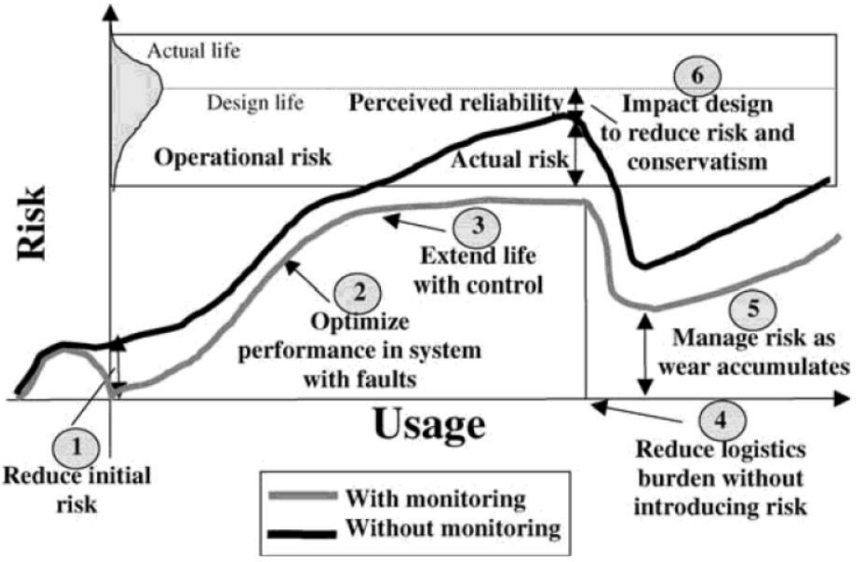

Figure 2-4 Benefits of system development and operation that can be realized using health and monitoring technology [11]

1) Reduced initial risk to operators and structural system using more systematic and accurate assessment
2) Performance optimisation through prognostics-driven control (e.g. smart system technology)
3) Reduced risk through life-extending operation and control based on the use of health monitoring information such early detection of crack
4) Reduced cost for servicing structural systems and logistics due to proper maintenance scheduling
5) Lower risk for after maintenance actions are taken (i.e. increase reliability)
6) Reduced design conservatism (i.e. reduce overall cost)

In the early 70's, SHM was considered very advanced and costly. However as the technology evolved, hardware and software are becoming more cost-effective, which makes SHM application viable. The state-of-the-art sensor technology such as wireless sensor embedded in laminated structures (i.e. smart system[1]) has become applicable to

[1] Smart system refers to a device or an array of devices that can sense changes in its environment and makes an optimal response.

many industries. The integration of such system with advanced digital signal processing, telemetry and computational algorithms provides unprecedented information about structural condition throughout their service life. One of the practical benefits of SHM over conventional non-destructive evaluation (NDE) techniques is that, SHM does not suffer from operation intervention that may lead to production loss. Detection can be achieved through systematic data collection and analysis by permanently installed sensor network. However an inherent associated problem is that each type of damage may have unique characteristics and hence interpretation of data requires a dedicated signal processing analysis and damage identification method in order to obtain meaningful results. NDE can be used for verification purposes when the location of damage is known, which complements the SHM techniques.

2.4.1 Overview of SHM

The research in structural health monitoring is very broad. A comprehensive review of damage identification and structural health monitoring from year 1968 to 1997 was presented by Doebling et al [12,13]. Sohn et al [14] continued the survey from 1996 – 2001. Carden and Fanning [15] reviewed until 2003. Fan and Qiao [16] made a comparative study in this research development until 2009. To date, there are many published papers in this research field presenting the development of state-of-the-art systems with extensive improvement in SHM reliability based on integration of statistical tools for probability of flaw detection etc. However to date there is no specific standard established for the SHM applications.

2.4.1.1 Local and Global Damage Identification

In general, the Structural Health Monitoring applications focus on “local” and “global” damage identification. “Local” in this context is meant by damage assessment from pre-determined locations. In contrast, “global” considers assessment of an entire system but the response is less sensitive to local changes. “Damage” is a comparison between two different states of a system: the initial (healthy) condition and the damaged condition [12]. Worden [17] emphasis on definition of damage taxonomically into *fault*, *damage*

and *defect*. A *fault* is regarded when a structure can no longer operate satisfactorily, *damage* is when a structure can no longer operate in ideal condition but still can function satisfactorily. *Defect* is inherent within materials. In practice, damage identification is carried out in conjunction with various methods which include SHM, condition monitoring and non-destructive evaluation. Doebling et al [12] classified structural damages into linear and non-linear, where for linear damage, a structure remains linear-elastic after damage occurs and the response can be modelled linearly. Non-linear damage is when linear-elastic becomes non-linear after damage is introduced. This problem is usually associated with fracture mechanics.

2.4.1.2 Feature Extraction

Generally, the features providing information on the state of the structures, can be categorized as parametric-based and signal-based [18]. For signal-based features, dedicated signal processing techniques are used which acquire parameters directly from a signal in time, frequency or time-frequency domain. These methods have been used by many researchers for linear and non-linear problems such as Auto-Regressive Model (AR) model and Auto-Regressive Moving Average (ARMA) model. The parametric-based uses explicit physical-dynamic parameters to evaluate the structural condition. Due to the large number of variables in analysis, statistical methods are considered the best option over deterministic approach allowing the quantification of uncertainty in measured data.

2.4.1.3 Model Updating based on Statistical methods

The principle behind model updating is minimizing errors between the predicted result and measured data [19]. Model updating is useful to predict structural response to disturbances. Updating model parameters are crucial and must be validated physically. Invalidated model with uncertainties in physical data, loading information, environment and operating conditions may result in modelling errors. Prediction by only a single calibration of model parameters does not provide high confidence level [20]. Therefore, the variability of parameters can be assessed by statistical framework either based on *frequency* or *degree of belief* [20]. The *frequency* approach is based upon maximum

likelihood or maximum conditional probability of the parameters with known random output, while the basis of *degree of belief* i.e. Bayesian theorem, is based on prior belief and this approach will be discussed in detail in the following sections.

2.4.2 Statistical Pattern Recognition

Statistical pattern recognition receives great attention owing to its suitability to account for large uncertainties and non-linearity of measurement data. According to Farrar et al [21], statistical pattern recognition consists of *supervised* and *unsupervised* learning. *Supervised* learning requires both the undamaged and damaged states to be known. The extracted features can be studied by classification or regression analysis. In *unsupervised* learning, the damage condition is unknown and hence the outliers of measurement have to be studied. This is useful to compare the current and past measurements. Statistical pattern recognition study involves operational evaluation, data condensation and cleansing. The method is actively used in damage detection, which involves assessment of features using different classes of patterns. Sohn et al [22] used statistical process control or known as "X-bar Control Chart", which provides a framework to identify the inconsistency of measurements i.e. damage sensitive features of the current and past measurements. The authors used the Auto Regressive (AR) technique to fit the measurements, a range of AR coefficients describing the initial state being compared with calculated AR coefficients. When outliers occur, a change of state is registered. Sohn et al [23], later extended the technique to take into account a two-stage time history prediction model, combining an auto-regressive (AR) model and an autoregressive with exogenous inputs (ARX) model. The sensitive features leading to residual errors were calculated between the current and predicted signals. The standard deviation of residual errors determines the proximity of damage location showing increased values for those sensors located near the damage locations. Sohn et al [24] also combined the AR – ARX model with neural network for data normalization to distinguish the effect of damage and environment upon the extracted features.

2.4.2.1 Bayesian Estimation

Bayes's theorem can be used for updating inspection data such as predicting flaw size overcoming the limitation of NDT devices [25]. In theory, Bayes's theorem is used to determine the *posterior*[2] distribution from a known *prior* distribution. The observed data or evidence is used to update the *prior* distribution. The *prior* such as crack density is updated as more data is collected. An example of distribution of detected cracks out of all cracks from a sample (i.e. crack density against flaw size) is illustrated in Figure 2-5. The general equation of Bayesian theorem is given as follows;

$$p(H|D) = \frac{p(D|H)p(H)}{p(D)} \tag{2-1}$$

$p(H)$ −Probability of the hypothesis before the data is seen, called *prior*
$P(H|D)$ −Probability of the the hypothesis after the data is seen, called *posterior*
$p(D)$ − Probability of data, called normalizing constant, to ensure $\sum p(H|D) = 1$
$P(D|H)$ − Probability of the data under hypothesis, called *likelihood*

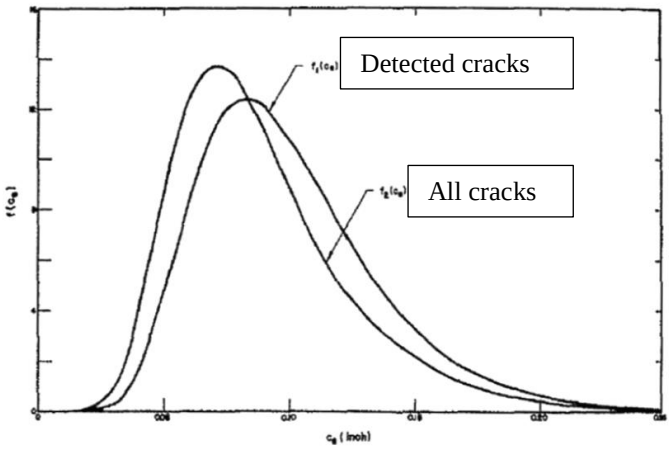

Figure 2-5 Comparison of crack depth distribution for the detected crack sample against the actual cracks [25]

[2] Posterior is a predictive distribution to account for the unobserved observations

In SHM, the Bayesian theorem is considered a promising tool for damage identification. Many random variables can be used in joint networks e.g. Bayesian Networks (BN) or finding the best model to represent the data by joint probability distributions over many hypotheses e.g. Bayesian Model Averaging (BMA). The advantage of Bayesian estimation is that it can alleviate diagnosis problems having large uncertainties of data and unwanted information such as noise from environment and hence, only the relevant signals are used for assessment. This method can prevent the two common diagnostic problems in damage identification i.e. *False Positive* and *False Negative* [21]. *False Positive* is defined when a system incorrectly identifies the structures to be damaged although it is actually healthy and hence leads to unnecessary follow up inspection or repairs. *False Negative* is when detection of damage is missed due to system error and hence, misses the subsequent damage developments. .

2.4.3 Structural Health Monitoring applications

For Piping or pipelines monitoring, an array of sensors are deployed at various locations along pipe axis. The sensors array must be arranged such that it covers critical locations. Piping configurations are usually consisting of many elements attached to main line such as fitting, valves, small bore connection (SBC), flanged and welded joints. Different materials or structures may have inherent flaws or defects that are not obvious prior to commission. Throughout the time, piping may experience various forms of damage such as fatigue or corrosion. These types of damage are usually accumulated for a long time period. Therefore monitoring of these pipes may not be feasible. However, damage could also occur in a relatively short time period such as sudden rupture during hydrostatic test[3]. Thus, continuous monitoring of these assets is more suitable. Thien et al [26] investigated coupled impedance-based and Lamb waves propagation methods for overall pipeline health monitoring. The authors adopted electromechanical coupling effects of

[3] Hydrostatic test involves pressurizing the pressure boundary equipment to a point greater than the maximum operating pressure. The pressure is then observed for several hours to determine if any leaks are present. Because a hydrostatic test could potentially cause a leak or rupture, all the hazardous materials in the pipeline must be replaced with water to prevent environmental damage

piezoelectric-based active sensor i.e. macro fibre composite (MFC) to identify cracks and corrosion along the surface and through thickness. Self-sensing impedance was used to evaluate defects at the welded joints. Dezfouli and Zabihollah [27] developed a framework for SHM of buried polyethylene pipelines under static dislocation and vibration by means of the smart structure concept. The concept uses information from different stages of pipeline lifecycle. The Polyvinylidene fluoride (PVDF) (i.e. pressure sensor) was used to evaluate the relationship between the applied loads and the generated voltage. Out et al [28] made a comparative study of a few inspection methods for flexible pipe monitoring. The authors acknowledged that AE is a useful technique for online monitoring based on their evaluation from full-scale test riser. However the authors highlighted that the technique needs significant development since AE were directly responding to variable loads and suffered from signal attenuation. Jacques et al [29] experimented full dynamic loading test on 6 meters long section of flexible riser with end connectors. The authors used a combination of NDT techniques to identify rupture of wires. Fibre Bragg grating was used to validate AE signals during full-scale dynamic loading tests. Fibre Bragg grating is deployed in an optical fibre where a small amount of light signals is reflected under Bragg condition. The wavelength of these signals is called Bragg wavelength that will change according to physical conditions such as strain or temperature. The author highlighted the advantage of using AE with optimum sensor distribution at areas prone to damage occurrence. Clarke et al [30] employed different combinations of measurement techniques on the same wires used by Jacques et al [29] to observe the relationship between torsional angle variation and axial displacement with AE. Although AE provided strong indication of damage the received AE signals were affected by the induced load variation. The authors discarded the usage of AE as a sole monitoring technique.

2.5 ACOUSTIC EMISSION TESTING

Acoustic emission (AE) is a passive[4] NDT technique. It is related to energy dissipation due to rapid change of stress state within a material such crack initiation or crack extension resulting from fatigue. The energy is released in the form of transient elastic waves [31]. The elastic waves travel randomly within a structure in microscopic displacement and are detected by AE sensors. These sensors are transducers that convert mechanical waves into electrical signals. Therefore, AE monitoring is the only NDT technique that is able to detect damage at the same time it occurs. The benefit of using AE is that it is able to detect structural damage in the early stage, which provides a great advantage for structural integrity assessment. The AE technique was developed by Kaiser [32] over sixty years ago during a tensile test, using [33] piezoelectric crystal microphone from quartz and Rochelle salt crystals to record waves generated from cracks. His great effort contributed to the profound discovery i.e. Kaiser effect[5]. Drouillard [34] provides an exhaustive review of many early experimental works and history of AE prior to 1996. The information includes information about AE such as past research works, technology and collaboration of acoustic emission working groups.

2.5.1 Acoustic Emission Source

In metallic structures, AE sources consist of continuous and burst signals [35]. Continuous emission signals are usually generated during plastic deformation in metals and alloys. The signals associated with this mechanism usually exhibit random distribution and are regarded as noise, while burst AE signals are generated from a distinct failure process such as cracks occurrence. The burst signal can be characterized by Green's function [36]. The examination of AE signals in time domain is important in

[4] **"**Passive" refers to the signals generated within the material whereas "active" receives the reflection of the emitted signals by the NDT instrument itself

[5] Kaiser effect i.e. no signals will be generated upon the second loading until the previous maximum load is exceeded

understanding the nature of AE sources, eliminating false interpretations. The relationship between AE sources and the acquired signals has been studied extensively in the past and can be summarized in a two-step process; first, the creation of damage, which can be related to the stress-strain relationship (i.e. AE source generation) and second, the dynamic behaviour of the waves resulting from damage (i.e. wave propagation).

2.5.2 Acoustic Emission Source Localization

In practice, there are many standards for AE inspection techniques such as American Society for Testing and Materials (ASTM) [37,38]. The general guidelines for acoustic emission test, such as determination of time of arrival (TOA) for source localization in most commercial AE software are described in [39]. Acoustic emission localization is an inverse technique locating AE sources using TOA. The AE events are classified according to TOA and the source location is calculated using linear or planar localization algorithms. The general assumptions of these algorithms are as follow:

1) The material is isotropic.
2) The wave velocity is homogenous (otherwise location error can occur)
3) The wave propagation is undisturbed (the wave has a direct path without obstacles)

2.5.2.1 Linear Localization

The Linear localization method is used in linear structures such as pipe or slender bar as illustrated in Figure 2-6. The source locations are estimated using pre-defined wave velocity and relative time difference between two sensors. The limitation of this technique is that it is only suitable for one-dimensional cases such as a long/small diameter pipe or narrow plate/beam where AE sensors are placed linearly along direct path of wave propagation. However, this technique fails to estimate source localization on a large structure where the third dimension is important. The equation for linear localization is described as follows;

$$d = \frac{1}{2}\left(D - \Delta t_{1,2} V\right) \tag{2-2}$$

D −Distance between sensor 1 and 2

d −Distance between sensor 1 and AE source

V −Wave speed

$\Delta t_{1,2}$ −Time difference between sensor 1 and 2

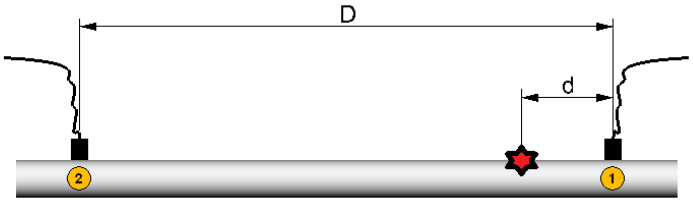

Figure 2-6 Linear localization method

2.5.2.2 Planar Localization

The time of arrival (TOA) between two signals is used to locate AE sources using the intersection of hyperbolae. At least 3 sensors are required to explicitly determine the acoustic emission source for each sensor pair (i.e. 1-2, 2-3, 1-3). The formula for planar localization can be mathematically described using the following equations;

$$\begin{aligned}
&\Delta t_{1,2} V = R_1 - R_2 \\
&Z = R_2 \sin\theta \\
&R_1^2 = Z^2 + (D - R_2 \cos\theta)^2 \\
&R_1^2 = R_2^2 \sin^2\theta + D^2 - 2DR_2 \cos\theta + R_2^2 \cos^2\theta \\
&\left(\Delta t_{1,2} V + R_2\right)^2 = D^2 - 2DR_2 \cos\theta + R_2^2 \\
&\Delta t_{1,2}^2 V^2 + 2R_2 \Delta t_{1,2} V = D^2 - 2DR_2 \cos\theta \\
&2R_2\left(\Delta t_{1,2} V + D\cos\theta\right) = D^2 - \Delta t_{1,2}^2 V^2 \\
&R_2 = \frac{1}{2}\left(\frac{D^2 - \Delta t_{1,2}^2 V^2}{\Delta t_{1,2} V + D\cos\theta}\right)
\end{aligned} \tag{2-3}$$

D −Distance between sensor 1 and 2

R_1 −Distance between sensor 1 and AE source

R_2 −Distance between sensor 2 and AE source

$\Delta t_{1,2}$ −Time difference between sensor 1 and 2

θ − Angle between lines R_2 and D

Z −Line perpendicular to D

V −Wave speed

The intersection of hyperbolae represents the source point as illustrated in Figure 2-7.

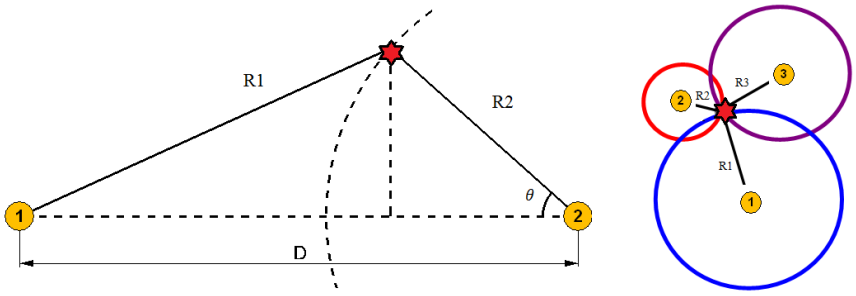

Figure 2-7 Planar localization method

Equation (2-3) is solved by numerical approaches using time difference and distance between sensors. Only a constant wave velocity can be set in any commercial AE acquisition system. Lamb waves are dispersive in nature hence causing error for locating the source if proper calibration is not carried out. The linear and planar localization methods are commercially available and embedded in many AE acquisition systems.

2.5.2.3 Other Source Localization Methods

Single Sensor Modal Analysis Location (SSMAL) technique [40] is an alternative to TOA, but is limited to simple geometries. SSMAL exploits Lamb waves by manipulating the time delay of symmetric wave mode S_0 and asymmetric wave mode A_0. The identification of S_0 and A_0 is known as Modal Acoustic Emission (MAE). The inherent problem associate with this method is the discrimination of signals into distinct modes. The wave decomposition into symmetric wave mode (extensional) and asymmetric wave

mode (flexural) is detailed in [41,42]. Holford et al [40], examined Lamb waves propagation using SSMAL to predict the locations of H-N sources using a single sensor. Baxter et al [43] established a novel technique "Delta T" which utilizes an artificial source that records the time difference information at a number of locations i.e. grids. This method does not require sensor locations or wave speed to be known prior to the test and hence can be used effectively over a large structure. Although various localization techniques are available the evaluation of uncertainties associated with source localization received less attention in many industrial applications. One of the methods for evaluation of uncertainties in source localization is "Lucy" [44] which is commercially available from Vallen Systeme [44]. "Lucy" is a standard deviation of the measured distances to the calculated distances of the sources which is described as follows;

$$Lucy = \left\{\left(\frac{1}{[n-1]}\right) \times \left[\sum_{i=2}^{n} (D_i - P_i)^2\right]\right\}^{1/2}$$

$$D_i = dti \times v$$

$$P_i = R_i - R_1 \qquad (2\text{-}4)$$

where;

dti is the arrival time difference

v is the group velocity

P_i is radial distance from the trigger sensor

R_i is the distance from the calculated source to each sensor

n is the number of sensors hit for each source event

"Lucy" is only valid if the system of equations is overdetermined (many sensors). The method relies on the arrival wave modes which is threshold dependent. For planar localization, at least four sensors are required for "Lucy" to be valid, although only three sensors are required for planar localization.

2.5.3 Acoustic Emission Application in Fatigue Analysis

AE signals are usually studied according to a particular damage mechanism such as micro/macro fractures, crack initiation, plastic deformation and crack growth in metals or delamination and fibre breakage in composite materials. There are also mixtures of signals due to noise from the environment. Therefore, discrimination of signals is crucial. Damage associate with fatigue in a structure usually occur before yielding, caused by cyclic loadings. During this process, a structure undergoes plastic deformation, crack initiation and extension [45]. In theory crack extension leads to sudden drop in stress from a maximum value at crack tip, the stress diminishing when the crack propagates. The stress unloading time depends on material strength. The unloading time decreases in brittle structure [46]. Heiple and Carpenter [47] provided extensive review of AE sources production during deformation of metals in the late 80's. The review covers many aspects of deformations such as dislocation motion, deformation twinning, and inclusion. Lindley et al [48] studied AE signals near the peak load of fatigue cycle and separated the AE signals from those occurring near the minimum load by using a gating[6] technique. The peak and minimum loads were attributed to crack extension and crack closure respectively. The authors concluded that for low strength material, the peak load emission is mostly related to deformation and fracture within the crack tip plastic zone rather than during crack extension, whereas for high strength material, the peak load emission is observed in both events. Similar gating techniques for high cycle fatigue problem have been studied earlier by Smith and Morton [49]. They have remarkably eliminated extraneous noises and discriminated acoustic emission signals from crack extension and closure with correlation methods of the arrival signals. The conventional features used in AE techniques can provide some information about the potential damage. Ai et la [50] used AE signals to monitor leaks caused by fatigue crack induced by hydraulic pressure to simulate active defect evolvement. The energy and amplitude of the AE signals help to forecast potential failure.

[6] A voltage controlled gate to count emissions only at the requisite part of the cycle

2.5.4 Damage Characterization

Damage characterization is essential in Non-Destructive Testing (NDT). The conventional NDT techniques such as ultrasonic testing, dye penetrant, electric inspection, radiography and AE [51] are normally used for structural condition assessment as well as damage characterization. These methods are very effective but require detection and localization of damage in prior. Damage characterization using AE is useful by means of observable parameters of AE signals such as AE counts (i.e. number of times a signal crosses the pre-set threshold amplitude). Early work by Dunegan [52] studied the relationship of AE count rate with stress intensity factor (ΔK) which leads to the equation;

$$N' = A\Delta K^{n} \tag{2-5}$$

where N' is AE count rate, A and n are constants which depends on the type of materials. The above equation was derived from linear elastic fracture mechanics (LEFM) [53] with assumptions;

1) AE occurs primarily at the crack tip in plastic region between the yield and ultimate tensile stress
2) AE count rate is proportional to the variation of volume of material
3) The strain at crack tip varies with $r^{-\frac{1}{2}}$, where r is the radial distance from the crack tip

The AE signal characteristics provide useful information about structural condition. In composite structures, AE generated in laminated plates under tension provides indication of a specific failure type. Prosser [54] studied AE generated in composite coupons where he demonstrated that large amplitudes of extensional wave mode correspond to matrix cracking while large amplitudes of flexural wave mode are associated with grip damage. The author highlighted that modal AE can provide information about damage signatures. Damage characterization can be deduced from AE signals rise time (RT) as illustrated in the Figure 2-8. The image shows an example of AE signal generated during tensile event.

The rise time is the time between arrival time and the maximum peak. AE signals with shorter rise time indicate domination of symmetric waves. Longer rise time indicate domination of asymmetric waves. The study shows that without knowing sensor coordinates and distance from the source, symmetric waves may be mistaken for asymmetric waves.

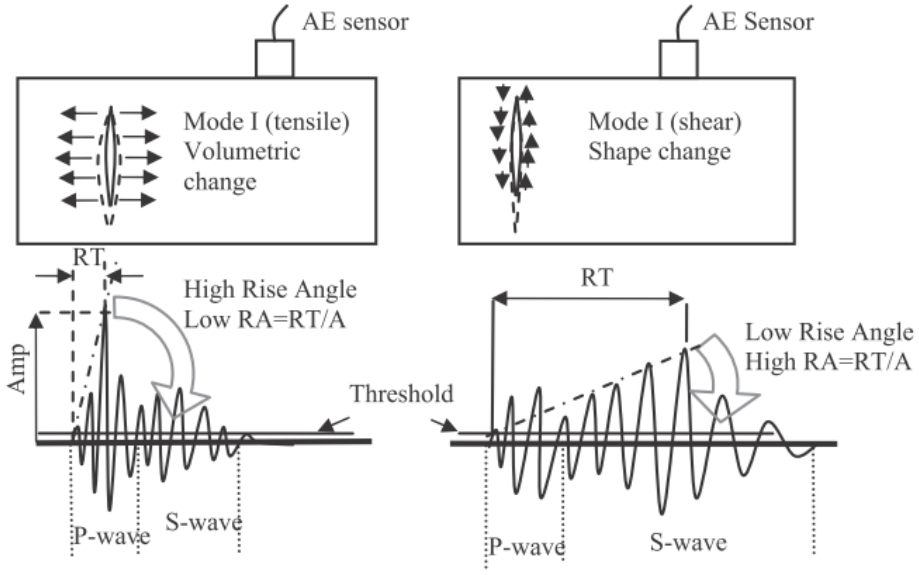

Figure 2-8 Signal rise time (RT). Cracking modes (top) and its corresponding signals (bottom), typically consist of symmetric and anti-symmetric modes of AE signals [55]

Crack growth rate is another useful parameter in fracture mechanics to measure crack propagation rate. Paris et al [56] established a notable relationship of crack propagation rate and crack intensity factor as follows;

$$a' = C\Delta K^{m} \tag{2-6}$$

where a' is crack propagation rate, C and m are constants which depends on material type. Equation (2-5) and (2-6) provide a relationship of AE count rates and crack propagation rates. Bassim et al [57] established the condition for both equations, such that $n = m$ or $n = m + 2$ depending on the load ratio, R i.e. $\left(R = \frac{F_{min}}{F_{max}}\right)$. The former is

used for high load ratio such as large mean stress. Roberts and Talebzadeh [58,59] also conducted experiments on steel specimens with various load ratios and correlate crack propagation rates and AE count rates. The authors concluded that AE monitoring is able to predict remaining life of fatigue damaged structures. Since AE count rate is time dependent as the load near the peak load and hence, further integration of this parameter with time would determine the life of a structure.

2.5.5 Fatigue Damage Prognosis

Fatigue damage prognosis[7] by means of probabilistic approach can be useful for fatigue life prediction and damage characterization. Farrar [60] summarized the elements of the damage prognosis process as illustrated in Figure 2-9.

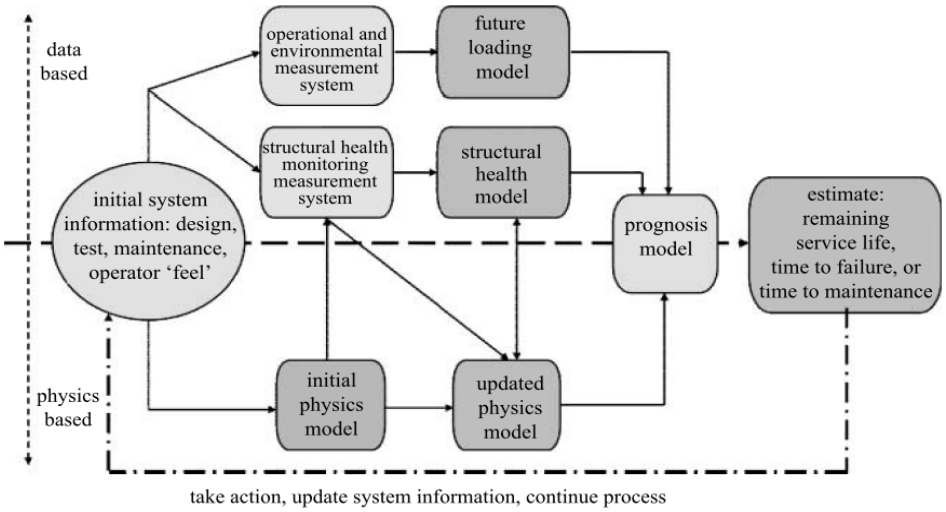

Figure 2-9 General component of a damage prognosis [60]

The theoretical relationship between AE features and fracture mechanics makes the probabilistic approach attractive [61]. The underlying concept of damage prognosis is

[7] Damage prognosis uses combination of information from the system's original, past, current, and anticipated future environmental and operational conditions to estimate the remaining useful life of the system

based on detection and characterization of damage determined using measurement data coupled with failure mechanics such as damage growth model. The physical parameters that associate with crack growth are subjected to various uncertainties. The probabilistic approach to estimate crack growth with various uncertainties in crack model, measurement data and physical variability is found effective. Carpinteri et al [62] used fragmentation fractal analysis to predict damage evolution and time to failure. Their proposed technique was to evaluate the energy dissipation detected by AE in fractal domain. Ling and Mahadevan [63] integrated fatigue damage with SHM data, taking into account various sources of uncertainty and errors by means of probabilistic framework i.e. Bayesian network. Zárate et al [64] used Bayesian inference to account for various uncertainties. The authors incorporated model updating to build probability distribution of the unknown parameters. These parameters distributions were used to estimate the stress intensity factor range from the experimental data using multivariable distributions.

2.6 CONCLUDING REMARKS

In this chapter, an overview of damage identification methods and their practical application was carried out. It is learnt that the application of Structural Health Monitoring (SHM) for diagnostic and prognostic to assess fatigue crack problem in process piping requires further research. Guidelines have been published by the Energy Institute which focuses on “through life” management and provides assistance for operators to develop their own management system. Prognosis using likelihood of failure (LOF) scoring method is provided in the guidelines. However, LOF is not the absolute probability of failure. It only provides initial evaluation for follow up inspection and detail assessment. One of the recommended approaches is to use specialist measurement techniques to quantify the damage. However, the guidelines do not explicitly define the requirement and methodology of any relevant technique. Based on this gap, the current research expands the niche in continuous monitoring using vibration and acoustic emission for damage identification. The main element which is considered crucial in damage identification is the predictive technique where type 1 error or *False Negative*

can be eliminated. Damage identification process in this thesis follows the strategies adopted by Rytter [17,65] which includes;

- Level 1 - Damage detection and signals discrimination
- Level 2 - Damage localization
- Level 3 - Damage extent assessment

The above strategies are generally used in conjunction with structural health monitoring (SHM) for diagnostic and prognostic. It is learnt that acoustic emission (AE) is commonly generated in response to structural degradation. AE is considered useful for the current research since it is highly sensitive to structural degradation. However the technique may not be feasible in extreme environment due to susceptibility to noises. Many sources of signals could contribute to false detection. Therefore, the current research must evaluate the usefulness of AE techniques to monitor vibration-induced fatigue problem in extreme environment. AE is highly sensitive to damage evolution, but using AE to detect inclusion or crack initiation in the early stage of damage is difficult. To achieve this, a dedicated experimental setup is proposed using the vibration analysis to discriminate the signals from these events. There are numerous standards and guidelines suggest best practices in conducting AE testing. However, AE application for continuous monitoring must be developed in a robust manner due to uncertainties in AE signals. Bayesian theorem is useful in parameter estimation and measures their uncertainties, and hence is considered promising for the current research. Bayesian estimation has already been used for detection, however it is learnt that a non-informative *prior* was used. The use of *prior* distribution from similar damage state can further improve estimation. Therefore, further research will be conducted in this area. Many types of waves exist in mechanical structures which could originate from damage or operational noise. The elastic waves generated from local defects may be converted into different forms of signals. In this approach the signal classification is important for damage identification. In the current research the waves under study are:

- Rayleigh wave, which travels in elliptical motion across geometric surface. Rayleigh wave velocity is approximately 90% of the shear wave velocity and the

wavelength is approximately equal or smaller than the structural thickness which is generally observed in thick structures such as thick pipes

- Lamb waves, which is important in plate-like structures or thin pipes where the thickness is less than the wavelength.

These important characteristics of waves can be observed in many types of pipework of different thickness. One of the problems associated with incorrect wave mode identification is source localization error due to incorrect time of arrival (TOA). It is learnt from the literature that many source localization techniques are available. However less attention is given to the evaluation of uncertainties associated source localization. It is expected that a large number of calculated events will be recorded during continuous monitoring hence errors in source localization is imminent. Bayesian estimation is believed useful to overcome this problem. The theorem could provide high likelihood of predicted damage locations given prior knowledge about a particular damage mechanism. Hence, a new method shall be developed rather than solely relying on the standard acoustic emission features.

CHAPTER 3

EXPERIMENTAL STUDY OF RAYLEIGH AND LAMB WAVES IN THICK AND THIN STRUCTURES

3.1 BACKGROUND

In the previous chapter, theoretical aspects of acoustic emission (AE) and their practical application have been discussed. However, implementation of the technique for structural health monitoring (SHM) can be difficult since AE signals are susceptible to noise; large amount of unusable data may be recorded. Therefore it is important to understand different aspects of waves observed in AE testing. In this chapter, waves generated by artificial crack using standard lead breakage (ASTM - E569-97) often known as Hsu-Nielsen (H-N)[8] and Gaussian pulses generated by AE sensors were studied. The specimens comprised of a defect free aluminium plate and carbon steel pipe. The idea in this chapter, apart from understanding the typical waves observed in AE wave analysis, is to observe near-field and far-field effects. Similar studies have been carried out extensively by Hamstad et al [66–69] although the works were only done on thick plates. It has been noted that Rayleigh wave is particularly important in thick structures. Therefore, in this chapter, it is of interest to understand Rayleigh waves and Lamb waves observed in different structures. The outcome from this study provides fundamental understanding of AE technique and early investigation prior to their implementation for continuous monitoring.

[8] Hsu-Nielsen (H-N) is referred to the pencil lead breakage for artificial acoustic emission source

3.2 ELASTIC WAVES

Waves theory was developed in the 18th century upon discovery of dynamical equations of waves in solids by Cauchy [70]. The theory was limited to linear approximation of stress and strain such that the deformation is small and the stress states do not produce yielding. The theory evolved from longitudinal and transverse waves into many type of waves such as Rayleigh, Lamb and Love waves. The formulation of elastic waves propagation was derived from the theory of elasticity. Elastic wave propagation is also known as elasto-dynamics. The equations of motion of elastic waves are based on Newton's second law. Using an infinitesimal cubic element with respect to the reference state[9], the mathematical formulation can be written as follows;

$$\rho_0 a_i = \rho_0 \frac{\partial^2 u_i}{\partial t^2} = \frac{\partial \sigma_{ij}}{\partial x_j} \tag{3-1}$$

Where ρ_0 is the material density at the reference state, a_i is the acceleration, u_i is the displacement, t is time, x_j is the principal coordinate system (as shown in Figure 3-1) and σ_{ij} is the stress tensor.

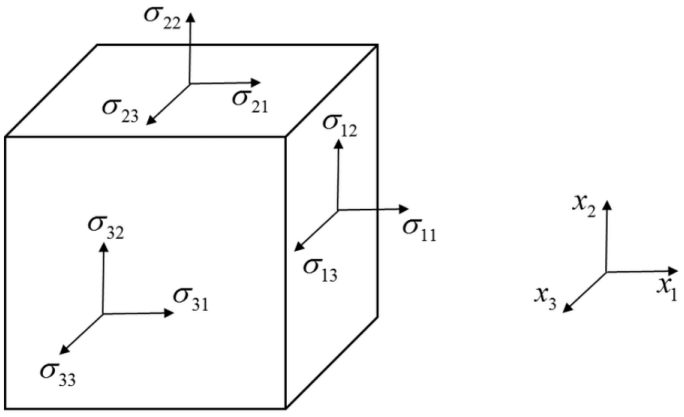

Figure 3-1 Principal axes of stress components

[9] The reference state here means spatial coordinates or volume of infinitesimal cube of elastic solid before deformation

The relationship can be written in three dimensional axes as follows;

$$\rho_0 \frac{\partial^2 u_1}{\partial t^2} = \frac{\partial \sigma_{11}}{\partial x_1} + \frac{\partial \sigma_{12}}{\partial x_2} + \frac{\partial \sigma_{13}}{\partial x_3}$$

$$\rho_0 \frac{\partial^2 u_2}{\partial t^2} = \frac{\partial \sigma_{21}}{\partial x_1} + \frac{\partial \sigma_{22}}{\partial x_2} + \frac{\partial \sigma_{23}}{\partial x_3}$$

$$\rho_0 \frac{\partial^2 u_3}{\partial t^2} = \frac{\partial \sigma_{31}}{\partial x_1} + \frac{\partial \sigma_{32}}{\partial x_2} + \frac{\partial \sigma_{33}}{\partial x_3} \tag{3-2}$$

The stress at any point in time will depend on the strain at that time which is given as follows;

$$\sigma_{ij} = c_{ijkl}\varepsilon_{ij} \tag{3-3}$$

Here ε_{ij} is linear strain tensor derived from *Langrangian strain tensor* that corresponds to material deformation relative to the reference state and c_{ijkl} is the stiffness or elastic tensor. The linear strain tensor can also be represented in terms of displacement;

$$\varepsilon_{ij} = \frac{1}{2}\left(\frac{\partial u_i}{\partial x_j} + \frac{\partial u_j}{\partial x_i}\right) \tag{3-4}$$

The above equation consists of nine components of strain as follows;

$$\begin{bmatrix} \varepsilon_{11} & \varepsilon_{12} & \varepsilon_{13} \\ \varepsilon_{21} & \varepsilon_{22} & \varepsilon_{23} \\ \varepsilon_{31} & \varepsilon_{32} & \varepsilon_{22} \end{bmatrix} = \begin{bmatrix} \frac{\partial u_1}{\partial x_1} & \frac{1}{2}\left(\frac{\partial u_1}{\partial x_2} + \frac{\partial u_2}{\partial x_1}\right) & \frac{1}{2}\left(\frac{\partial u_1}{\partial x_3} + \frac{\partial u_3}{\partial x_1}\right) \\ \frac{1}{2}\left(\frac{\partial u_2}{\partial x_1} + \frac{\partial u_1}{\partial x_2}\right) & \frac{\partial u_2}{\partial x_2} & \frac{1}{2}\left(\frac{\partial u_2}{\partial x_3} + \frac{\partial u_3}{\partial x_2}\right) \\ \frac{1}{2}\left(\frac{\partial u_3}{\partial x_1} + \frac{\partial u_1}{\partial x_3}\right) & \frac{1}{2}\left(\frac{\partial u_3}{\partial x_2} + \frac{\partial u_2}{\partial x_3}\right) & \frac{\partial u_3}{\partial x_3} \end{bmatrix} \tag{3-5}$$

For homogenous and isotropic materials, the relation given by equation (3-3) can be simplified using Lamé parameters with two independent components of elastic tensor such that [71];

$$c_{ijkl} = \lambda\delta_{ij}\delta_{kl} + \mu(\delta_{ik}\delta_{jl} + \delta_{il}\delta_{jk}) \tag{3-6}$$

and for strain tensor;

$$\varepsilon_{ij} = \lambda\delta_{ij}\varepsilon_{kk} + 2\mu\varepsilon_{ij} \tag{3-7}$$

Where λ and μ are the Lamé constants and ε_{kk} is the trace of the strain tensor i.e. volumetric change of the element. δ_{ij}, δ_{kl} etc. is kronecker delta such that $\delta_{ij} = 0$ if $i \neq j$ or $\delta_{ij} = 1$ if $i = j$. Equation (3-7) can be written $\lambda\delta_{ij}\varepsilon_{kk} = \lambda(\varepsilon_{11} + \varepsilon_{22} + \varepsilon_{33}) = \lambda\Delta$ when $i = j$. The relationship of the stress and strain then becomes;

$$\begin{aligned} &\sigma_{11} = \lambda\Delta + 2\mu\varepsilon_{11} \quad \sigma_{22} = \lambda\Delta + 2\mu\varepsilon_{22} \quad \sigma_{33} = \lambda\Delta + 2\mu\varepsilon_{33} \\ &\sigma_{12} = \mu\varepsilon_{12} \qquad \sigma_{23} = \mu\varepsilon_{23} \qquad \sigma_{13} = \mu\varepsilon_{13} \end{aligned} \tag{3-8}$$

By substituting the relation of the stiffness tensor and (3-8) into (3-1) gives;

$$\rho_0 \frac{\partial^2 \boldsymbol{u}}{\partial t^2} = (\lambda + \mu)\nabla(\nabla.\boldsymbol{u}) + \mu\nabla^2\boldsymbol{u} \tag{3-9}$$

where,

$$\begin{aligned} &\nabla = \partial/\partial x_1 + \partial/\partial x_2 + \partial/\partial x_3 \,, \\ &\nabla^2 = \partial^2/\partial x_1^2 + \partial^2/\partial x_2^2 + \partial^2/\partial x_3^2 \end{aligned} \tag{3-10}$$

Equation (3-9) is the equation of motion for isotropic elastic medium [71]. The second term in RHS of (3-9) is the *Laplacian* term of $\boldsymbol{u}$ which can also be represented as follows;

$$\nabla^2\boldsymbol{u} = \nabla(\nabla.\boldsymbol{u}) - \nabla \times (\nabla \times \boldsymbol{u}) \tag{3-11}$$

Therefore;

$$\rho_0 \frac{\partial^2 \boldsymbol{u}}{\partial t^2} = (\lambda + 2\mu)\nabla(\nabla.\boldsymbol{u}) - \mu(\nabla \times (\nabla \times \boldsymbol{u})) \tag{3-12}$$

These equations are called equation of motion in scalar and vector notations. The displacement field $\boldsymbol{u}$ can be expressed in terms of the sum of the gradient of scalar potential ϕ and the curl of vector potential $\vec{\psi}$ by Hemholtz decomposition, such that;

$$\boldsymbol{u} = \nabla\phi + \nabla \times \vec{\psi} \tag{3-13}$$

By substituting equation (3-13) into (3-12), the equation can be grouped as follows;

$$\nabla\left[\rho_0 \frac{\partial^2\phi}{\partial t^2} - (\lambda + 2\mu)\nabla^2\phi\right] + \nabla \times \left[\rho_0 \frac{\partial^2\vec{\psi}}{\partial t^2} - \mu\nabla^2\vec{\psi}\right] = 0 \tag{3-14}$$

Treating div and curl operators in equation (3-14) independently leads to the following equations;

$$\frac{\partial^2\phi}{\partial t^2} = V_L^2\nabla^2\phi \tag{3-15}$$

$$V_L = \sqrt{\left(\frac{\lambda + 2\mu}{\rho_0}\right)} \tag{3-16}$$

$$\frac{\partial^2\vec{\psi}}{\partial t^2} = V_T^2\ \nabla^2\vec{\psi} \tag{3-17}$$

$$V_T = \sqrt{\frac{\mu}{\rho_0}} \tag{3-18}$$

Therefore, for isotropic and homogenous media, V_L and V_T are the longitudinal (P-wave) and transverse wave (S-wave) velocities respectively. The displacements of P-Wave and S-Wave are illustrated in Figure 3-2.

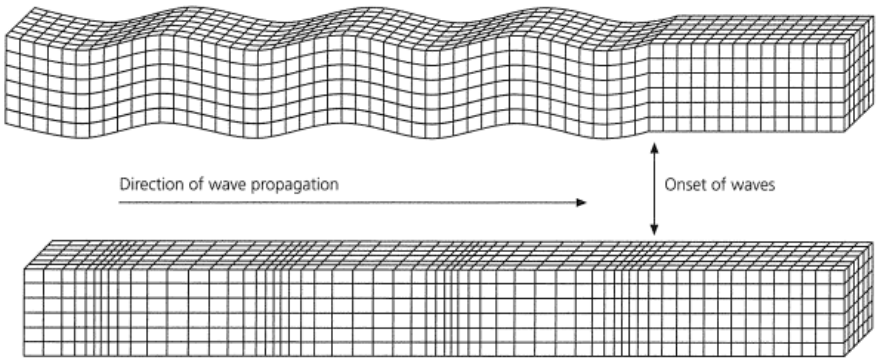

Figure 3-2 Displacements of P-waves (top) and S-waves (bottom); image taken from [71] page 57.

Both the *Lamé* constants in equation (3-16) and (3-18) can be replaced by the Young's modulus and Poisson ratio; thus, the equations can be written in the form;

$$V_L = \sqrt{\frac{E(1-\nu)}{\rho_0(1+\nu)(1-2\nu)}} \tag{3-19}$$

$$V_T = \sqrt{\frac{E}{2\rho_0(1+\nu)}} \tag{3-20}$$

In semi-infinite space, the surface wave is known as "Rayleigh wave" discovered by Lord Rayleigh [72]. The wave exhibit elliptic motion as illustrated in Figure 3-3.

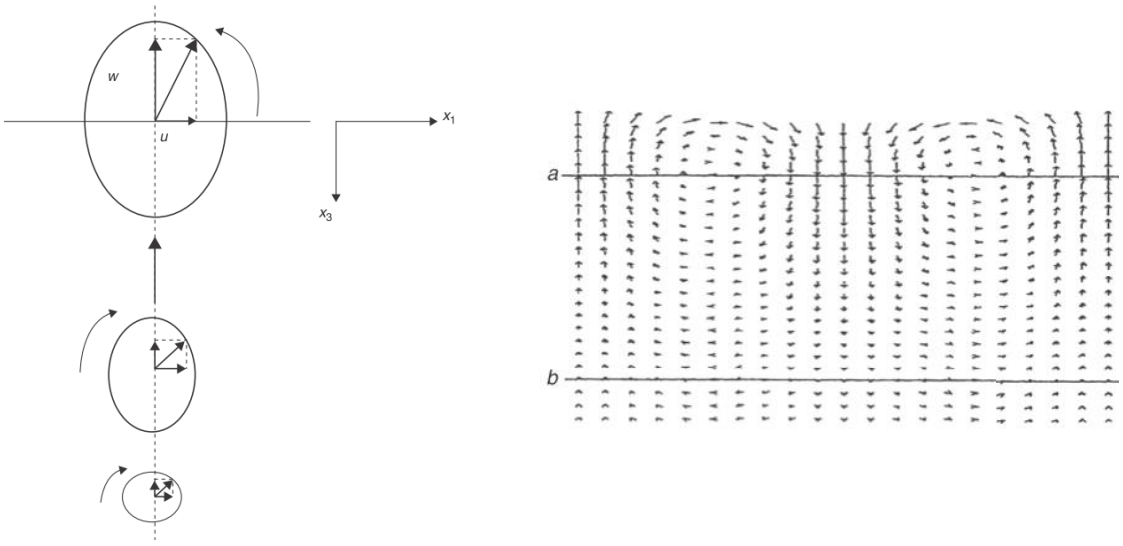

Figure 3-3 Displacement vector elliptical particle motion with depth; image taken from [73] page 112. Line *a* denotes the reversal of particle rotation. Line *b* represents the one wavelength of the Rayleigh wave.

Waves in a finite body such as thin plates, where the wavelength is larger than thickness, exhibit so-called Lamb wave[74]. In general there are two fundamental wave modes, symmetry and asymmetry about the plate mid-plane. The characteristic equation can be represented by the following equations;

$$\frac{\tan(\beta d/2)}{\tan(\alpha d/2)} = -\frac{4\alpha\beta k^2}{(k^2-\beta^2)^2} \tag{3-21}$$

$$\frac{\tan(\beta d/2)}{\tan(\alpha d/2)} = -\frac{(k^2-\beta^2)^2}{4\alpha\beta k^2} \tag{3-22}$$

where,

$$\alpha^2 = \frac{\omega^2}{V_L^2} - k^2$$

$$\beta^2 = \frac{\omega^2}{V_T^2} - k^2$$

The velocities are no longer constant (i.e. non-linear relation) as in the infinite medium but dependent on wave frequencies. These waves are dispersive in nature and represented graphically by the phase and group velocities, commonly regarded as dispersion curves. The relationship of phase velocity V_p and group velocity V_g are given as follows;

$$V_p = \frac{\omega(k)}{k} \tag{3-23}$$

$$V_g = \frac{\partial\omega(k)}{\partial k} \tag{3-24}$$

Example of dispersion curves and wave modes are illustrated in Figure 3-4 and Figure 3-5 respectively. At higher frequencies, a number of wave modes exist. The fundamental waves travel at constant velocity which is referred to as Rayleigh waves. These waves are important for the analysis of wave propagation in thick structure.

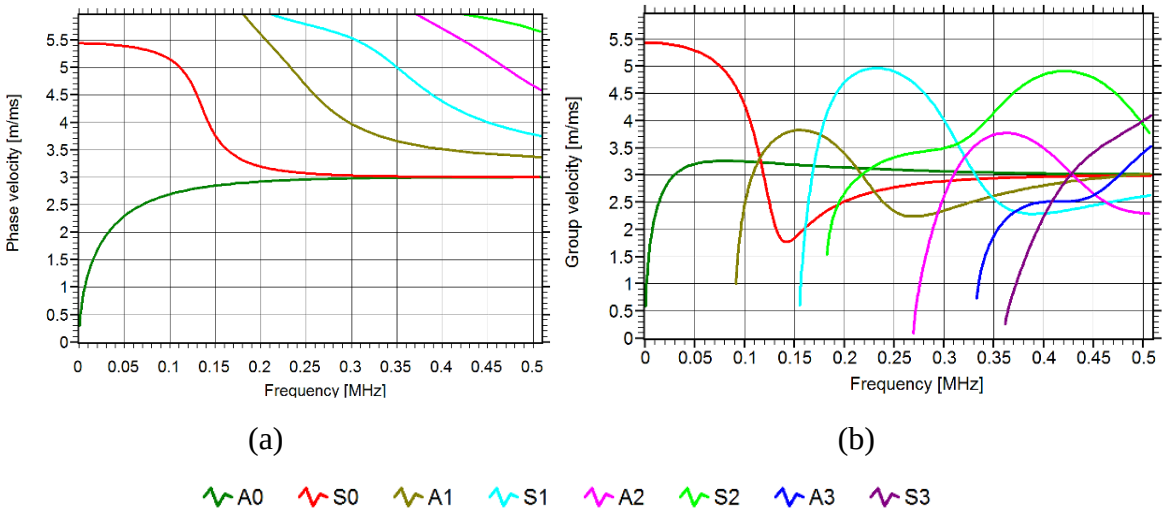

Figure 3-4 (a) Phase velocity (b) group velocity in steel plate [44]

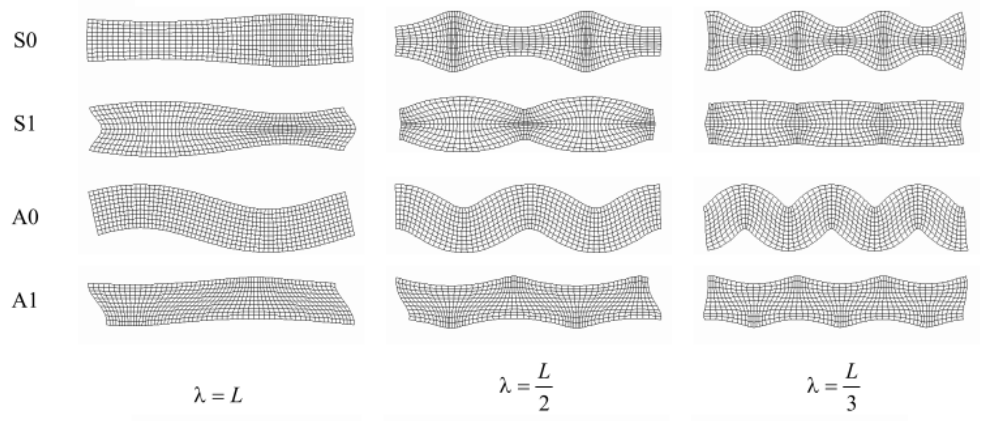

Figure 3-5 Example of Lamb wave modes of different wavelength (λ) that is submultiple of plate length, L [75]

The wave modes illustrated in Figure 3-5 shows physical significance of symmetrical (S) and asymmetrical (A) waves. In general, Lamb waves are guided by structural boundaries having finite thickness. Waves in tubes have a larger number of modes compared to waves in plates, such as waves which propagate in the circumference direction. The common wave modes consist of axisymmetric longitudinal wave/axial L(0,*m*), non-axisymmetric flexural wave/radial F(*n*,*m*) and circumferential wave/torsional T(0,*m*) [76,77]. The *m* and *n* are the axial nodal pattern and circumferential nodal pattern respectively. Example of such wave modes are illustrated in Figure 3-6. Silk and Bainton [78] investigated ultrasonic wave propagation in metal tube. They concluded that The L(0,*m*) corresponds to all Lamb waves in plates including symmetric and asymmetric wave modes.

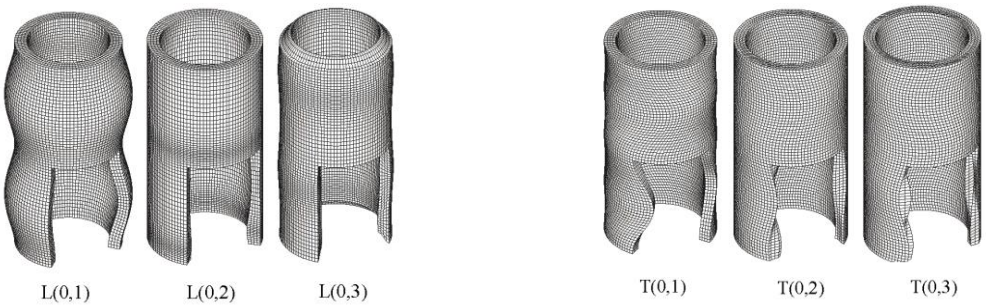

$n = 0$, $m = 1,2,3$	$n = 0$, $m = 1,2,3$
$n = 1$, $m = 1,2,3$	

Figure 3-6 Example of longitudinal, torsional and flexural wave modes [75]. Wave number (m,n) of axial nodal pattern (m) and circumferential nodal pattern (n).

The application of wave propagation in structures is very wide such as guided wave inspection technique (GW) [79–81]. In this technique specific types of waves are generated using actuators/piezoelectric sensors [82]. The reflection of signals provides information about the location of defects. The basis of wave propagation can be understood by the interaction of interconnecting springs and masses. The speed of propagation increases as the stiffness and mass increases, or vice versa.

3.2.1 Dispersion Extraction by DISPERSE Code

The use of Lamb waves for damage detection was first studied by Worlton [83]. One of the main challenges using Lamb waves is to identify wave modes for damage detection; thus, knowledge of dispersion curves is essential. Depending on material properties and geometry complexity, dispersion curves may be obtained by analytical methods from theory of elasticity [70,84] or using the finite element method. The analytical methods have limitation in that for higher order wave modes the solution can be inherently

complex. Numerical approach such as superposition of bulk wave (SPBW), which uses matrix based method developed by Lowe [85] or semi-analytical finite elements (SAFE) are used for generating dispersion curves. SAFE uses geometry cross section element mesh and calculates displacement along the wave direction using exponential functions. This method can be used for many geometry cross sections [86]. Another simple approach is to use standard finite element model with periodic boundaries formulation [87] that is available in many commercial softwares such as ANSYS [75] or Abaqus FEA [88]. In the current work, DISPERSE code, based on analytical methods developed by Pavlakovic [89], was used to generate dispersion curves for plate and pipe geometries. The calculated dispersion curves are shown in Figure 3-7 to Figure 3-10 based on the geometry properties provided in Table 3-1. The width of the plate is not necessary for dispersion curves extraction assuming that the plate is two dimensions. However for wave propagation analysis the effect of the side boundaries are discussed in the subsequent section. It is learnt that L(0,*m*) family modes consist of all Lamb waves in plate including the fundamental symmetric and asymmetric wave modes [78]. Some flexural waves (i.e. non-axial symmetry) have similar wave velocities with the extensional waves [75] as can be seen in Figure 3-7 and Figure 3-8.

Geometry	Pipe	Plate
length (m)	7.2	1
Width (mm)	-	50
Outside diameter (mm)	381	-
Thickness (mm)	50	3
Poisson ratio	0.29	0.33
Density (kg/m³)	7850	2700
Young's modulus (GPa)	210	70

Table 3-1 Pipe and plate physical properties

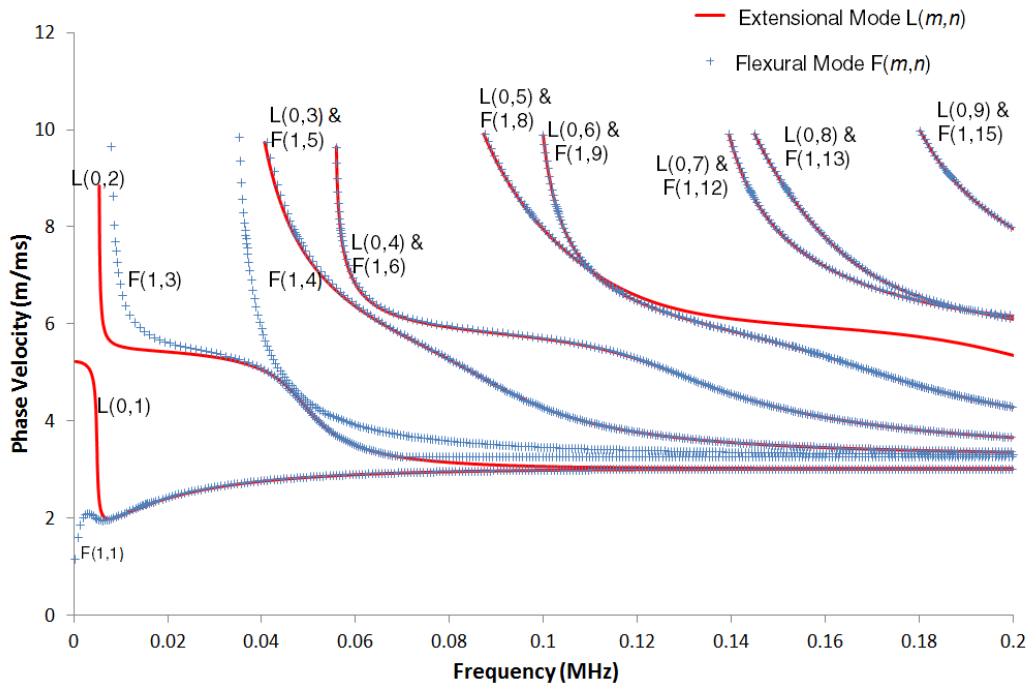

Figure 3-7 Phase velocities against frequencies of various wave modes in pipe; solid line represents extensional wave mode; markers represent flexural wave mode [90].

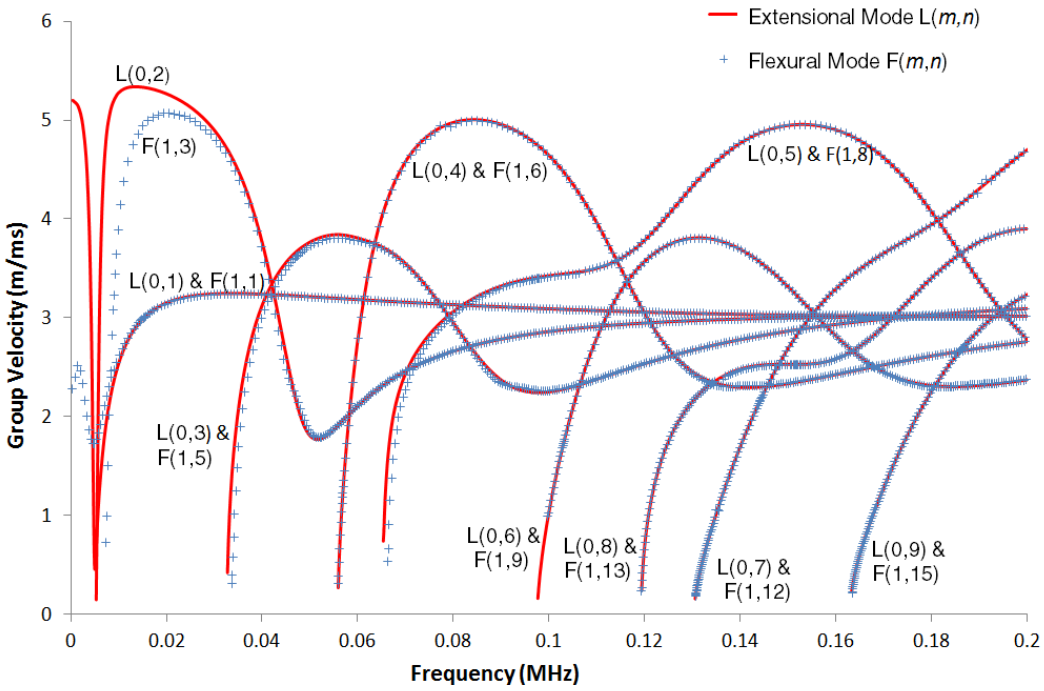

Figure 3-8 Group velocities against frequencies of various wave modes in pipe; solid line represents extensional wave mode; markers represent flexural wave mode [90].

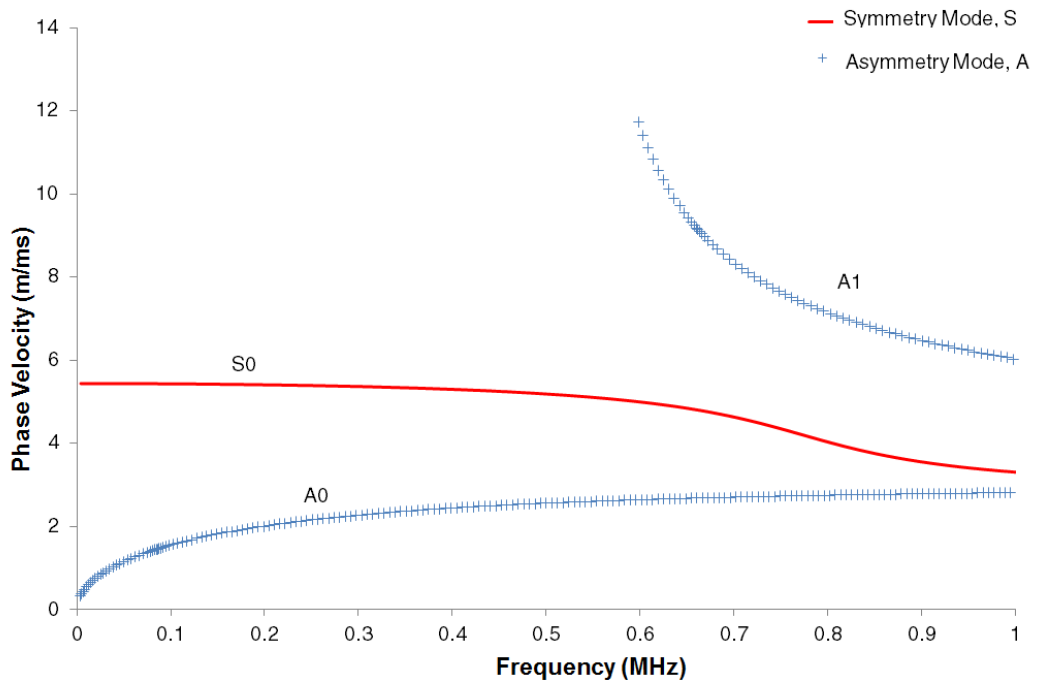

Figure 3-9 Phase velocities against frequencies of various wave modes in plate; solid line represents symmetry wave mode; markers represent asymmetry wave mode [90].

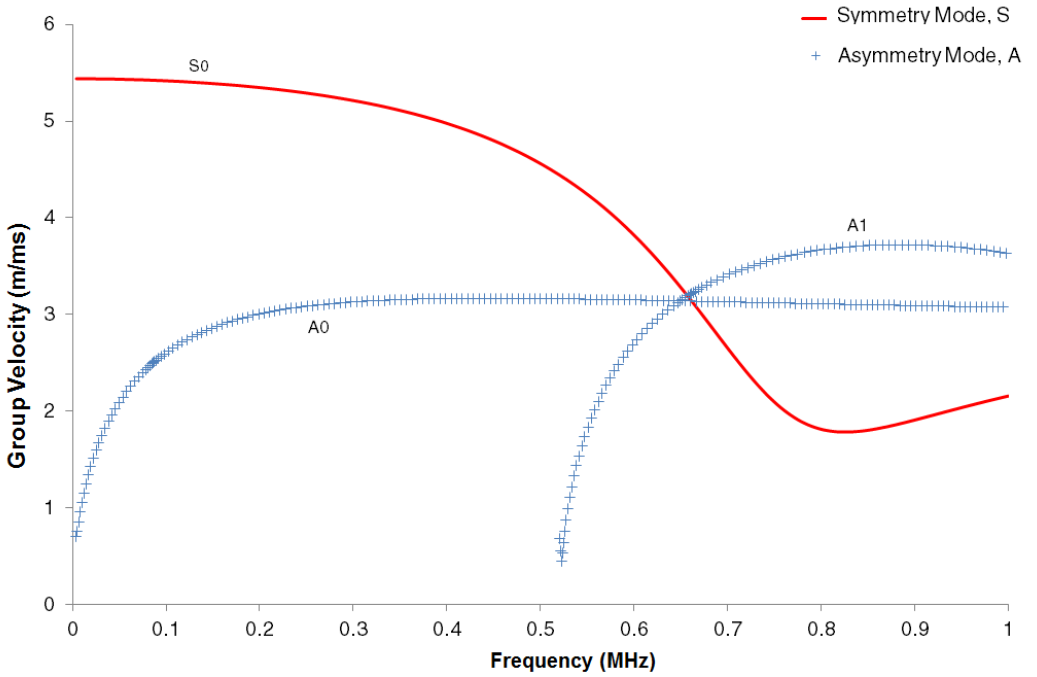

Figure 3-10 Group velocities against frequencies of various wave modes in plate; solid line represents extensional wave mode; markers represent flexural wave mode [90]

3.2.2 Waves Attenuation

Acoustic emission signals generated from crack damage usually present a broad range of frequencies. However only low frequencies waves are able to travel farther and are captured by AE sensors, due to the fact that higher frequency waves experience higher attenuation. Attenuation is commonly understood as an exponential decay of wave amplitudes with distance. Attenuation is caused by many factors such as geometric scattering, spreading, dispersion and dissipation to adjacent media. These effects are dependent on geometry and material properties. Attenuation is significant for less ductile material. Prosser [54] observed that the peak amplitude of flexural waves (i.e. asymmetric waves) suffered large attenuation due to geometric spreading compared to symmetric waves. Pollock [91] demonstrated that the geometric spreading was the major contributing factor for attenuation in the near field close to the sources.

3.3 ANALYSIS PROCEDURES

In the current research, a signal based analysis was carried out to observe wave modes directly from transient signals. The signals were transformed into time and frequency domain using wavelet transformation (WT) to enhance the identification of wave modes. WT provides good resolution in time and frequency domain [92]. In practical application, WT decomposes signals into various frequency components which are then analysed using different scale of resolution. Wavelets adopt a basis function so-called "mother wavelet". WT uses scaled-varying functions of various window sizes as shown in Figure 3-11.

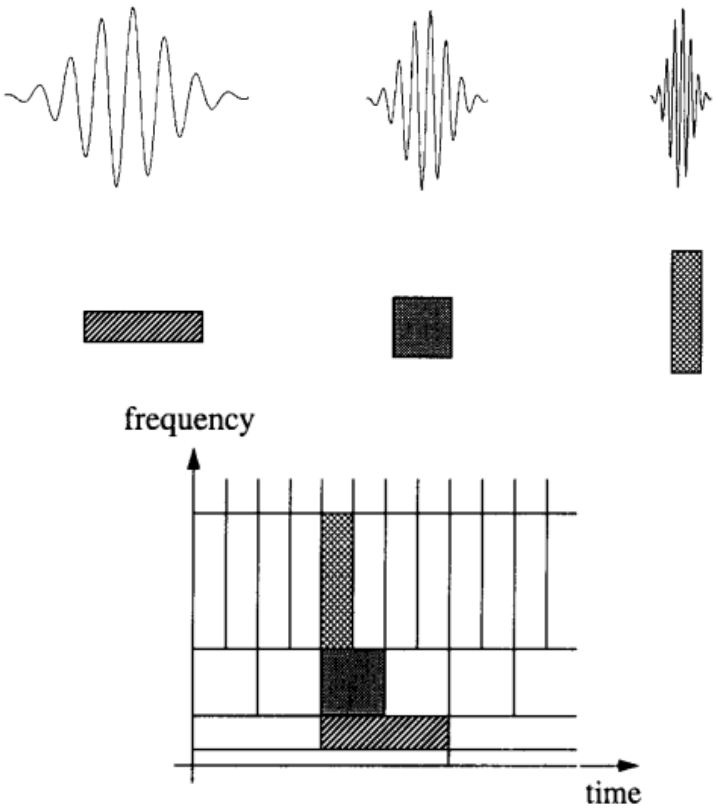

Figure 3-11 The wavelet basis function and time-frequencies tiles (WT)[93].

The function can be scaled to accommodate a range of signal frequencies through division of the signal domain [94]. A short-scaled basis function (a contracted form of wavelet) is useful for high frequency signals and a long-scaled basis function (a dilated form of wavelet) for low frequency signals. WT comprises of discrete and continuous forms. Discrete wavelet transform (DWT) is less computation expensive and provides good signal compression which removes redundancy of the transformed signals. Basically, the signal transformation is based on orthogonality of wavelets such that decomposition of signals is orthogonal to its scaling and translations. DWT have many types of basis function such as Daubechies, Coiflet, Haar and Symlet [92,95,96]. Illustrations of these functions are shown in Figure 3-12. In general, a wavelet basis function can be described as follows:

$$\psi_{a,b}(t) = \frac{1}{\sqrt{2}}\psi\left(\frac{t-b}{a}\right) \tag{3-25}$$

where, $a \in R^+$ define the scale and $b \in R$ define the shift in time. The basis function is dilated or stretched for large *a* (i.e. long-scaled basis function), and contracted for small *a* (i.e. short-scaled basis function). The transformation can be written as follows;

$$X_w(a,b) = \int_{-\infty}^{\infty} \psi^*_{a,b}(t)x(t)dt \tag{3-26}$$

where, *x(t)* is the signals function or data; $\psi^*_{a,b}$ is complex conjugate. DWT performs in a similar manner to the discrete Fourier transform, where the generated matrix is not sparse in general [92]. On contrary, continuous Wavelet Transform (CWT) has larger dimension of signals, where the continuous signal frequencies can be seen on the time-frequency map. However, the data is highly correlated and redundant but smoother than DWT.

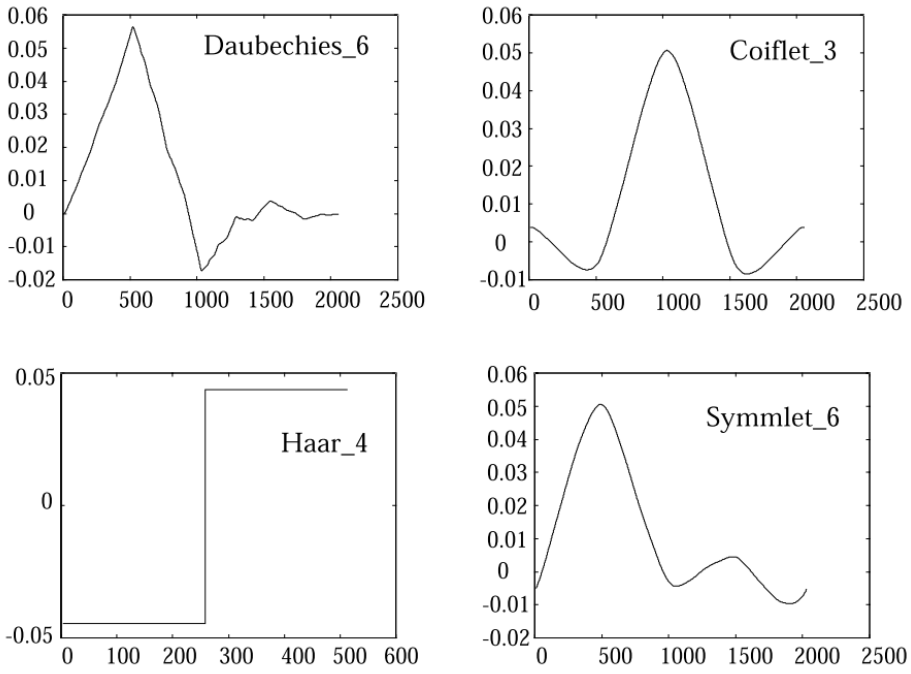

Figure 3-12 Various families of wavelets [92]. The number next to wavelet's name represents the vanishing moment[10].

In the present work, CWT namely Gabor wavelet was used to visualize the time-frequency analysis of the acoustic emission signals [97]. The wavelet function is provided as follows;

$$\psi(t) = \frac{\pi^{-\frac{1}{4}}\sqrt{(\omega_c}}{\gamma}.e^{-\left[\frac{t^2}{2}\left(\frac{\omega_c}{\gamma}\right)^2 + i\omega_c t\right]} \tag{3-27}$$

where, ω_c is the centre frequency, γ is constant (i.e. γ = 5.336) and satisfies the admissibility condition[11]. The freeware Vallen Wavelet [44,97] based on this algorithm was used for AE signal analysis. Correlation of Gaussian function with transient signals can reveal important characteristics about the signals. Gaussian modulation of a cosine function can be set according to the signal frequency of interest which is known as central frequency. The method was used in [98,99] to determine the time delay of the arrival signals for AE source localization. The Gaussian modulated cosine function can be written as follows;

$$x(t) = e^{-\frac{(t-t_{half})^2}{\sigma^2}}\cos(2\pi f t) \tag{3-28}$$

where;

$t -$ Discrete time of the signals

$t_{half} -$ Half time window of the of recorded signals

$f -$ Frequency of interest

$\sigma -$ The standard deviation of the Gaussian window which is specified according to the shape of signals to be obtained

[10] A mathematical definition for wavelets coefficients.

[11] The wavelet functions must satisfy the orthogonality.

A simple illustration of this function is shown in Figure 3-13. The correlation function ϕ_{xy} between Gaussian modulated cosine and transient signals can be described as follows:

$$\phi_{x,y}(\tau) = \lim_{T\to\infty} \int_{-T}^{T} x(\tau)\, y(t+\tau) d\tau \qquad (3\text{-}29)$$

From equation (3-29), the transient signal $y(t)$ is recursively correlated at various time lag intervals τ. The output is known as cross-correlogram or cross correlation function. Figure 3-14 provides an example of typical acoustic emission signal related to crack damage. The cross-correlograms with varying σ of Gaussian modulation are shown in Figure 3-15. In current work, the cross-correlograms were enveloped using the Hilbert transformation and superimposed with the original signal as shown in Figure 3-16. The Hilbert transform of the cross-correlogram is given as follows;

$$H\left[\phi_{x,y}(\tau)\right] = \tilde{\phi}_{x,y}(\tau) = \frac{1}{\pi}\int_{-\infty}^{\infty} \phi_{x,y}(\tau') \frac{1}{\tau-\tau'} d\tau' \qquad (3\text{-}30)$$

Hilbert transformation is generally used to extract real (ϕ) and imaginary ($\tilde{\phi}$) parts of a signal with 90° phase change. Using both imaginary and real values, the transformed cross-correlogram can be enveloped as follows;

$$\left|\phi_{x,y}(\tau)\right| = \sqrt{\phi^2{}_{x,y}(\tau) + \tilde{\phi}^2{}_{x,y}(\tau)} \qquad (3\text{-}31)$$

A similar technique was used by Okafor et al [98] on composite materials to estimate the time of arrival (TOA). The author used the time at the first peak rather than at the threshold crossing.

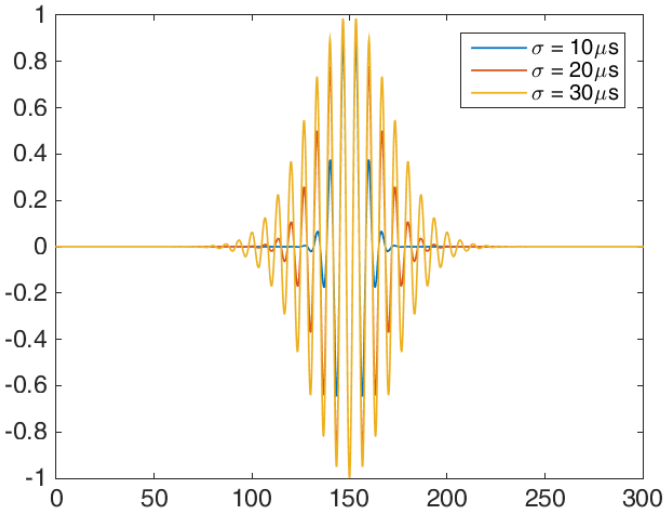

Figure 3-13 Examples of Gaussian modulated cosine signals of central frequency of 150 kHz of various standard deviations. Larger spreads of Gaussian modulations correspond to larger standard deviations.

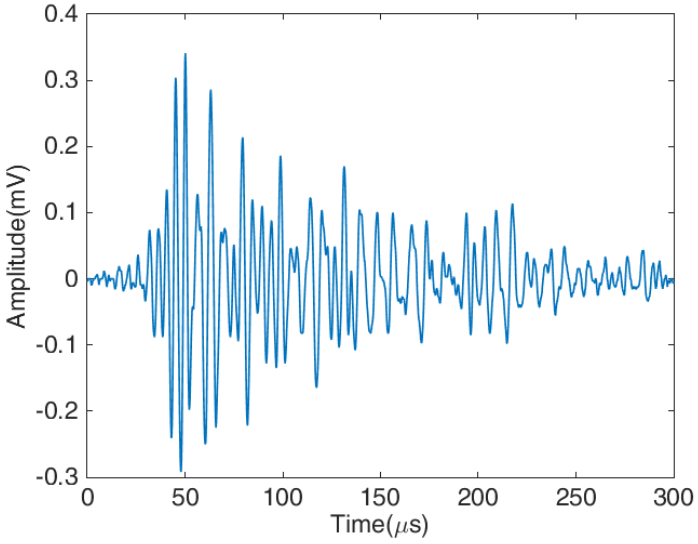

Figure 3-14 Typical AE signal associated with crack damage.

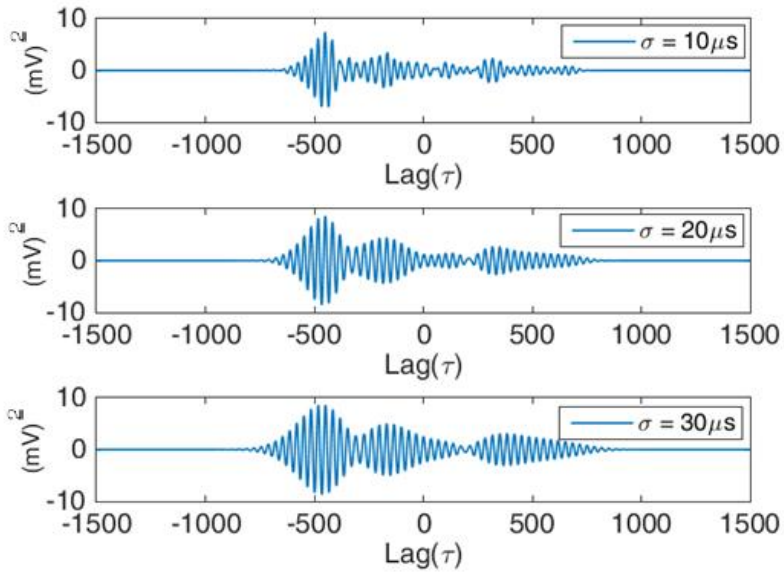

Figure 3-15 Cross-correlograms of AE signal with Gaussian modulated cosine of various standard deviations.

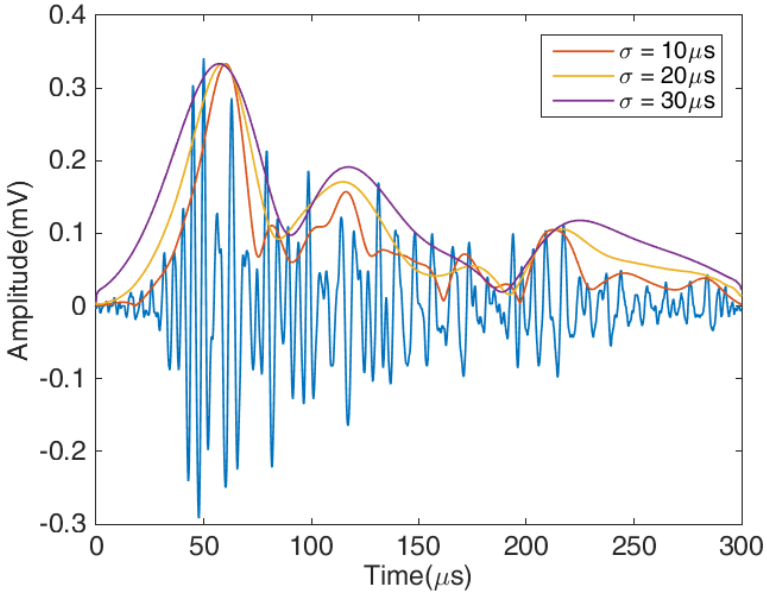

Figure 3-16 Superimposed of AE signal with the enveloped cross-correlograms. High correlation of signals is illustrated by the peaks of the envelopes.

Cross correlation is useful to identify wave modes and their time of arrival. It can also prevent error of time of arrival estimation due to signal dispersion. As mentioned in the previous section, SSMAL technique uses wave velocities of the fundamental wave modes to predict AE source locations. The technique can be mathematically described as follows;

$$D = \Delta t \left(\frac{V_{S0} V_{A0}}{V_{S0} - V_{A0}} \right) \tag{3-32}$$

where;

$V_{S0} -$ is the velocity of S_0 mode

$V_{A0} -$ is the velocity of A_0 mode

$\Delta t -$ is the time difference between the two signals

Using cross correlation, wave modes can be separated and hence, correlation of signals were used to identify wave modes. The arrival time can be estimated from the peak of the enveloped signals.

3.4 EXPERIMENTAL ANALYSIS

3.4.1 Carbon steel pipe

The experiment consists of a 7.2m length carbon steel pipe of API 5L X65/X70 which has the characteristics and properties given in Table 3-1. The pipe was welded with Butt welding joint at mid-span. Four wideband AE sensors (i.e. VS900-RIC with frequency range of 100kHz to 900kHz) with two sensors were placed in a ring configuration at each side of the pipe that is asymmetric about pipe mid-section as shown in Figure 3-17. The rings were rotated by 90° against each other. This is a minimal configuration of having sufficient number of sensors placed on this type of geometry given that at least three sensors are required for planar localization.

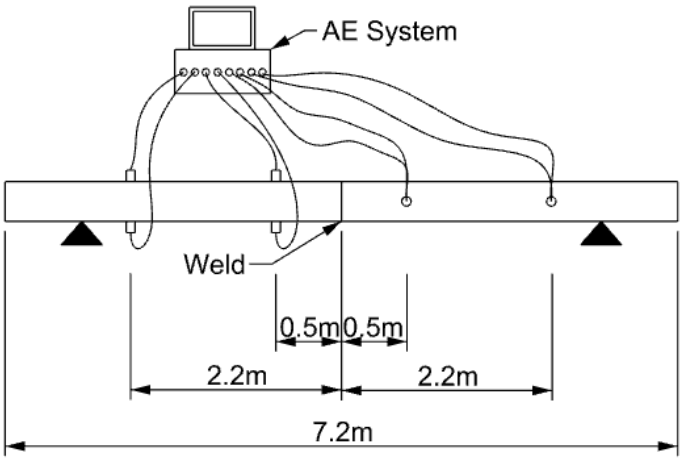

Figure 3-17 A schematic diagram of experiment setup

It is important to note that the pipe is relatively thick, therefore it is expected that Rayleigh waves are important in this structure. The arrangement of the sensors is such that the sensors are able to capture Rayleigh waves in the far-field. H-N sources or commonly known as pencil lead break (PLB) tests were excited around the weld circumference while wave pulses were generated using AE sensors. In order to study the propagating waves, distance from the AE sources was varied by modifying the distance between the rings. Two distances *L* were changed;

1) *L* = 50cm from the weld joint as illustrated in Figure 3-18
2) *L* = 220cm from the weld joint as illustrated in Figure 3-19

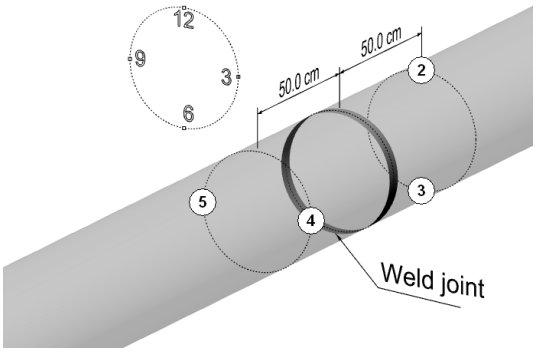

(a)

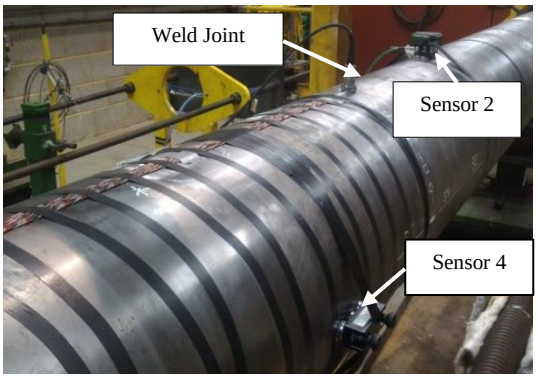

(b)

Figure 3-18 a) A schematic diagram of sensor locations (L = 50 cm from the weld joint) b) Actual locations of the sensors on the pipe.

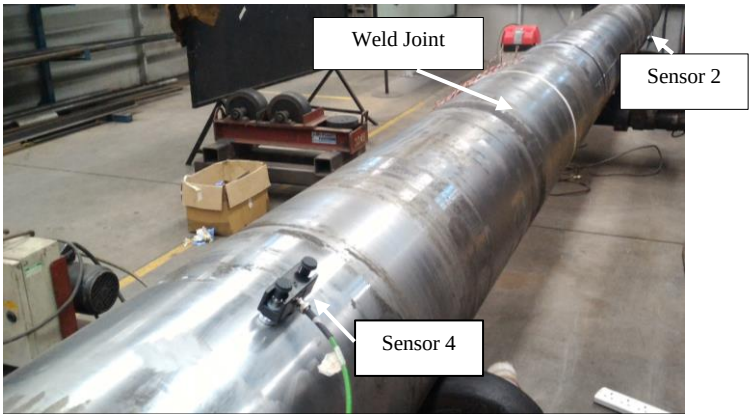

Figure 3-19 Afar sensor arrangement approximately L = 220 cm from the weld joint.

In the first sensor arrangement, the distance of H-N source generated at 12 o'clock to the nearest AE sensor is 50cm (i.e. L = 50cm from the weld joint). The maximum distance is approximately 78cm as depicted by a 2-D diagram in Figure 3-20. In this diagram, the y-axis and x-axis are the coordinates along the length and circumference of the pipe respectively. The H-N sources were generated at 3, 6, 9 and 12 o'clock. The pulses were generated using a Vallen sensor (i.e. VS900-RIC sensor [100]). Each sensor generated a pulse of 5.2μs width which forms a total of 4 sinusoids between 100kHz and 200kHz. The sensors were set with a threshold of 40dB which is the minimum noise level for the current setup. An example of a pulse signal is shown in Figure 3-21. The distance between the pulse sensor and the nearest AE sensor is 60cm i.e. either sensor 2, 3 or sensor 4, 5 as illustrated by the red coloured dimensions in Figure 3-20. The maximum distance is 104cm. The same setups were done for the second sensor arrangement i.e. L = 220cm. The calculated distances to all sensors from the various sources are detailed in Table 3-2.

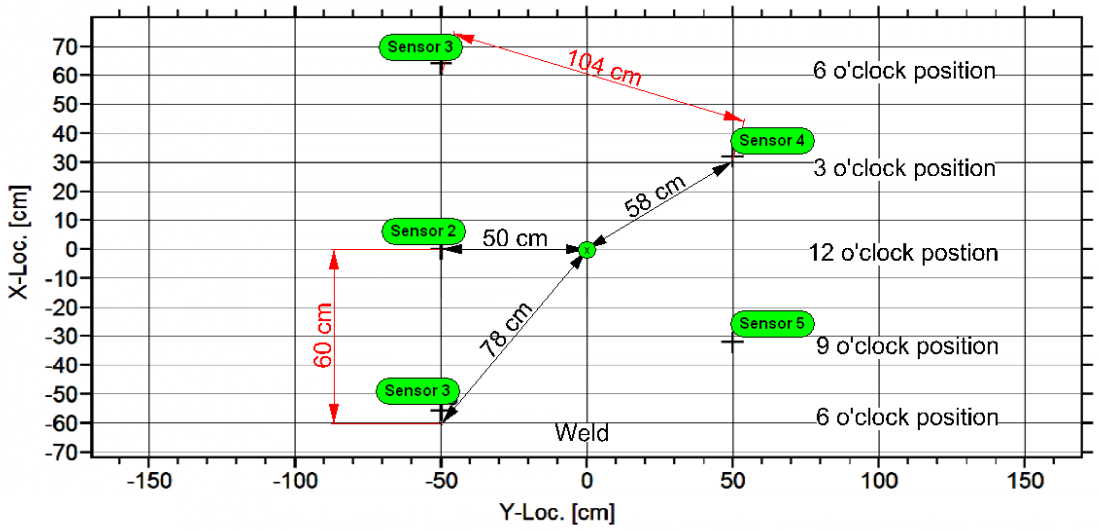

Figure 3-20 2-D planar diagram the pipe. The dimensions coloured in black shows the distances from the source initiated at 12 o'clock position, y=0. The dimension coloured in red is distance from the pulse generated by sensor 2.

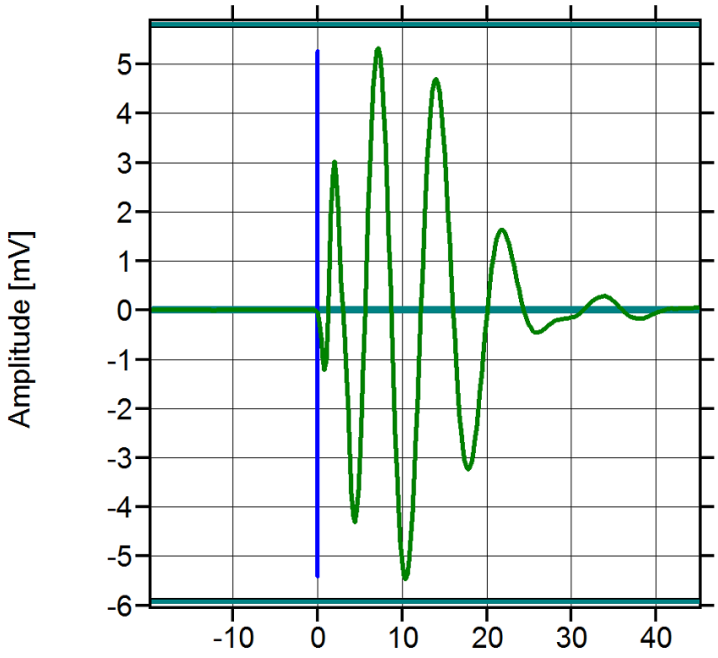

Figure 3-21 A pulse signal of central frequency of $150kHz$.

Source types	Sources	Distance from sensors	Distances (cm)	
			L = 50cm	L = 220cm
H-N	3 o'clock	4	50	220
H-N	3 o'clock	2,3	58	222
H-N	3 o'clock	5	78	228
H-N	6 o'clock	3	50	220
H-N	6 o'clock	4,5	58	222
H-N	6 o'clock	2	78	228
H-N	9 o'clock	5	50	220
H-N	9 o'clock	2,3	58	222
H-N	9 o'clock	4	78	228
H-N	12 o'clock	2	50	220
H-N	12 o'clock	4,5	58	222
H-N	12 o'clock	3	78	228
Pulse	Sensor 2	3	60	60
Pulse	Sensor 2	4,5	104	441
Pulse	Sensor 3	2	60	60
Pulse	Sensor 3	4,5	104	441
Pulse	Sensor 4	5	60	60
Pulse	Sensor 4	2,3	104	441
Pulse	Sensor 5	4	60	60
Pulse	Sensor 5	2,3	104	441

Table 3-2 The measured distance from H-N sources and AE pulses.

3.4.2 Thin aluminium plate

Lamb waves can be easily identified in thin structures due to their wavelengths larger than the structural thickness. The fundamental Lamb wave modes S_0 and A_0 can be clearly distinguished in a wide frequency range. An experimental test using an aluminium plate with the dimensions given in Table 3-1 was conducted to study Lamb wave propagation. The width of the plate is large enough to avoid the effect of wave reflection

from the side boundaries. The plate was mounted to a fixture at each end as shown in Figure 3-22-a. H-N sources were generated at mid-span as illustrated in Figure 3-22-b. The generated waves propagate in a direct path towards the AE sensors located in the centre along the plate axis. Vallen VS900-RIC sensors [100] were used to record signal received above the 40dB threshold. The sensors were mounted using electrical tapes due to difficulty to use magnetic mount. A calibration was done prior to the test to ensure both sensors recorded similar readings.

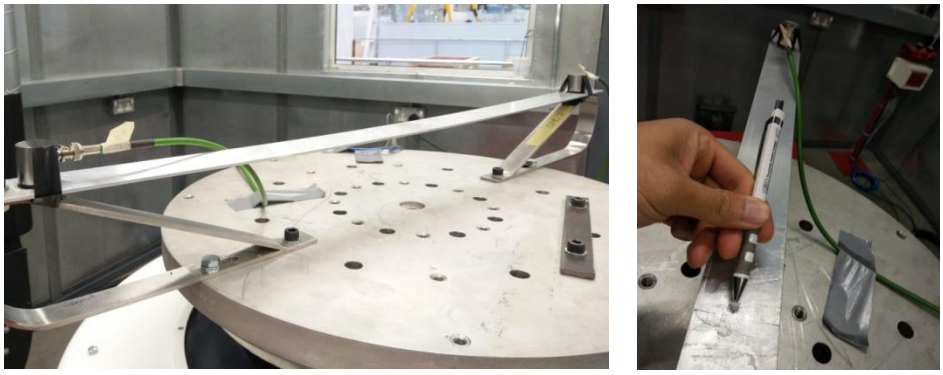

(a) (b)

Figure 3-22 a) AE sensor locations on the aluminium plate. b) An illustration of H-N/PLB sources conducted at the mid-span.

3.5 RESULTS AND DISCUSSION

3.5.1 Carbon Steel Pipe

3.5.1.1 Case 1: L = 50cm from the weld joint

AE pulses were generated alternately by each sensor. The average speeds were calculated by Vallen system which records the time of arrival of AE signals at each channel. The calculated average wave speeds rounded to the nearest whole numbers as reported by Vallen [44] is given in Table 3-3.

Sensors	2	3	4	5
2	-	5450 ms^{-1}	4419 ms^{-1}	4464 ms^{-1}
3	5449 ms^{-1}	-	4383 ms^{-1}	4451 ms^{-1}
4	4422 ms^{-1}	4413 ms^{-1}	-	5331 ms^{-1}
5	4468 ms^{-1}	4452 ms^{-1}	5291 ms^{-1}	-

Table 3-3 Wave velocities calculated based on TOA recorded at each channel for L = 50cm.

The average velocity recorded by all channels was approximately 4749ms^{-1}. The highest velocity calculated was approximately 5450ms^{-1}. A number of burst signals including the reflected waves from boundaries were also recorded. The signals were led by smaller amplitude signals as shown in Figure 3-23 (top). The out-of-plane excitation by AE pulses generated symmetric and asymmetric wave modes which can also be seen by the wavelet transform as shown in Figure 3-23 (bottom). The asymmetric wave modes have larger amplitudes. Examples of the signals acquired by sensor 2, 3 and 4 for pulses generated by sensor 5 are illustrated in Figure 3-23 to Figure 3-25.

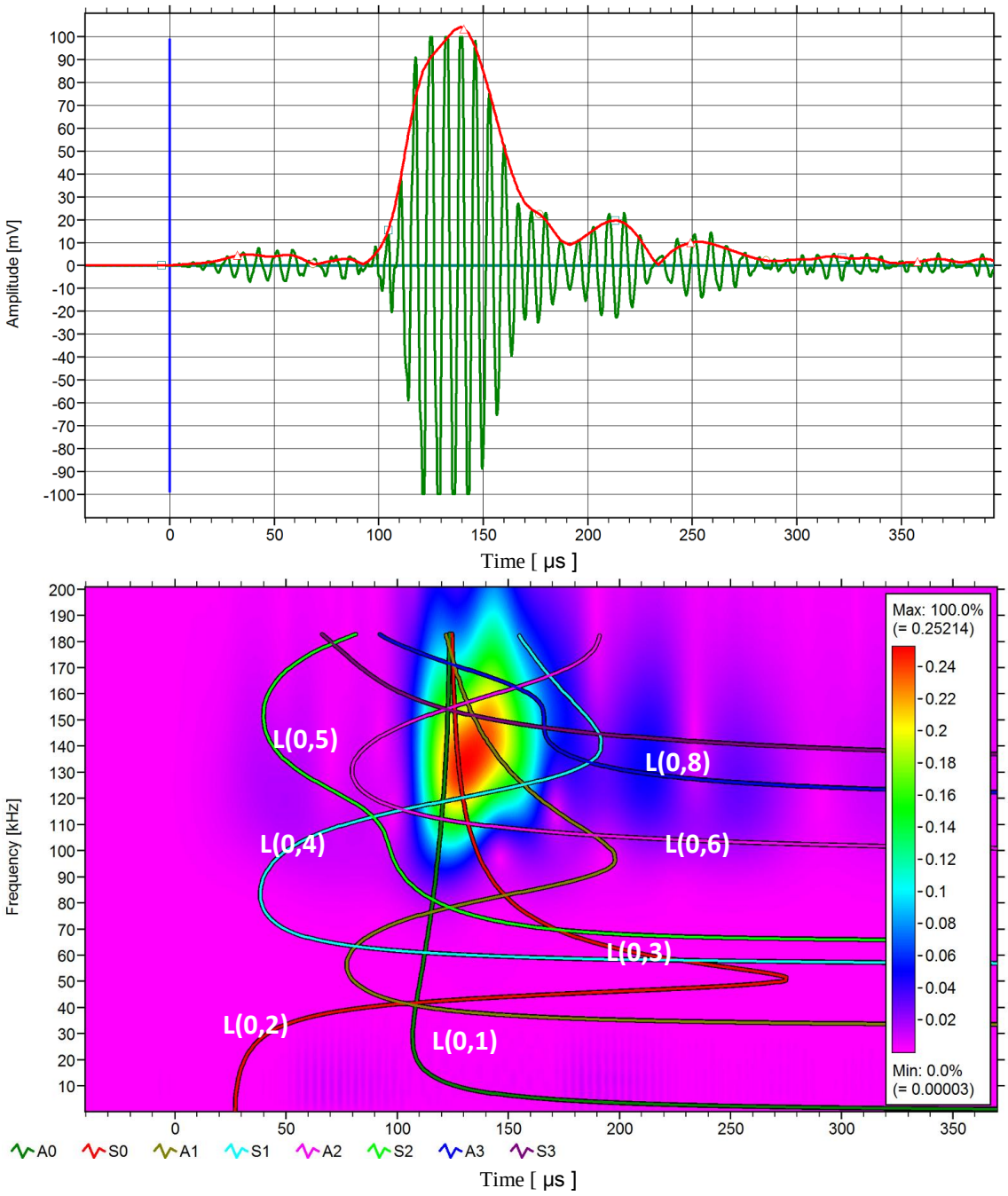

Figure 3-23 The signal recorded by channel 4 (Top). Wavelet transform of the signal (bottom) overlapped with dispersion curves, for *L*=50cm.

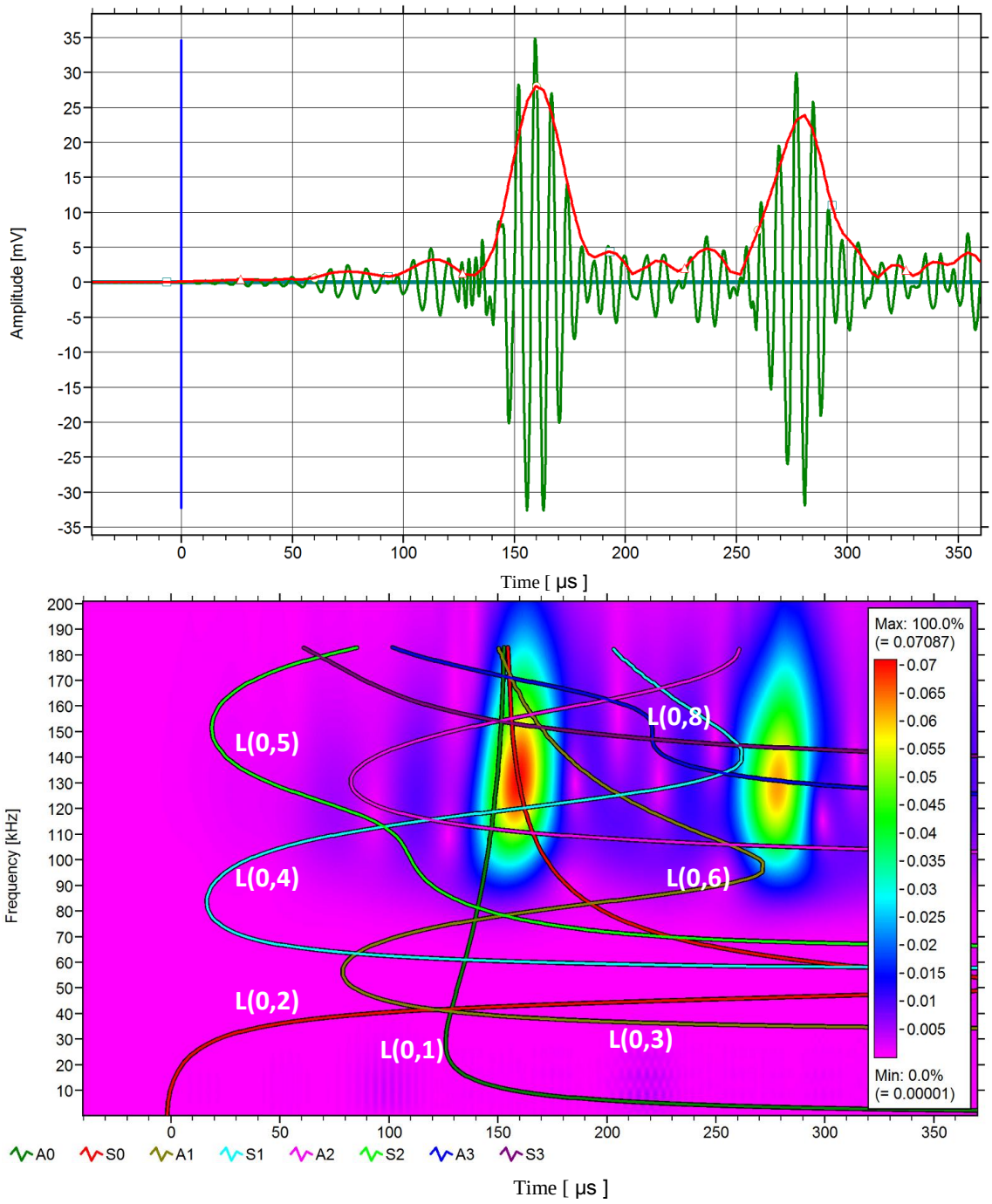

Figure 3-24 The signal recorded by channel 2 (Top) and the wavelet transform of the signal (bottom) with overlapped dispersion curves for *L*=50cm.

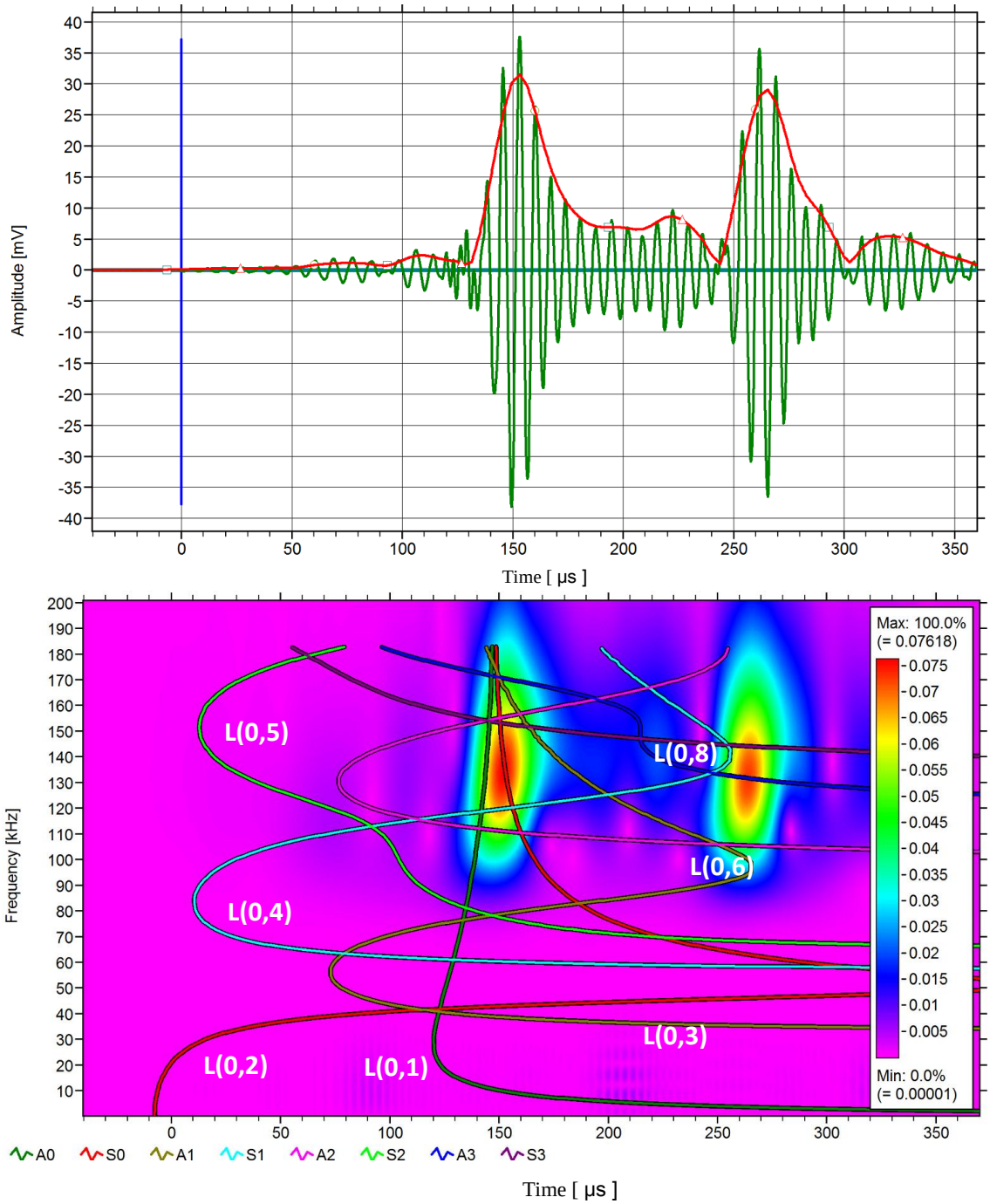

Figure 3-25 The signal recorded by channel 3 (Top) and the wavelet transform of the signal (bottom) with overlapped dispersion curves for *L*=50cm.

The AE signals recorded by the nearest sensor (i.e. sensor 4) have larger amplitude asymmetric waves. The symmetric wave signals arrived earlier as expected. The asymmetric waves arrived later as shown by the wavelet transform (see Figure 3-23

bottom). Given that elastic waves are dispersive, the phase and group velocities of each wave mode vary with frequencies, and hence it is difficult to identify the oncoming waves since there are many waves overlap. The wave modes were distinguished using the calculated dispersion curves overlapped with wavelet transform. It was identified that the arrival wave is the L(0,5) instead of the fundamental waves. An estimation of the time difference between the frontal wave and the subsequent waves can be calculated by taking the velocity at $180kHz$ (refer to the dispersion curve in Figure 3-8). The selected frequency was based on the frequency of the recorded waves. According to the dispersion curves the phase velocity of the S_2 wave mode or L(0,5) is approximately $5000ms^{-1}$ while the asymmetric waves are propagating at approximately $3000ms^{-1}$. The difference between these waves and the frontal wave can be estimated analytically using wave velocities and distance between the sensors as follows; $60cm/5000ms^{-1} - 60cm/3000ms^{-1} = 80\mu s$. Another way of calculating the wave velocities can be done using the time difference of the frontal wave and the asymmetric waves using Gaussian correlation with an artificial wave of centre frequency of $180kHz$ as shown in Figure 3-23 (red curve in the top figure). The arrival time of the first envelope peak is approximately $50\mu s$ while the arrival time of the largest envelope is approximately $130\mu s$. The time difference (i.e. $130\mu s$ - $50\mu s$) is similar to the analytical calculation. This is the principle behind SSMAL technique which uses time difference of S_0 and A_0 modes. Using the calculated average velocity, the located events/calculated sources were calculated as shown in Figure 3-26 and Figure 3-27 respectively.

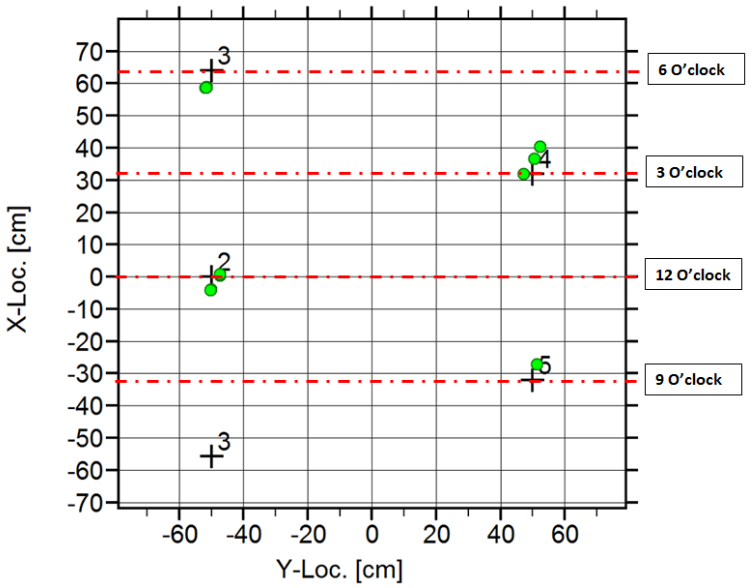

Figure 3-26 The located events of the generated AE pulses represented by green dots.

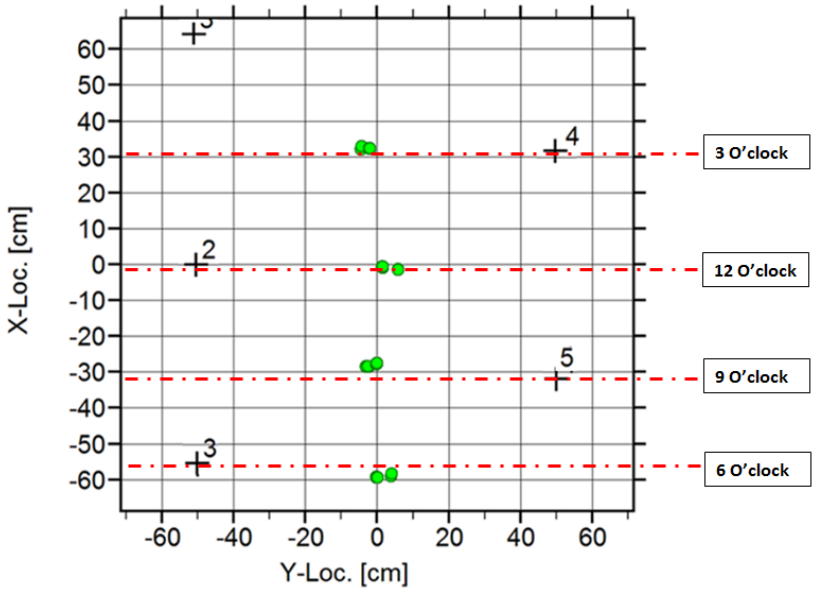

.

Figure 3-27 The located events of the generated H-N sources at various locations on the pipe which represented by green dots.

3.5.1.2 Case 2: L = 220cm from the weld joint

The average wave velocity is $3903ms^{-1}$. The velocity range is greater than the first case since the maximum distance between sensors is larger. However the shortest distance is similar to the first case. The frontal wave mode can be seen clearly which is the S2 wave

mode or L(0,5) as shown in Figure 3-28 which records the highest velocity of 5674ms^{-1}. However, the majority of the calculated velocities are lower as given in Table 3-4.

Sensors	2	3	4	5
2	-	5568 ms^{-1}	3476 ms^{-1}	3456 ms^{-1}
3	5553 ms^{-1}	-	3446 ms^{-1}	3530 ms^{-1}
4	3435 ms^{-1}	3419 ms^{-1}	-	5427 ms^{-1}
5	3425 ms^{-1}	3586 ms^{-1}	5674 ms^{-1}	-

Table 3-4 Wave velocities calculated based on TOA recorded at each channel for far sensor arrangement, (L=220cm).

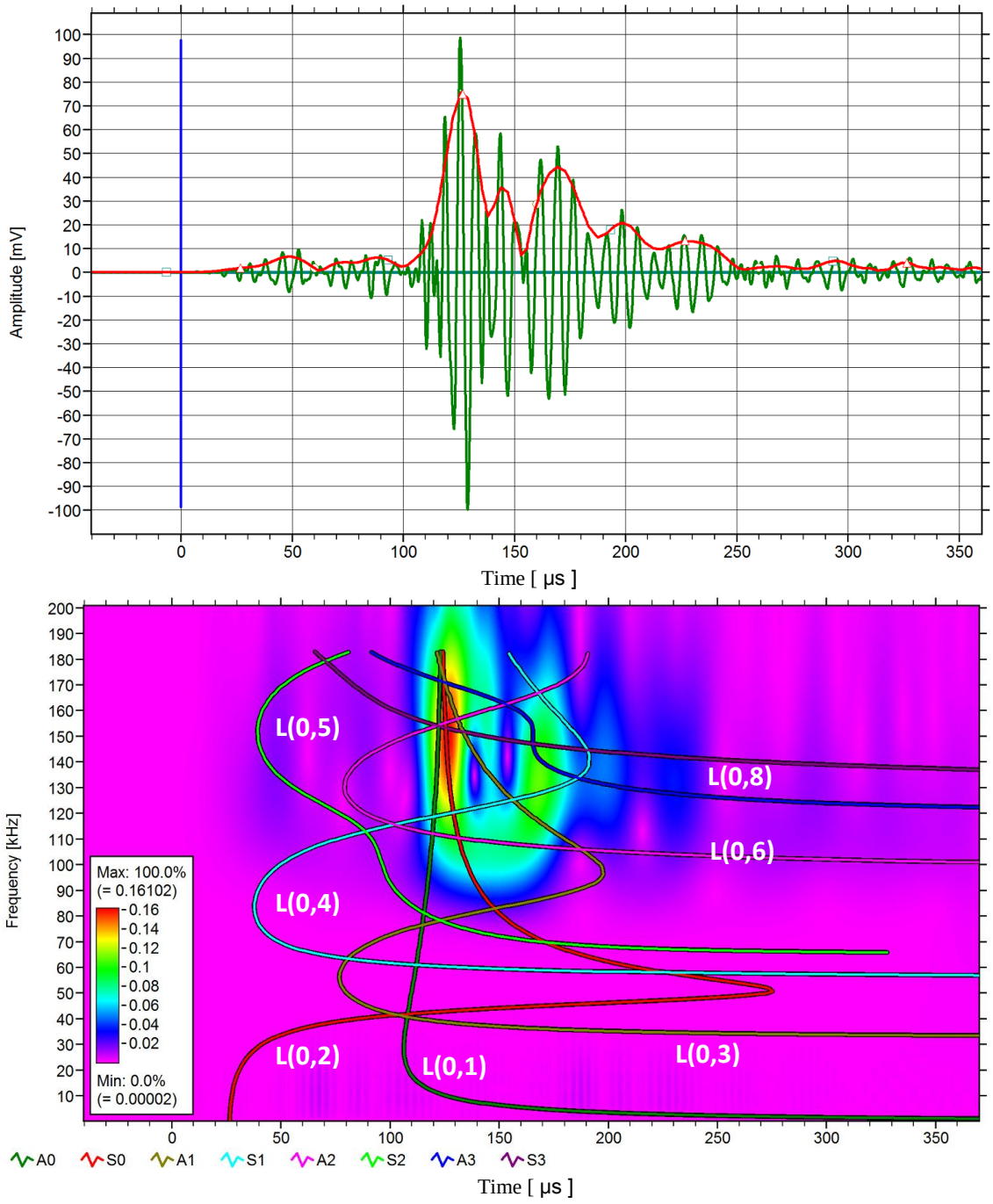

Figure 3-28 The signal recorded by channel 4 (Top) and the wavelet transform of the signal (bottom) for *L*=220cm.

The signals consist of various wave modes as shown in Figure 3-29 and Figure 3-30. The largest peak amplitudes are believed to be a combination of many wave modes. The attenuation of symmetric wave modes delayed the arrival waves recorded by sensor 2 and

3. However the signal recorded by the nearest sensor (i.e. sensor 4) was triggered by the symmetric wave mode similar to the previous case.

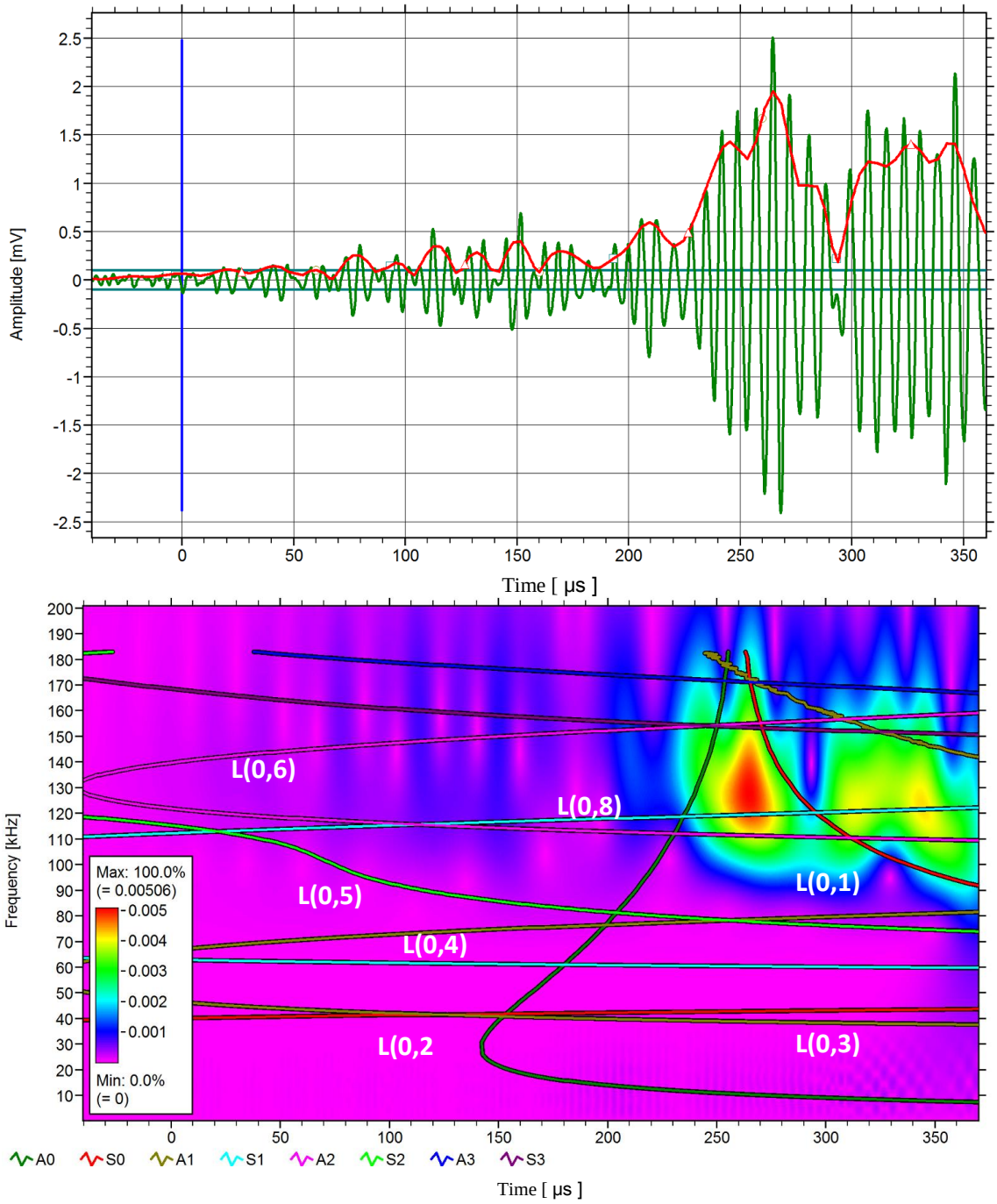

Figure 3-29 The signal recorded by channel 2 (Top) and the wavelet transform of the signal (bottom) for *L*=220cm.

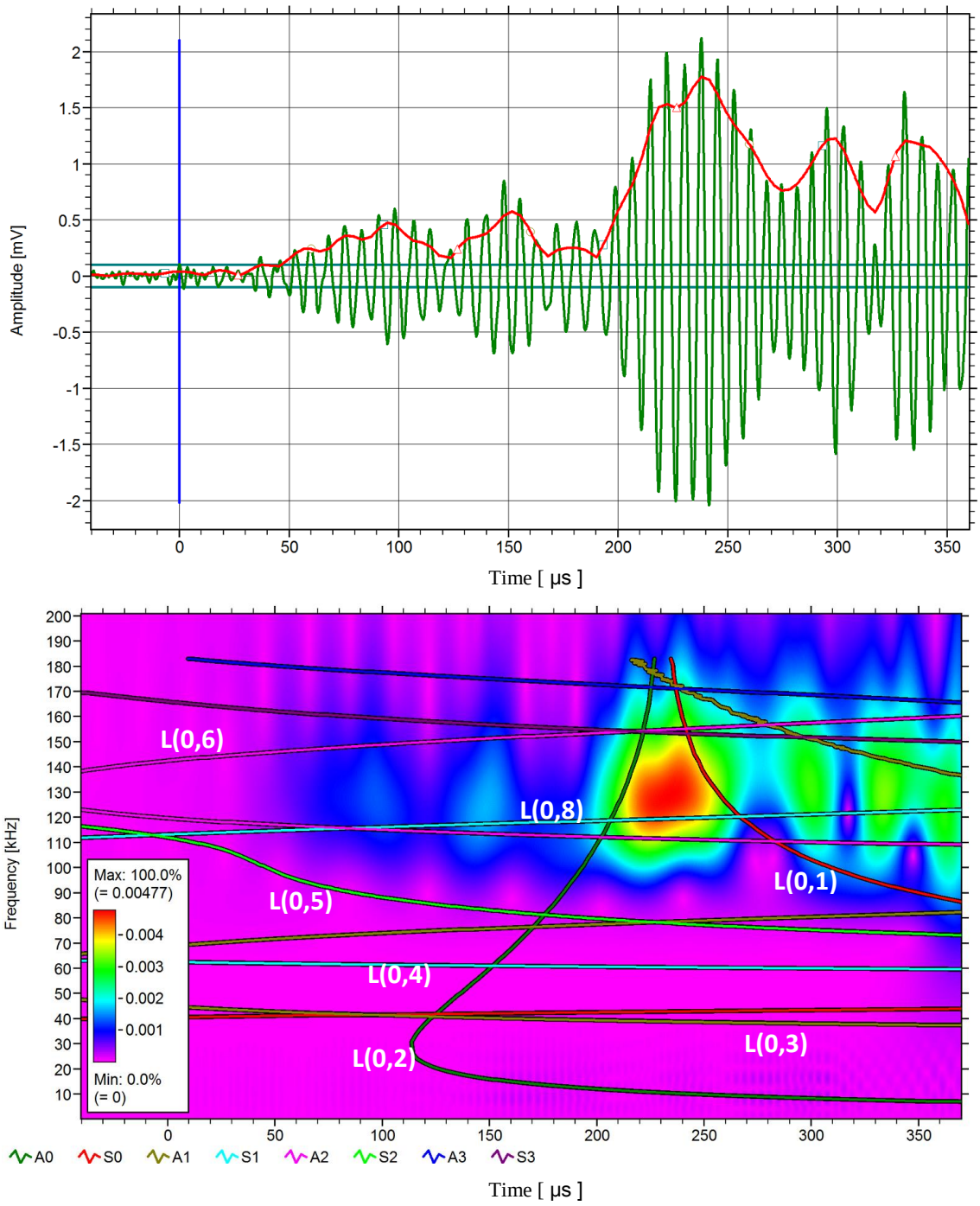

Figure 3-30 The signal recorded by channel 3 (Top) and the wavelet transform of the signal (bottom) for *L*=220cm.

The inconsistency of the arrival waves causes errors on the source localization as shown in Figure 3-31. The located events depend on the time of arrival of the waves exceeding

the thresholds. Therefore the wave velocity of the arrival waves of different wave modes that travels at different velocity than the fundamental waves cause this problem.

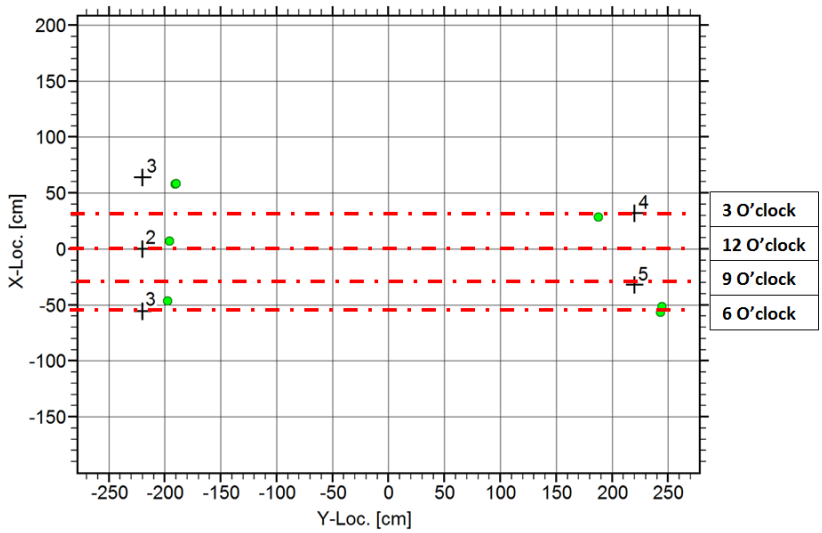

Figure 3-31 The located events generated at various locations on the pipe which represented by green dots

The high amplitude waves are travelling at lower speed than the shear wave velocity in generic steel structure, which represents the Rayleigh waves. The tests were repeated with pencil lead breaks (PLB) around the weld with the threshold increased to 60dB to remove the smaller amplitude signals. By setting the velocity to 3000ms^{-1}, the event was located correctly as illustrated in Figure 3-32. Therefore using a high threshold setting, the acquisition would be triggered by the Rayleigh waves, which could eliminate errors of the predicted source locations.

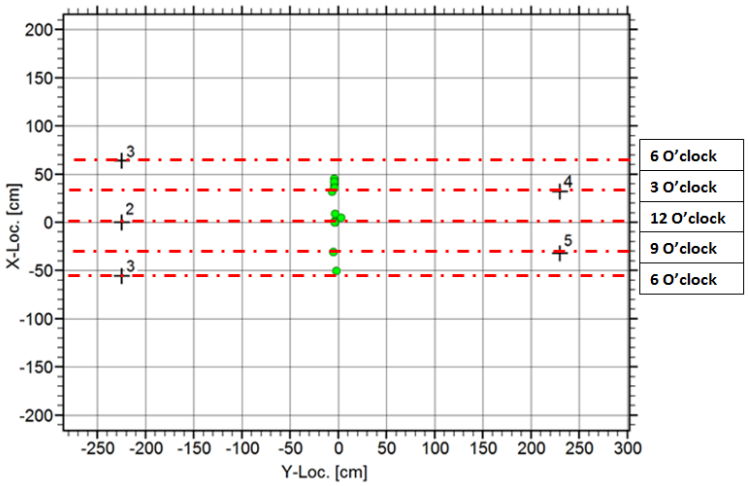

Figure 3-32 The located H-N sources (PLB) generated at various locations on the pipe which represented by green dots

3.5.2 Thin Aluminium Plate

A number of PLB sources were generated at mid-point between the two sensors. The distance from the mid-point to the sensors is 45cm. The signal acquired by one of the sensors is shown in Figure 3-33 (Left).

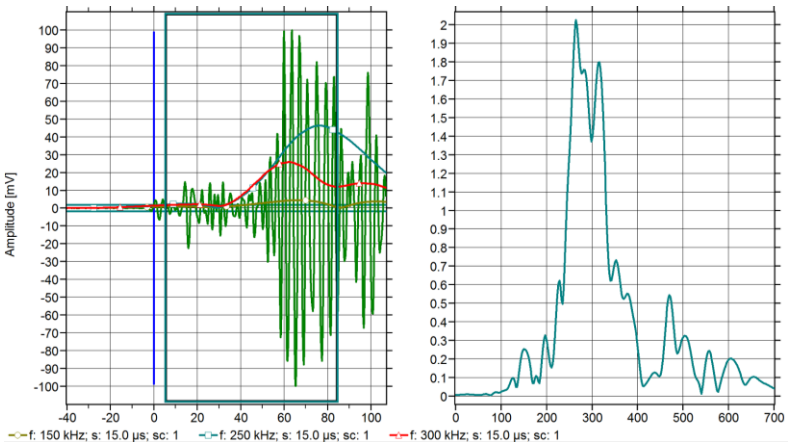

Figure 3-33 An example of AE signal acquired by one of the sensors, overlapped with signal envelope of various central frequencies (left). Fourier transform of the signal (right).

As can be seen in Figure 3-33 (left), there is distinction of symmetric wave S_0 and asymmetric wave A_0. The Fourier transform of the signal is shown in Figure 3-33 (right). The dominant frequency was calculated approximately $250kHz$. Therefore the signal was cross correlated with a Gaussian modulated cosine signal of central frequency $250kHz$. The standard deviation of the Gaussian function was set to $15\mu s$, which correspond to signal bandwidth of $100Hz$. The cross-correlogram was then enveloped using Hilbert transform. The time difference between S_0 and A_0 were determined according to the time of the envelope peaks which are summarized in Table 3-5;

Central frequency	S_0 wave velocity (ms^{-1})	A_0 wave velocity (ms^{-1})	Time difference between S_0 and A_0, $\Delta t\ (s)$	Calculated source location, SSMAL (cm)	Source localization percentage error, %
250	5290	3085	65.6	48.6	7.9

Table 3-5 S_0 and A_0 wave velocities and time difference between the wave modes based on the peak values of the enveloped cross-correlogram. The source location was predicted using SSMAL technique.

The S_0 and A_0 wave velocities were determined from the dispersion curves given in Figure 3-10. The calculated location of the PLB source is 48.6cm (i.e. 7.9% error from the actual source location). The cross correlation with Gaussian function depends on the spread of the modulated signal. In order to observe such variation, the standard deviation, σ was varied for $5\mu s, 10\mu s, 15\mu s, 20\mu s, 25\mu s$. Figure 3-34 shows the envelope of cross-correlogram according to various σ.

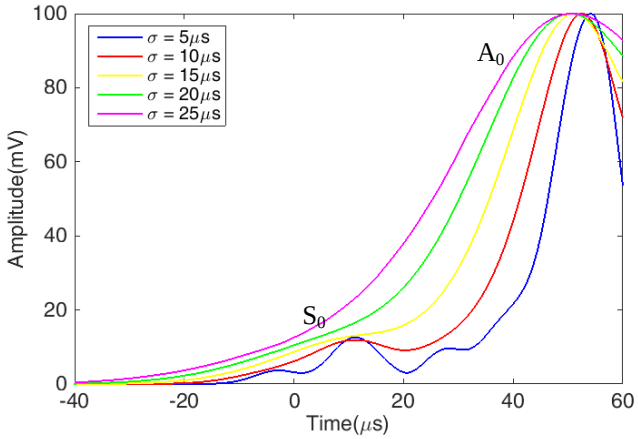

Figure 3-34 Spread of signal envelope according to various σ.

Although the S_0 wave mode is less dispersive, the effect of different σ shifts the peak values and hence the arrival time. Larger σ makes the wave identification difficult due to lack of signal correlation. To find the optimum σ, a study was conducted for every $1\mu s$ increment between $5\mu s - 15\mu s$. The summary of the calculated arrival time and located sources are tabulated in Table 3-6.

σ (μs)	Time difference between S_0 and A_0, Δt (s)	Calculated source location, SSMAL (cm)	Source localization percentage error, %
5	58.2	43.1	4.3
6	58.6	43.4	3.6
7	59	43.7	3.0
8	59.6	44.1	2.0
9	60.4	44.7	0.7
10	61.2	45.3	0.7
11	62	45.9	2.0
12	63	46.6	3.6
13	63.8	47.2	4.9
14	64.6	47.8	6.2
15	65.6	48.6	7.9

Table 3-6 The calculated source locations using SSMAL technique for different values of σ.

The Gaussian modulation of standard deviation $9\mu s$ and $10\mu s$, which correspond to signal bandwidth of approximately $60Hz$, provide the most accurate of the calculated source location with 0.7% error.

3.6 CONCLUDING REMARKS

This chapter presents considerations related to the wave propagation characteristics in thick and thin structures. The study covers Level 1 and Level 2 of the SHM strategy using acoustic emission technique. A number of test set up conditions obtained by varying the measurement distances from AE sources were studied. The dispersive signals were decomposed into various wave modes using wavelet transformation and cross correlation with Gaussian modulated cosine signal. For the study of waves on a thick pipe, various distances of AE sensors from AE pulses and PLBs were studied. The

average velocity for close arrangement of sensors was measured consistently. Using wavelet transformation, the wave mode that triggered the acquisition was identified to be the L(0,5) mode. This wave mode is equivalent to the S_2 wave in plates. However for far-field sensor arrangement the waves that triggered the acquisition were no longer the L(0,5) mode due to attenuation. Such discrepancy has caused errors to the calculated event locations. The velocity of the high amplitude signals was measured approximately equivalent to the shear wave velocity, such waves being predominantly Rayleigh waves. Using a high signal threshold and the calculated Rayleigh wave velocity, the events around the weld were determined correctly. Although wave mode identification is difficult in thick structures, the use of Rayleigh waves was found effective removing the need to identify smaller amplitude wave modes. In the second part of this chapter, an aluminium plate was used to study Lamb wave propagation on a thin plate. PLB sources were generated at mid-point between two AE sensors. Wave mode identification was much easier since the fundamental modes can be distinguished in a larger frequency range. To calculate the source locations, a Single Sensor Modal Analysis location (SSMAL) technique was used. This technique uses Lamb waves by manipulating the time delay of symmetric, S_0 and asymmetric, A_0 waves. The sources were calculated based on the velocities of the two different wave modes. In order to determine the correct arrival time, AE signals were cross correlated with Gaussian modulated cosine signals. This technique removes the effect of dispersion and reveals only those waves that contain a specific signal frequency. Wave dispersion is the factor that causes error to the SSMAL technique in practical testing conditions. Using the Fourier transformation, the largest amplitudes from the PLB tests consist of signal frequency of $250kHz$. It was found that $\sigma = 9\mu s$ or $10\mu s$ which corresponds to the signal bandwidth of $60Hz$, gives the least error of the calculated events compared the actual PLB locations. σ is an independent parameter that controls the spread of Gaussian function. Using the velocities of S_0 and A_0 and the time difference calculated using cross correlation, the events were correctly calculated within 0.7% error. This study shows that using cross correlation of acoustic emission signals with Gaussian modulated cosine signal enhances wave mode identification, and hence improves source localization by SSMAL technique.

CHAPTER 4

ACOUSTIC EMISSION MONITORING OF A RESONANT FATIGUE PIPE

4.1 BACKGROUND

A number of inspection techniques and monitoring systems are available however their applications are not specific to address vibration-induced fatigue problem in piping and pipelines. Guidelines have been published [3] which provide strategic assessment programs to identify the threats of vibration-induced fatigue in piping systems and offer a framework for quantitative assessment to determine the risk of damage. The output from the assessment is used to quantify the integrity of piping systems. The general practice of vibration assessment is that damage can be inferred from the change of dynamic characteristics such as mode shapes, modal damping and natural frequencies. However the change of these parameters may be insignificant for structures that suffer from fatigue cracks due to negligible change of structural stiffness. This problem is crucial for any pressurized equipment such as piping or pipeline with the possibility of loss of containment. An alternative way to detect this problem is to use stress waves generated during the onset of cracking. The generated stress waves propagate within the structure can excite measurement sensors placed on the external surface. This method is known as passive measurement technique, which is the fundamental principle of acoustic emission (AE). There are several published papers [12,14–16] that summarized different techniques and approaches regarding damage detection in structural health monitoring. Generally, selection of features can be categorized as parametric-based or signal-based [18,101] methods. The signal-based method employs signal processing techniques which evaluate signals directly in the time domain, frequency domain or time-frequency domain. Examples of these methods are the auto-regressive (AR) model and auto-regressive moving average (ARMA) [22–24], [102] model for linear or non-linear

problems. The parametric-based method is based on explicit parameters derived from measurements [103–105]. These parameters can be used for model updating to evaluate structural modal parameters by numerical methods [19,20,106–108]. Acoustic emission monitoring of piping subjected dynamic loadings received less attention due to large uncertainties associated with measurement. The signals are also susceptible to noise. In this chapter, a Bayesian estimation procedure was proposed to estimate parameters derived directly from the recorded signals to evaluate uncertainties of the calculated events. Bayesian estimation takes advantage of large database with less computational power in making inference about the underlying distributions. This method is considered novel since there is no similar research in the past using Bayesian estimation for source localization and uncertainties evaluation. The method is found useful to ascertain damage sources and can be used with other damage identification methods in evaluating weld condition in resonance fatigue test [109,110]. The work presented in [109,110] mainly used dynamic strain measurement to assess fatigue damage against the S-N curves.

4.2 ANALYSIS AND EXPERIMENTAL PROCEDURES

In signal-based methods, the amount of data received can be prohibitively large which may require high computational power to condense large signals into meaningful results. The premise of using signal-based method in AE is usually to obtain time of arrival for source localization. It is important to note that the generated waves resulting from defects consist of many modes due to interaction with geometric boundaries. Lamb waves travel with different velocities at different frequencies. This can cause problem for wave mode identification. In general, high frequency waves suffer high attenuation and hence the fundamental wave modes such as symmetric, S_0 and anti-symmetric waves, $A_{0,}$ in plate-like geometry are usually identified. However, waves in pipes have additional modes which include the extensional, flexural and torsional modes. The commonly used features in AE for damage identification include “count” (i.e. the number of times AE signals cross threshold), “burst energy” (i.e. the integral of squared signal amplitudes over its duration), and “signal rise time” (i.e. the time difference between the first threshold crossing and peak amplitude) [111]. The parametric-based methods were used in many

aspects for damage detection [54,57,112,113] and prognosis [62,64], however they depend on the threshold setting for signal detection. In this chapter "burst energy" and "count" were used for damage detection. For validation with AE signals, strain history was recorded. The premise of using strain history is that the change of strain frequency correspond to damage evolution [114–116], due to the change in strain modes [117], [118]. The strain data is not presented in this work to preserve confidentiality. The data belongs to a collaborative project with Technology Welding Institute (TWI) limited, which cannot be disclosed due to commercial agreement. However, for completeness, normalized strain is presented to illustrate dynamic strain behaviour. Strain gauges can be effective to measure vibration [119–121] although it has some limitation such as low signal to noise ratio. In the current research, it is considered that under normal conditions without damage, the measured strain frequency is similar to the vibration frequency. Damage may increase the measured frequency due to crack opening and closing, and other non-linearity effect [122]. During fatigue tests in this research, the cycles were determined based on the peak counting method, aiming to estimate the actual number of cycles which provides an indication of damage. The similarity and differences between AE features and strain measurements were discussed.

4.2.1 Signal Processing Method

Acoustic Emission sensors are highly sensitive to environmental noises. Identifying useful signals in a noisy background is crucial in many applications, particularly to detect the onset of damage. Such problem has been discussed greatly by Pollock [123]. In this chapter a Bayesian estimation procedure based on Acoustic Emission signals was employed for a resonance fatigue test. Bayesian estimation was proposed due to the fact that:

- The *prior* probability distributions related to damage can be established from historical data.
- The estimation takes into account the current evidences. The model can be used with parameters obtained at different time independently.

- Bayesian analysis takes advantage of large data and makes inference about the underlying parameters while giving an evaluation of uncertainties occurring in the process.

4.2.1.1 Short Time Fourier Transform (STFT)

Fourier basis function consists of sine and cosine functions. The transformation is obtained over a specified data length where signals tend to be truncated, this leading to spectral leakage (i.e. spread out in frequency domain). The truncation problems are usually avoided by using window functions [124] applied to the signals such as rectangle, Blackman, Hamming, Hanning, among others. STFT uses a single window for all signals [93] as illustrated in Figure 4-1. STFT is inferior to wavelet transformation in that wavelet transformation uses scaled-varying functions for various window sizes as demonstrated in the previous chapter. However, STFT is considered a robust method to analyse vibration data since low order vibration mode is considered in the present research (e.g. bending mode).

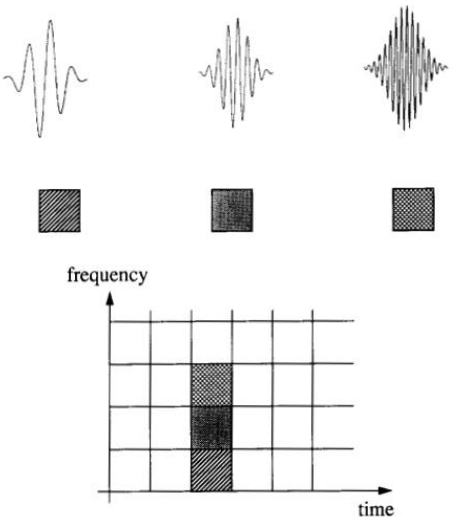

Figure 4-1 Fourier basis function and coverage of time-frequency tiles (STFT)

4.2.1.2 Bayesian Estimation

Bayes's Theorem is attributed to Reverend Thomas Bayes (1702-1761). The foundation for Bayesian methods is based upon the 'degree-of-belief' interpretation of probability.

The 'belief' is updated upon 'seeing' evidence, which updates the distribution of parameters. Statistical inferences can be made from the updated distributions either by point or interval estimates [125,126], such as the mean values of the *posterior* distributions. Bayesian estimation consists of a *prior* probability distribution, $P(\theta)$ which is the initial hypothesis of random parameters that cannot be measured directly. It represents the distribution of the sought-after parameters before considering any observations (i.e. the input data). In this work the prior knowledge is assumed to follow the distribution obtained from the pencil lead break tests, which is considered the most relevant method to simulate cracks. The quality of the process depends on the likelihood function $P(D|\theta)$ which finds the most probable data set for different values of θ. Bayes's theorem can be written as follows [107];

$$P(\theta_t|D_t) = \frac{P(D_t|\theta_t)p(\theta_t)}{\int_{-\infty}^{\infty} P(D_t|\theta_t)p(\theta_t)d\theta_t} \tag{4-1}$$

where;

θ_t - The predicted variables

D_t - The observed data

The subset *t* denotes data at different time intervals. Acoustic emission signals are susceptible to extraneous noises and such signals may consist of burst-like signals, which are normally associated with cracks, or continuous signals correspond to plastic deformation, boundary sliding and dislocation movement in crystal lattices [35,127]. Continuous signal may also be generated from continuous rubbing of materials in contact during dynamic motion. Based on this fact, the signals can be discriminated using Bayesian methods such that, the generated events can be further filtered so that only those signals having high probability of crack related events are obtained.

4.2.1.3 Cross Correlation of Signals

Cross correlation is a method which finds correlation between two signals. The mathematical formula is given in (3-29). The method is useful to measure similarity [128] or their time differences for source localization [99]. The cross correlation function is a

matrix of cross correlation values or known as cross-correlogram obtained by shifting one signal relative to the other. These values are based on the length and amplitude of signals. The maximum cross correlation value is normalized by autocorrelation of each signal at zero lag to obtain a cross correlation coefficient between zero and one as follows;

$$\bar{\phi}_{i,j} = \frac{max\left|\phi_{i,j}(\tau)\right|}{\sqrt{\phi_{i,i}(0)\phi_{j,j}(0)}} \tag{4-2}$$

where;

$\phi_{i,j}(\tau)$ is the cross correlation function of lag τ

$\bar{\phi}_{i,j}$ is the cross correlation coefficient of signals i and j

$\phi_{i,i}(0)$ is the autocorrelation of signals for sensor i at lag zero

AE signals are susceptible to extraneous noise and may consist of burst-type signal that is normally generated from rapid releases of energy such as cracks. Continuous signals are usually associated with plastic deformation in material [35,127]. Continuous emission can also be generated due to rubbing of materials in contact during dynamic motion. The significance of using cross correlation for AE signals is that some signals with a specific characteristic can be distinguished from other signals detected at the same instance. In AE method, signals detected above threshold are mainly regarded as events. The located events or predicted source locations are not always correct. The errors could be due to delay of time of arrival or falsely detected signals. In the current research, Bayesian estimation is inferred from a set of parameters derived from a set of time series signals represented by the effective coefficients (EC). EC takes into account correlation coefficients from all possible sensor/signals combinations. The relationship can be described as follows;

$$\mathrm{EC} = \alpha(Minimum\ \bar{\phi}_{i,j}) \tag{4-3}$$

where;

α is the correction factor $Minimum\ \bar{\phi}_{i,j}/Maximum\ \bar{\phi}_{i,j}$

$\bar{\phi}_{i,j}$ is the cross correlation coefficient of signals i and j

EC measures a minimum degree of similarity of the correlated signals taking into account the maximum and minimum cross correlation coefficients of any two signals from the located events. Using this relationship, if all signals are perfectly similar then the ratio $Min\ \bar{\phi}_{i,j}/Max\ \bar{\phi}_{i,j}$ is equal to one. Therefore, the EC in this case is also one. If only two out of three signals are similar, then the less correlated signals reduce the calculated EC. An example of this is illustrated in Figure 4-2. The signal which is different in b) that is continuous rather than a short burst is at sensor 1. Using this relationship any located event that has high EC means the signals are similar. However, the coefficients calculated by cross correlation are highly dependent on the lengths and amplitudes of the signals which have an impact on the measured EC. A number of PLBs were carried out around the weld circumference to obtain a range of EC values for signal lengths between 50μ and $500\mu s$ in increments of $50\mu s$.

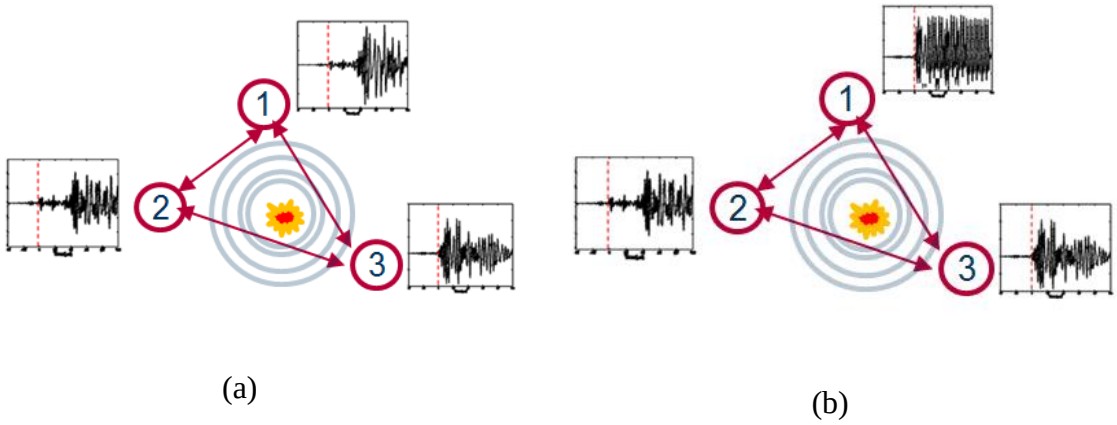

(a) (b)

Figure 4-2 The located events from (a) high EC values (b) low EC value.

A simple example to illustrate this method is given in two scenarios;

1) Signal from sensor 2 and sensor 3 are similar. The signals consist of sinusoidal wave $x = \sin(2\pi ft)$ with signal frequency $f = 10Hz$ and period of $T = 1$ second. Signal 3 has time delay of 0.5 seconds which can be represented by $y = \sin(2\pi ft - 1/2T)$. Signal 1 consists of Signal 2 but subjected to random noise. These signals are illustrated in Figure 4-3.

2) Similar to scenario 1 but Signal 1 is not subjected to random noise. Therefore signals from all sensors are similar although signal 3 is delayed.

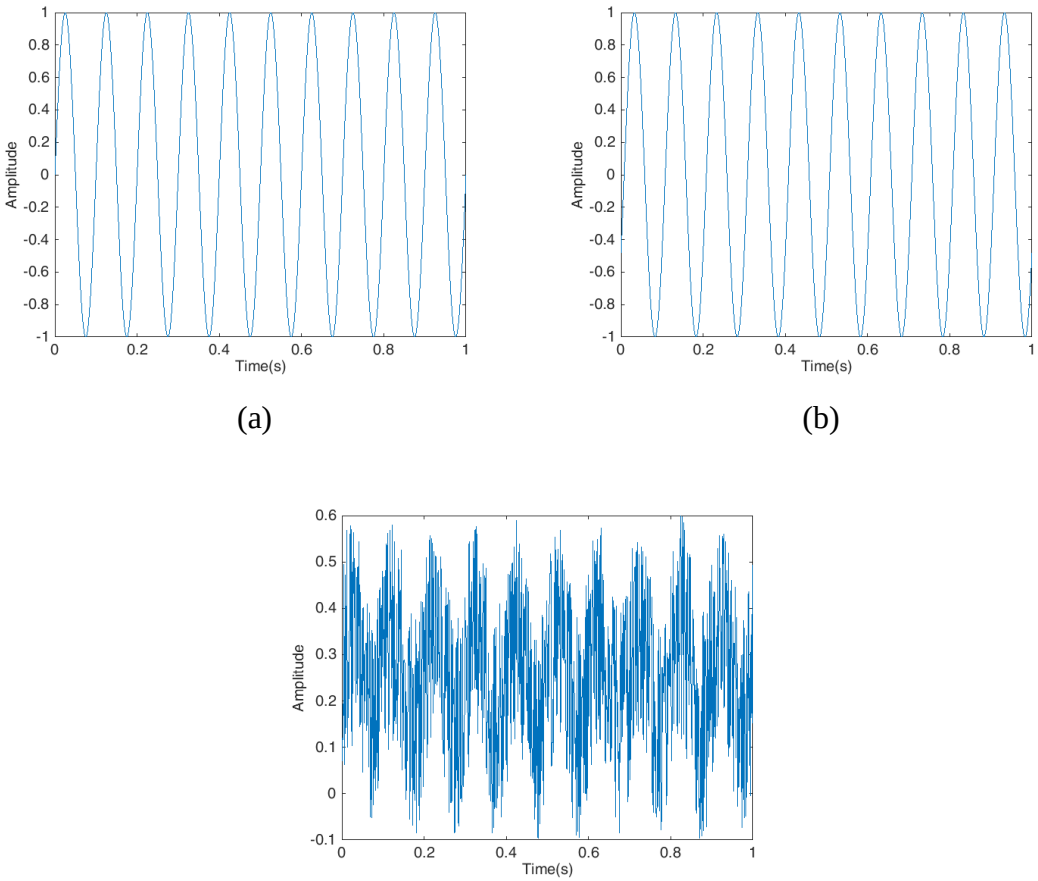

Figure 4-3 Scenario 1 (a) Signal 2 (b) Signal 3 (c) Signal 1.

Using eq. (4-2), the cross correlation is made for signal 1-2, 1-3 and 2-3 and EC were calculated. Table 4-1 and Table 4-2 summarize the calculated cross correlation coefficient and EC values for scenario 1 and scenario 2 respectively. As we have expected the EC values calculated in scenario 1 is comparatively smaller than scenario 2 due to the additional noise in Signal 1.

Signal combination	Cross Correlation coefficient, $\bar{\phi}_{i,j}$	EC
1-2	0.2844	0.0803
1-3	0.2822	0.0797

2-3	0.9987	0.2822

Table 4-1 – Cross correlation coefficient and EC values of various signal combination for scenario 1.

Signal combination	Cross Correlation coefficient, $\bar{\phi}_{i,j}$	EC
1-2	1	0.9987
1-3	1	0.9987
2-3	0.9987	0.9974

Table 4-2 - Cross correlation coefficient and EC values of various signal combination for scenario 2.

4.2.2 Analysis Procedures

In Bayesian estimation, the integration in the denominator of Eq. (4-1) i.e. "evidence" must be carried out over a high-dimension space and may not be tractable. This problem is usually solved using the Markov Chain Monte Carlo (MCMC) method [129,130], which enables the solution of integrals over high dimension probability distributions. The Monte-Carlo method approximates the integration of a continuous random variable, θ, by summation over a large number of discrete random variables $\theta^{(i)}\ i = 0,1,2,..,N$, which is independent and identically distributed $(i.i.d)$. The solution is computed by concentrating the samples $\theta^{(i)}$ in the regions of high probability. The stochastic process of Markov Chain Monte Carlo (MCMC) method [130], is referred to as a guided random walk which combines multiple samples sequentially. In the estimation of the *posterior* distribution, a chain of distributions of the random variables is constructed. The sequence of distributions tends to equilibrium, independent of the initial estimate. The convergent to *posterior* distributions i.e. $p(\theta|D)$ is termed the stationary distribution of the Markov chain such that $f\left(\theta^{(\tau+1)}\middle|\theta^{(\tau)},\dots,\theta^{(0)}\right) = f(\theta^{(\tau+1)}|\theta^{(t)})$. This means the parameter distribution $\theta^{(t+1)}$ at step $t+1$ depends only on $\theta^{(t)}$ and is independent of t.

4.2.2.1 Bayesian Model

The WinBUGS [131] (Bayesian Inference Using Gibbs Sampling [132]) program is used to generate samples from full conditional distributions of the posterior [133]. The likelihood estimation of the parameter is assumed to follow a Gaussian distribution given the random nature of the fatigue damage process. The likelihood is formulated as follows;

$$p(D|\theta) = p(D|\mu,\tau) = \sqrt{\frac{\tau}{2\pi}}\exp\left(-\frac{\tau}{2}\sum_{i=1}^{N}(EC_i-\mu)^2\right) \quad (4\text{-}4)$$

where;

μ is the mean of the distribution

τ is the precision or inverse of variance σ^2

The *prior* distribution for the samples' precision, τ_0, in this case is set to follow the Gamma distribution $\tau_0 \sim \Gamma(r,\mu)$; where r is the shape parameter and μ is the rate parameter. The parameters are unknown and hence $r,\mu = 0.001$. "Informative *prior*" is used for μ_0 based on the fitted distribution from the PLB tests. Therefore the posterior distribution is;

$$p(\mu|D) \propto p(D|\mu,\tau)p(\mu|\mu_0,\tau_0) \quad (4\text{-}5)$$

In this model the mean of the posterior distribution is indeed the most probable EC. The estimation was carried out with the signals obtained from the located events. The signals were extracted and cross correlated in MATLAB®. The EC values were calculated for each event and imported into WinBUGS for estimation. A schematic diagram of the process from acquiring data to estimating the EC values is illustrated in Figure 4-4. A graphical diagram of WinBUGS is illustrated in Figure 4-5. During the estimation process, there is non-stationary period known as a "burn-in" stage at the beginning of the iterations before the chain is converged. These values are discarded in the final estimation. The outcome in WinBUGS is illustrated by the density and history plot shown in Figure 4-6. In this example a flat or uniform *prior* is used.

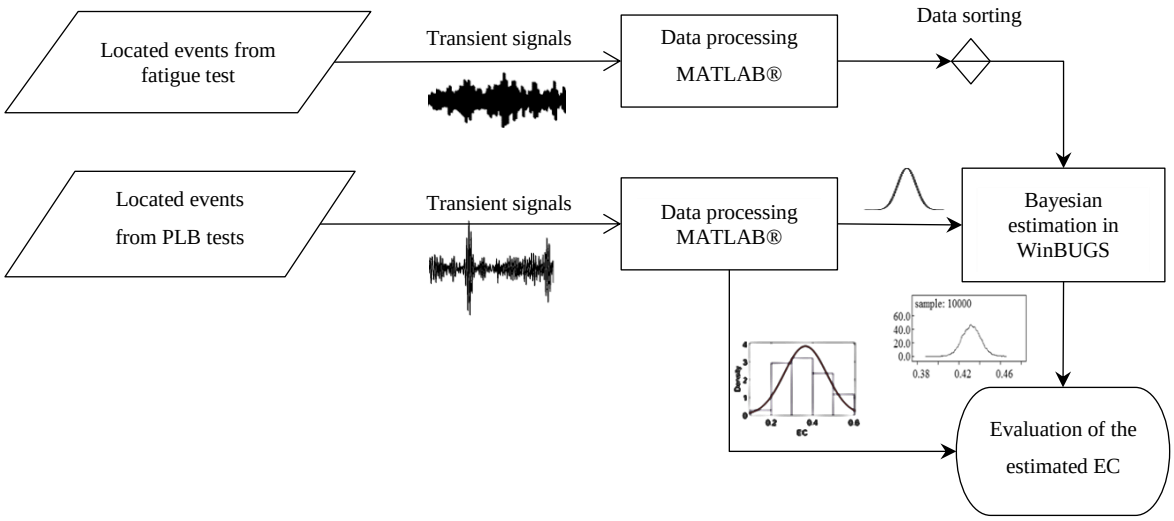

Figure 4-4 Estimation process flow chart

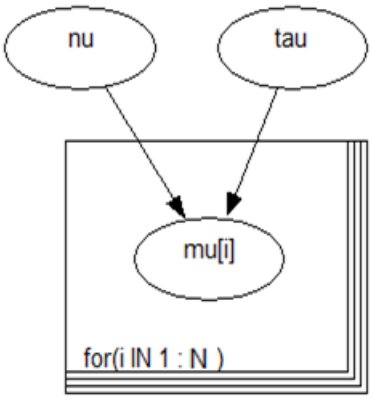


```
model;
{
  #Prior
  nu ~ dnorm( MeanPLB,PrecisionPLB)
  tau ~ dgamma(0.001,0.001)
  std<-1/sqrt(tau)
  #Estimate EC from nu
  for( i in 1 : N ) {
    mu [i] ~ dnorm(nu,tau)
  }
}
```

Figure 4-5 WinBUGS graphical diagram. The estimation is made for N data points.

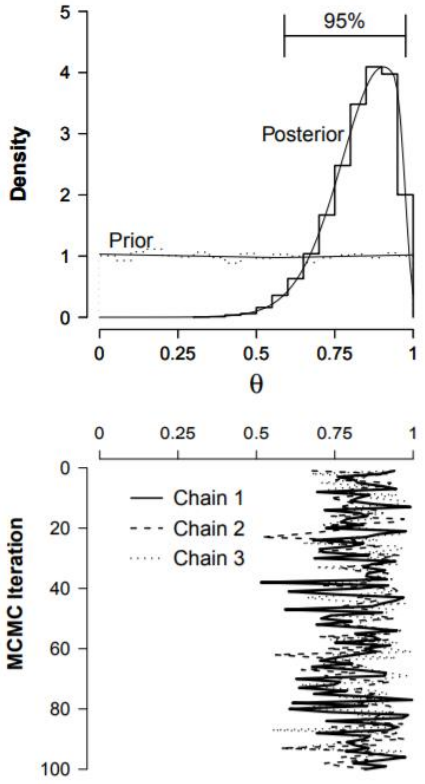

Figure 4-6 MCMC iterative calculation in WinBUGS. Density plot (top). History plot (bottom).

4.2.3 Experimental Setup

A 15 inch diameter carbon steel pipe with a 50mm wall thickness was installed and tested in a resonance fatigue testing machine [2]. The pipe was 7.2m long and contained a girth weld at mid-length. The pipe was filled with water, which has the effect of increasing the overall mass, and thus reducing the pipe length required for the same resonant frequency if it were empty. The pipe length was calculated based on its mass including the internal medium and both end attachments, to achieve a resonance in the first bending mode at around 30Hz. The resonance fatigue test rig comprises a drive unit at one end as shown in Figure 4-8-a. A 'balance' unit is present at the other end for dynamic symmetry. The drive unit contains an eccentric mass which is spun using a motor to provide a rotating radial force to the system. The driving frequency was adjusted to achieve a particular

strain range (as measured by strain gauges located at the mid-length of the pipe). A schematic diagram of the setup is shown in Figure 4-7.

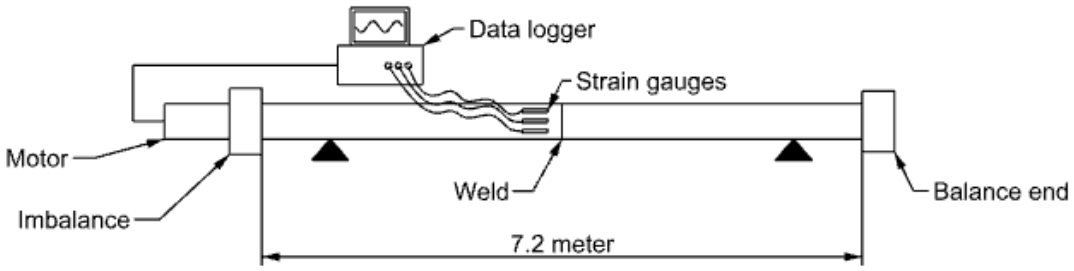

Figure 4-7 A schematic diagram of the resonance bending test setup.

The pipe mid-length, where the weld is located, is subject to the highest cyclic strain and hence the highest cyclic stress around the pipe circumference. The variation in stress from maximum to minimum is defined as a stress ratio of R=-1, and is superimposed on the axial stress generated by pressurising the water. The water pressure is chosen to produce an axial stress that is half of the applied stress range so that the resulting R ratio is greater than zero (R > 0). The pipe is supported at the nodes of the first vibration mode as illustrated in Figure 4-8-b where the displacement is minimal.

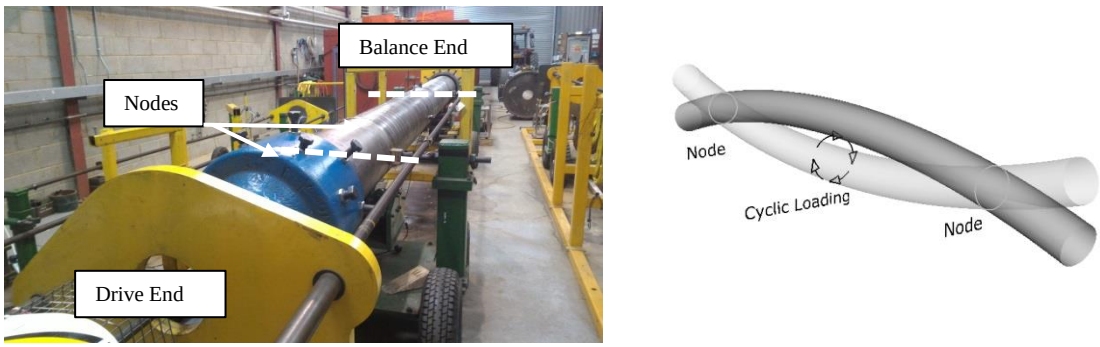

(a) (b)

Figure 4-8 The test set up. (a) Cyclic excitation is driven by a drive unit containing an eccentric mass at the drive end. There is a similar (static) mass at the other (balance) end for symmetry. (b) Two supports are positioned at the nodes where the pipe displacement is almost negligible.

Prior to the test, an ultrasonic testing was conducted around the weld to identify weld damage after welding process. Any defect identified shall be subsequently monitored.

4.2.4 Instrumentation Setup

Four broad band acoustic emission sensors (model VS900-RIC) with built in pre-amplifier from Vallen Systeme were used with a Vallen AMSY-6 multi-channel test system. The system was set to 5MHz sample rate with a band-pass filter between 95kHz and 850kHz. The duration discrimination time (DDT) and number of samples were set to 400μs and 2,097,152, respectively, to allow for sufficiently long recording of transient signals. Acoustic emission signals are highly contaminated by extraneous noise such as fretting at the pipe supports. Other sources of noise may be generated due to the mechanisms of fatigue cracking such as crack closure or crack face rubbing. Therefore, appropriate sensor positioning is crucial to avoid unwanted signals. In order to remove the effect of noise generated from the pipe supports and mechanical noise from both pipe ends, guard sensors (the noise will hit the guard sensor before hitting the data sensors) were placed at the 6 o'clock position at either side of the nodes close to the pipe supports. Elastic deformation creates additional noise by friction between the sensors and the pipe surface. To overcome these problems, two sensors were located at each node where the local displacement should be minimal, as illustrated in Figure 4-8-b. To reduce the uncertainties related to AE signal source locations, an asymmetric ring set-up was used allowing each sensor to record different arrival times than the case when all sensors would be located in the same plane. The sensors were attached using magnetic holders with grease between them and the pipe surface. The asymmetric sensor arrangement can make four combinations of isosceles triangular patterns i.e. 2-4-1, 4-1-3, 1-3-2 and 3-2-4 as illustrated in Figure 4-10. One aspect to consider using this triangular arrangement is that the circumcentre is not exactly coincident with the centre of the isosceles triangle hence need adjustment.

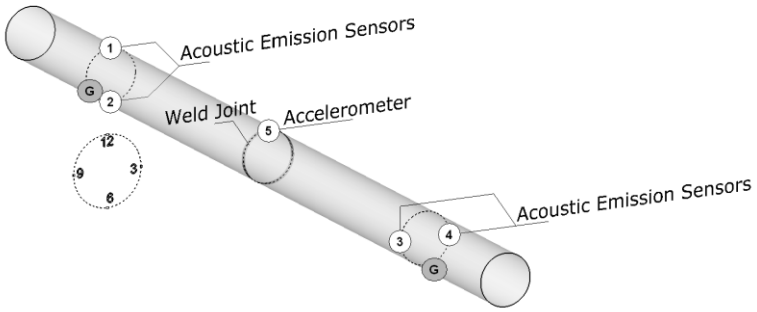

Figure 4-9 The location setup of acoustic emission sensors (numbered 1-4) at 12, 6, 9 and 3 o'clock positions respectively. A guard sensor (G) was mounted at 6 o'clock position close to each node and an accelerometer was mounted at 12 o'clock position in close proximity to the weld joint.

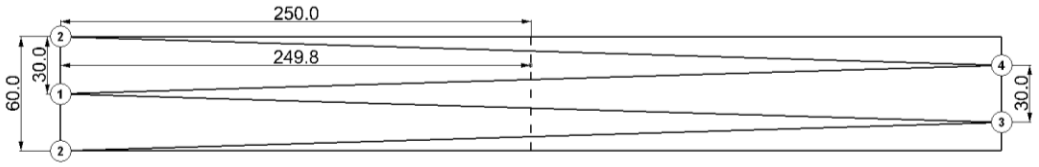

Figure 4-10 The combination of triangular patterns of sensor arrangement. Sensor 2 is labelled twice which marks a complete pipe revolution. The dimensions shown are in centimetres.

From the literature, it is understood that planar localization uses hyperbolic function to find the intersection point based on the arrival time difference. In order to use the method effectively, a maximum arrival time limit, Δt_{max} is introduced in the current research which limits the arrival time in the subsequent sensors upon detection by the trigger sensor. The trigger sensor is the first sensor that receives signal above threshold. Limiting the arrival time prevents detection of unwanted AE signals outside the assessment area, where defect may not be present. However, this method requires certain arrangement such that the defects are expected to be located in the circumcentre of the triangular sensor arrangement. The arrival time can be mathematically calculated from;

$$\Delta t_{max} = \frac{\sqrt{(x - x_d)^2 + (y - y_d)^2}}{V_g} \quad (4\text{-}6)$$

where x_d, y_d are the defect locations, V_g is the group velocity, and x, y are the extent of measurement area. This approach removes uncertainties of falsely detected AE signals due to reflection from geometric boundaries or noise generated outside the targeted areas, which has larger arrival time beyond the arrival time limit. The vibration measurement was evaluated by the input and output signals. The input i.e. excitation frequency from the motor was closely monitored and compared against the output vibration response measured by an industrial accelerometer mounted near the weld joint. The measurement output was fed into the Vallen system as parametric input with sampling rate of $500Hz$. The axial strain range was measured by eight equally spaced electrical resistance strain gauges mounted circumferentially. They were located 60mm from the weld toe as illustrated in the schematic diagram in Figure 4-7. The strain gauges were high resistance quarter–bridge strain gauges and high excitation voltage. The adhesion of the strain gauges to the pipe surface was carried out by experience technicians at Technology Welding Institute (TWI) according to manufacturer instruction. The measurement was sampled at $1kHz$ by National Instruments NI-9235 quarter bridge module configured in LabVIEW environment for data processing.

4.2.5 Calibration Measurement

The average group velocity, V_g was determined by pulsing between acoustic emission sensors (using one as a transmitter and the others as receivers). The propagating waves are identified by comparing the wave velocity against the DISPERSE code [90], a general purpose program for creating dispersion curves. A high threshold setting of 70dB was used based on the initial trials carried out prior to the actual test. The frequency of the arriving waves and their velocity were measured as approximately $180kHz$ and $3000ms^{-1}$ respectively, which is similar to the velocity calculated in the previous chapter. Although many wave modes appear at the measured frequency the calculated velocity is close to the transverse wave velocity (S-wave) in steel, which indicates Rayleigh waves in thick structures. Pencil lead break test (PLB) were performed at the 3,

6, 9 and 12 o'clock positions near the girth weld to examine the reliability of the proposed sensor arrangement. PLB is accepted as the standard method for calibration in acoustic emission testing [37,38]. Using the standard localization method provided by the Vallen Systeme, the events were located correctly as shown in Figure 4-11. It has been noted that using a single wave velocity can be erroneous due to the dispersion effect and mode conversion resulting from reflection at boundaries. Crack orientation could also influence the propagating waves [42]. In this work, the calculated velocity was assumed similar to that when cracks propagate through the thickness of the pipe.

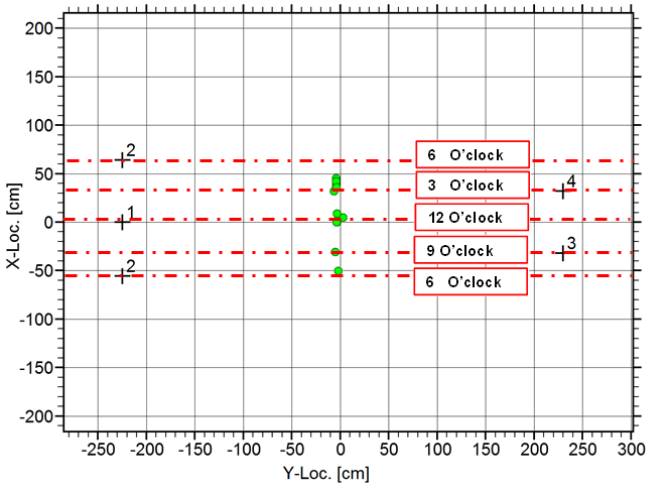

Figure 4-11 The Located events of PLB sources. Sensor 2 is labelled twice which marks a complete pipe revolution

4.3 RESULTS AND DISCUSSIONS

The resonance tests lasted in this experiment from start-up to failure for six days (corresponding to 14,106,360 applied cycles). The drive motor was stopped by a trip system immediately as the internal pressure in the pipe dropped rapidly when a through-wall crack was present. The failure location was identified at the 6 o'clock position where a 4mm long crack was present on the pipe outer wall. The crack had initiated on the inner surface and propagated through the pipe thickness. The parametric data were extracted and Short Time Fourier Transform (STFT) with low-pass filter was used. The vibration

frequencies were calculated to be 30Hz consistent over one hour durations at the beginning and end of the test. This shows that the excitation frequency of the pipe remained constant throughout the test, and is equal to the resonance frequency as depicted in Figure 4-12. The vibration amplitudes increase considerably towards the end of the test. Additional frequencies of approximately 50Hz emerged as soon as the drive motor was stopped allowing the pipe to come freely to a stop. From this observation, the additional frequency peak corresponds to different mode which may relate to damage. However, such frequency was not identified during the test. A snapshot of time series signal towards the end of the test, where the acceleration increased is shown in Figure 4-13.

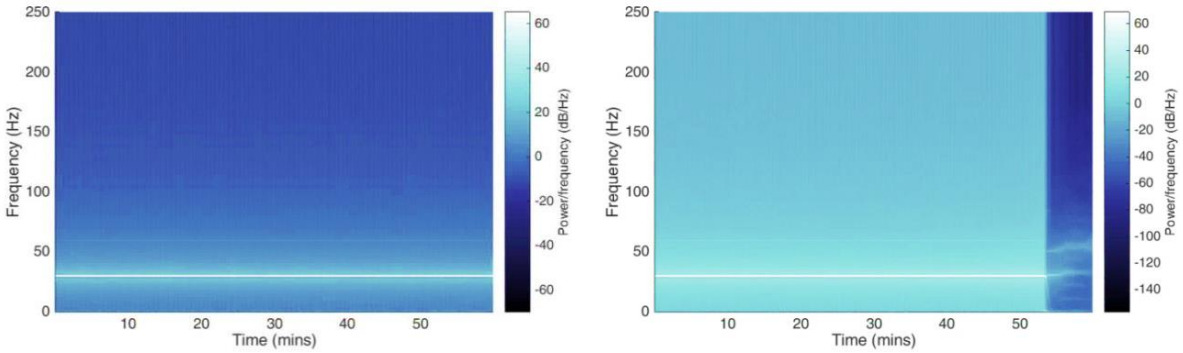

Figure 4-12 The frequency contents of the vibration signals coloured by power (dB)/frequency (Hz). (a) One hour duration at the beginning of the test. (b) One hour duration at the end of the test.

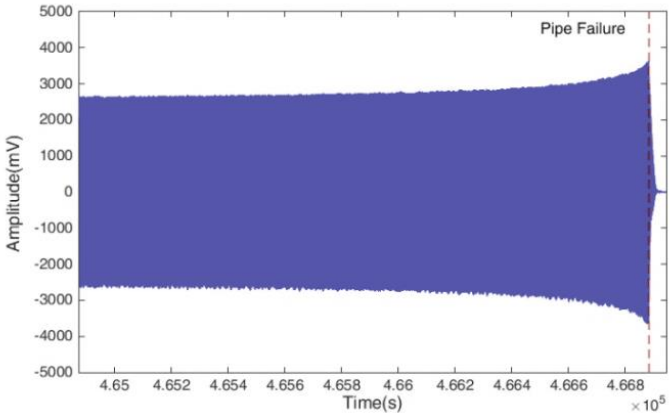

Figure 4-13 vibration signal recorded by the accelerometer.

4.3.1 Strain Range

Due to limitation of the system acquiring and storing the strain data, only average strain range for every thirty seconds was reported. The strain range recorded by each gauge varies almost consistently throughout the test as shown in Figure 4-14.

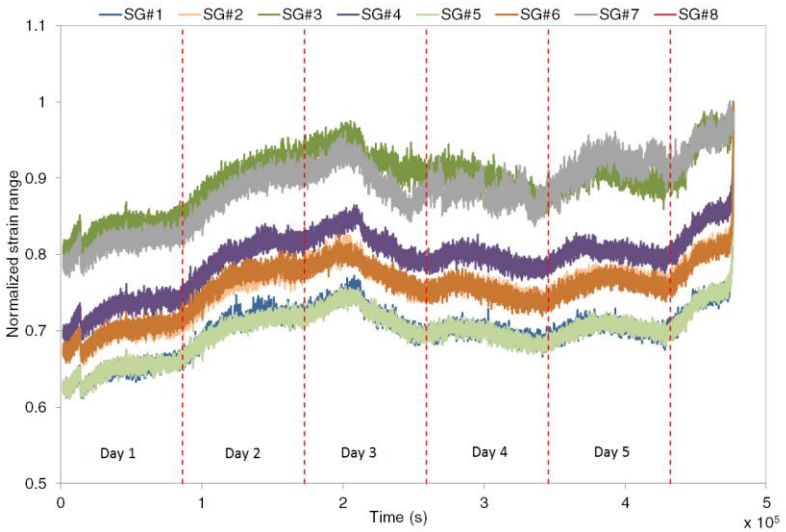

Figure 4-14 Strain range data recorded by the strain gauges located at the pipe mid-span approximately 60mm from the weld.

The strain from all gauges reached the first peak after day two before it started to drop in day three and four. The strain increased and decreased after day three before the pipe failed. Although the crack was identified at 6 o'clock, the origin of the crack may be initiated somewhere within the weld that is unable to be identified from the strain measurement. The pipe was mounted on the two supports, and hence the pipe weight may give additional stress by the act of gravity when the pipe bended towards the ground. This is however confirmed not to be the case as can be seen from the minimum and maximum strain ratio for SG#1/SG#5 i.e. the top and bottom strain gauges as depicted in Figure 4-15. The strain range recorded by the 12 o'clock strain gauge i.e. SG#1 is in fact increased throughout the test compared with the strain recorded at 6 o'clock i.e. SG#5 gauge. The minimum strain ratio decreased almost linearly.

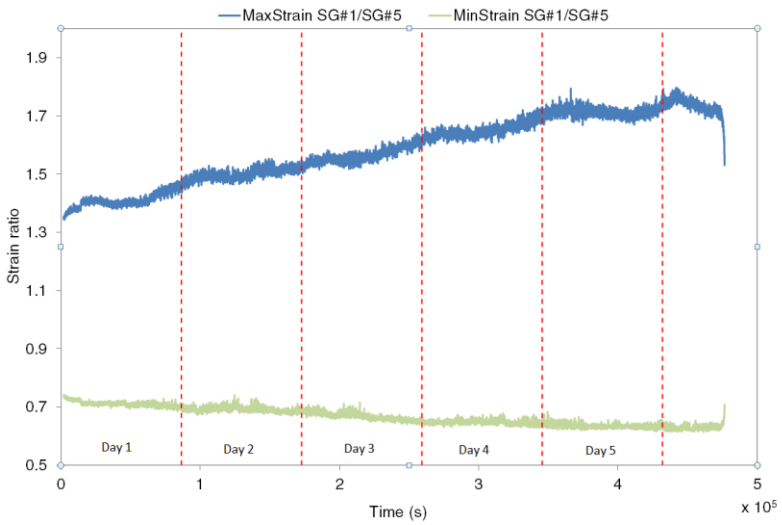

Figure 4-15 Strain ratio SG#1/SG#5 of the maximum and minimum strain.

Using the peak counting method, the number of cycle from strain data was calculated and recorded. At the beginning of the test, the strain frequency (i.e. maximum frequency for every 30s) is equivalent to the frequency of the excitation i.e. the resonance frequency of the pipe. The calculated frequencies before the strain reach the peak however is significantly higher with obvious erratic strain behaviour as illustrated in Figure 4-16. The frequencies calculated are approximately similar to the emerging frequency observed in spectrogram at the end of the test as shown in Figure 4-12-b. This implies the damage indeed introduce another strain mode in the system which was detected using the strain gauges.

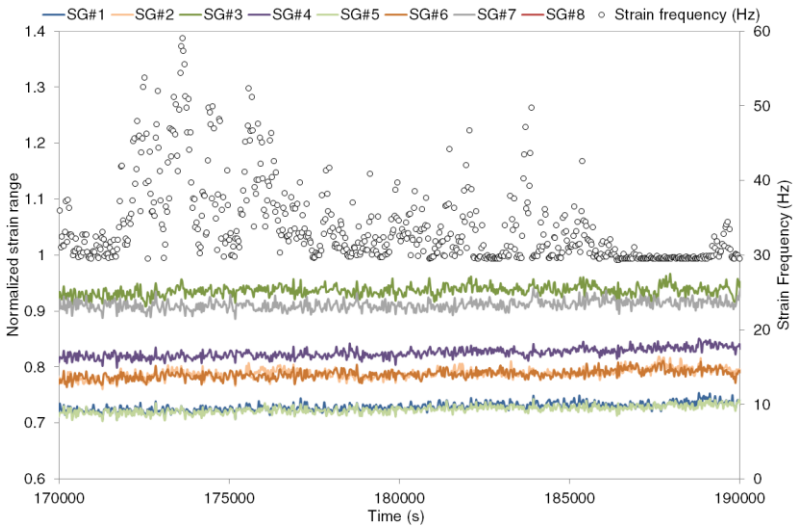

Figure 4-16 Strain ratio and strain frequency before the first peak after day 2.

In order to build a relationship between the strain and vibration data, the actual number of cycles recorded by the accelerometer, N_a, is divided by the number of cycles obtained using peak counting, N_s. This simple relationship has a maximum ratio of one when the number of cycles calculated is similar as illustrated in Figure 4-17. A comparison is made with acoustic emission at the numbered points i.e. 1-8. The ratio decreases starting in day two which implies damage is present. Similar pattern is observed at point 6 where the maximum reduction is observed. Before the pipe failed, the ratio decreased again at point 7 and 8. This information is crucial to be used for comparison with acoustic emission results.

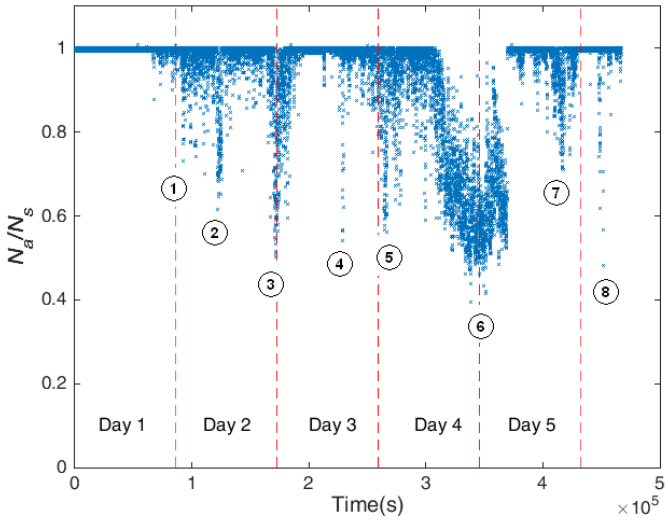

Figure 4-17 The ratio of actual number of cycles to the calculated cycles

4.3.2 Detection of Damage Evolution by AE

During the test, there were burst-like signals observed from the acoustic emission events. This signal is usually associated with cracks as illustrated in Figure 4-18-a. The burst signals consist of a number of wave trains due to reflection from boundaries as the waves propagate in the medium. Signals associated with noise such as continuous signals between burst signals were also recorded despite high threshold setting used as shown in Figure 4-18-b. These signals may correspond to plastic deformation [35,127] or crack face rubbing resulting from different crack modes and extraneous signals which are unknown. This causes problem in identifying true acoustic emission events for localization. However for detection purposes, the conventional parameter-based technique is sufficient to provide qualitative information.

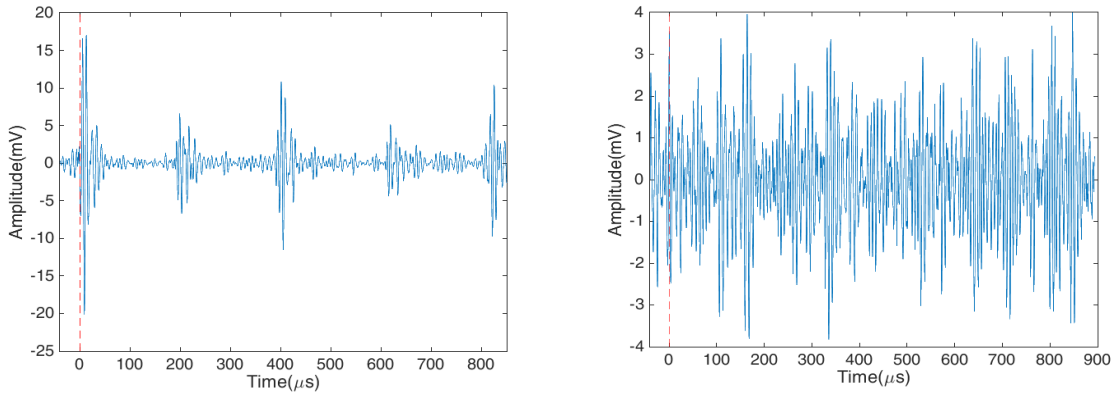

(a) (b)

Figure 4-18 Example of AE signals (a) due to cracking (b) and noise.

In order to make a comparison with the strain data, burst energy (i.e. the integral of squared signal amplitudes over its duration) was accumulated for every 30 seconds which is presented by dot marks in Figure 4-19. There are several peaks recorded from the energy. These peaks may correspond to the evolution of damage.

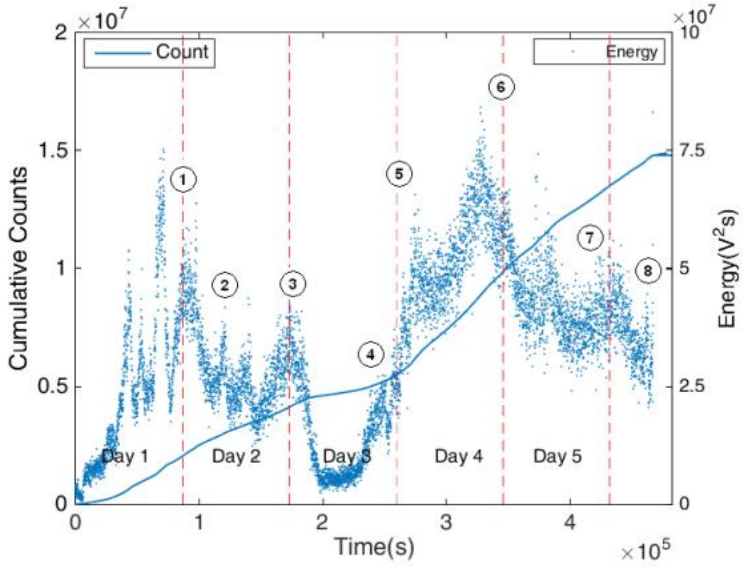

Figure 4-19 Acoustic emission features i.e. energy and count extracted from the AE signals.

There are a number of sharp rises and falls of AE energy observed in the early stage of test which is believed to be associated with micro-fracture phases [134]. Huang was suggesting three stages in fatigue damage [135]. The early stage or "stage one" corresponds to the first few cycles where the cyclic stress strain stabilizes. The strain in day one does not show any increase of frequency which implies that crack initiation had not been incurred. "Stage two" (i.e. crack incubation stage) correspond to steady dislocation of slip-bands which results in micro-cracks leading to macro-cracks. More large intervals of high amplitude of AE signals were expected. There are some spikes of AE energy denoted by point 2 and 3 in Figure 4-19, similarly for strain frequencies. This is an interesting observation which shows consistency in the results obtained using both techniques. At points 2 and 3, the AE energy accumulation may result from the emission of crack initiation, phase transformation or many other mechanisms provided in literature [47,127,135]. In this test specimen, it is most likely due to crack initiation. Similar trend is observed by the measured strain frequency. However, between points 3 and 4, the AE energy decreases suddenly to the minimum level which implies the noise threshold level in the system. Both techniques do not show any significant results which means "stage three" has not been started until day three. The process in "stage two" is expected to last longer as many microstructural activities in metallic material fatigue [136]. The scale of the geometry is relatively large to relate every microstructural activity which is not the main objective of this research. "Stage three", is the most active stage as various mechanisms occur at the same time including the microstructural activities. The cracks start to propagate with plastic deformation at crack tips, fracture along grain boundaries and many others [135]. This is reflected from the amount of data gathered within the last three days. The AE energy starts to increase tremendously between points 4 and 6 which recorded the highest peak. At these intervals the signals have longer duration which is associated with rapid releases of energy from crack activities. The longer duration and high amplitude signals result in the increase of AE count. A similar trend can be observed from the strain data where the number of measured cycles increases considerably at point 6 upon large crack growth. However the AE energy started to decay with smaller recorded peaks after point 6 and immediately before failure i.e. point 8. The reduction in energy means that fewer short duration signals are exceeding the threshold.

4.3.3 Localization of Damage

Although detection of damage can be identified using AE features, the located events can be misleading due to many signals obtained at the same time cracks propagated. The noise from reflection can lead to localization errors. Using planar localization technique, the events were located as illustrated in Figure 4-20. The events locations are distributed across the entire mid-section of the pipe circumference (i.e. along line at X=0) and span about 100 centimetre in each direction along the pipe length from the weld joint. This implies localization errors due large false events being recorded.

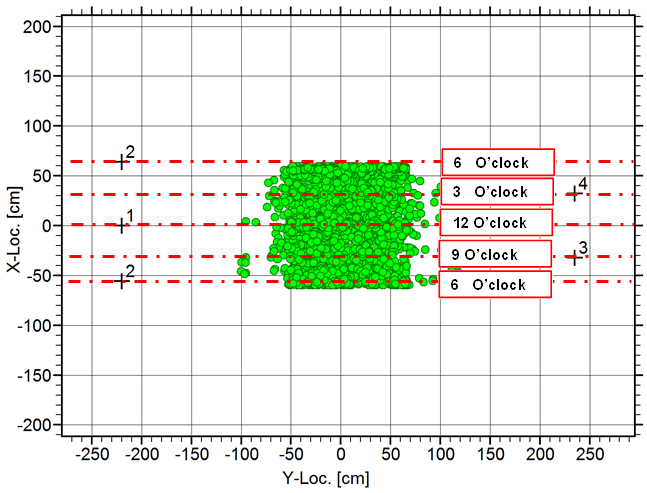

Figure 4-20 Located events on the pipe. Sensor 2 is labelled twice which marks a complete pipe revolution.

The asymmetric sensor arrangement makes four combinations of isosceles triangular patterns i.e. 2-4-1, 4-1-3, 1-3-2 and 3-2-4 as described earlier. The maximum time of arrival Δt_{max} can be limited in the acquisition system to only capture the events generated near the weld since the joint is mid-length between sensors 1, 2 and 3, 4. The area can be calculated using (4-6). In the previous chapter, the velocity of Rayleigh waves in the pipe was calculated approximately 3000 ms^{-1}. The (x_d, y_d) in this case is the circumcentre. By setting $\Delta t_{max} = 50\mu s$, the area of the circle is limited up to 15cm radius from the circumcentre which covers the entire circumference of the welded joint as illustrated in Figure 4-21.

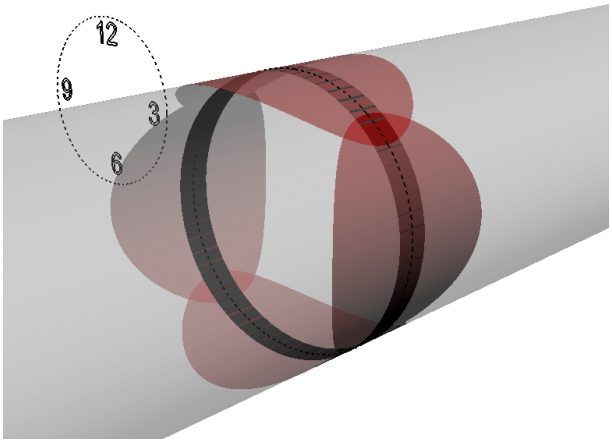

Figure 4-21 The covered area (red) around weld joint using the proposed triangular sensor arrangement with Δt_{max}

The crack growth concentrated locally particularly at 12 o'clock and 6 o'clock which suggests potential weak points. The high density of located events means failure at these locations is imminent. A number of located events were also recorded around the weld joint apart from the location of failure at 6 o'clock position. The damage was expected to propagate around the weld since the stress generated around the pipe circumference was almost consistent. The located events (marked in blue) as shown in Figure 4-22 were repeatedly recorded before the crack finally emerged on the pipe.

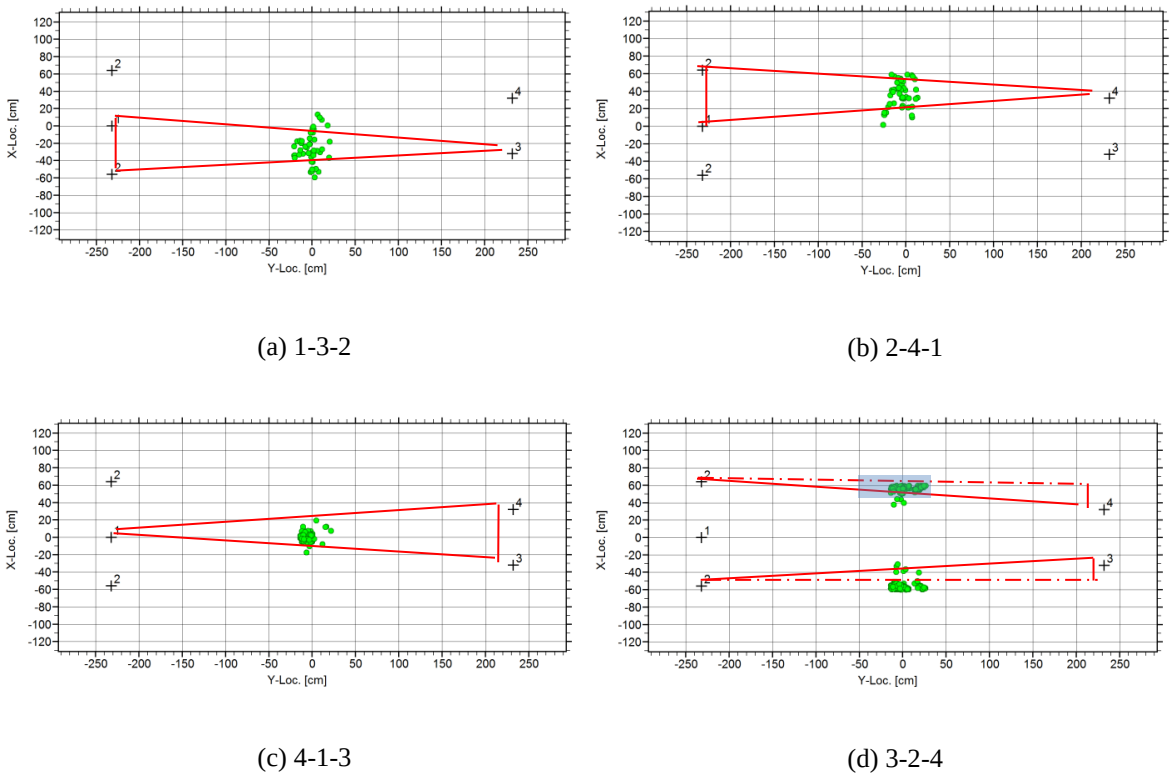

(a) 1-3-2

(b) 2-4-1

(c) 4-1-3

(d) 3-2-4

Figure 4-22 The located events when the pipe failed. Sensor 2 is labelled twice which marks a complete pipe revolution.

4.3.4 Bayesian Estimation

Numerous events were recorded during the last three days of the test when crack propagation was active. Only these events were post-processed to demonstrate the practicality of using Bayesian estimation. Figure 4-23 shows AE burst energy where high activity of AE was observed towards the end of day four. However the energy is relatively low before the pipe failed which demands further investigation. (Note the difference between the cumulative energy calculated for every 30s in Figure 4-19 and discrete energy in Figure 4-23).

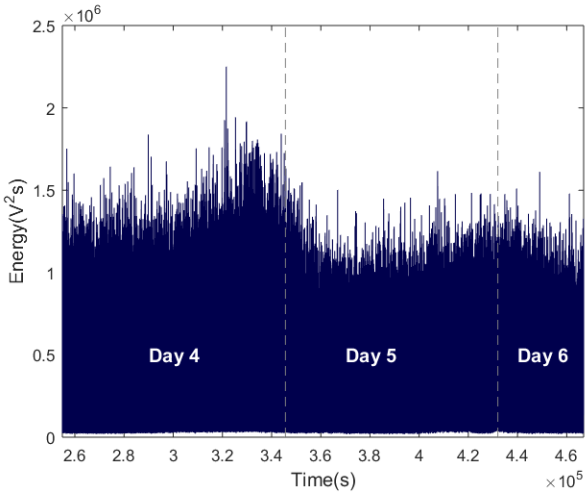

Figure 4-23 Discrete acoustic emission energy recorded during the last three days of the fatigue test.

The acoustic emission signals that registered the events were not only typical burst signals normally observed from crack-related activities as described in the preceding section. There existed some continuous random signals having long signal duration. Figure 4-24-a shows an example of signals recorded by sensor 1-3. The signals are random in nature, despite some signal peaks observed. Although the signals from sensor 3 may have some burst-like signals, the event was actually generated from combination of less correlated signals which was verified by analysing the cross-correlogram plot illustrated in Figure 4-24-b. In contrast, the events generated by different signal combinations give better correlation (shown in Figure 4-25-b); such signals are predominantly generated from cracks. Therefore, based on this idea, Bayesian estimation was used to estimate credible parameters identified according to this relationship, and to compare with the acoustic emission energy.

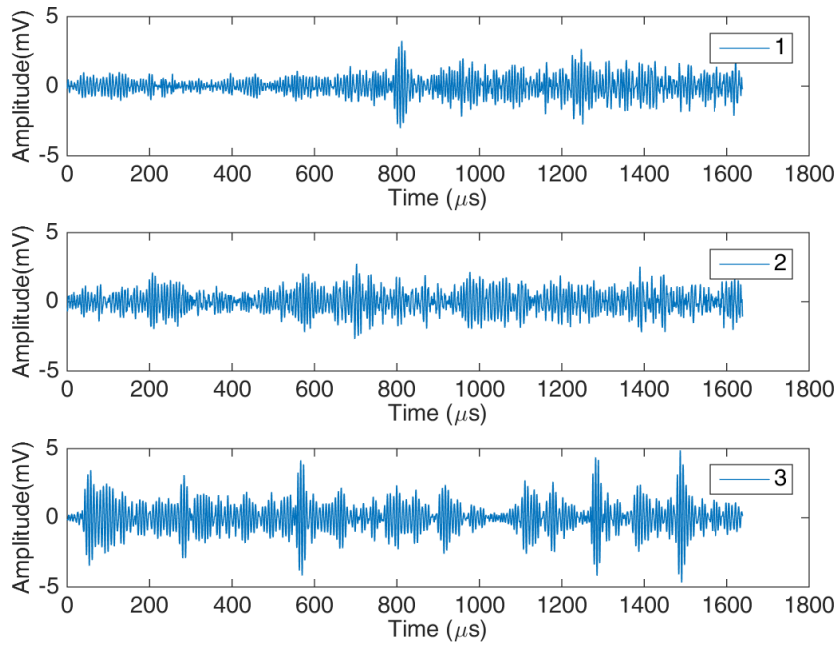

(a)

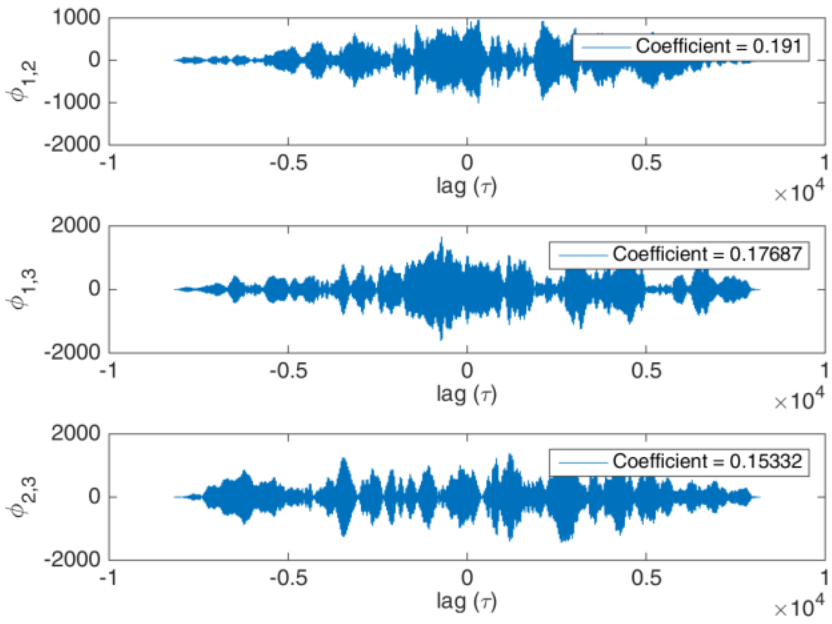

(b)

Figure 4-24 (a) Typical random signals recorded at sensor 1 – 3. (b) Low correlations of random signals were calculated for different combination of signals.

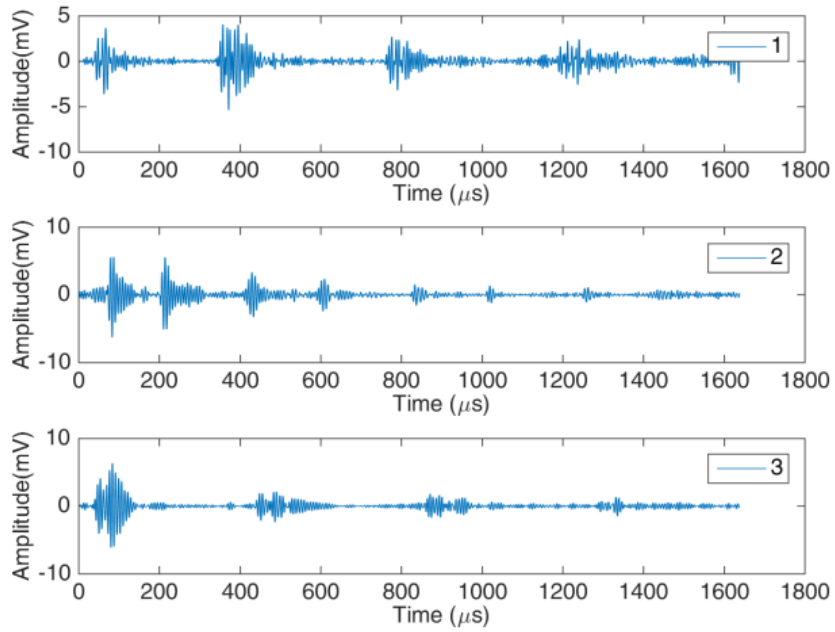

(a)

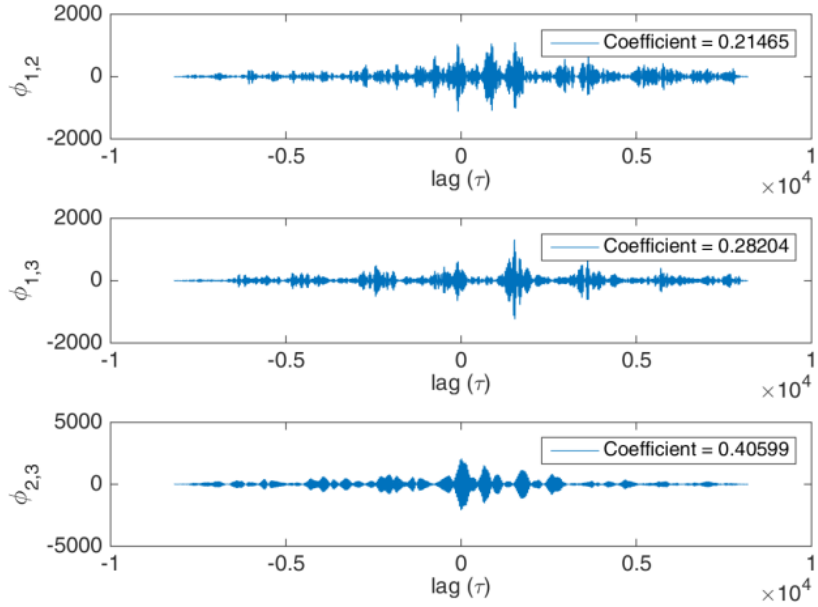

(b)

Figure 4-25 (a) Typical burst like signals recorded at sensor 1 – 3. (b) High correlations of burst-like signals were calculated for different combination of signals.

In order to compare the variation of signals after Δt_{max} is applied, 20 intervals of equal duration were defined from the test duration as illustrated Figure 4-26. There is no rule on the selection of number of intervals. For this assessment the selected number of intervals is considered sufficient if a clear distinction of successive events and those gaps are observed in some intervals. Increasing AE energy can be seen towards the end of the test which implies cracks were actively propagating compared to those events before Δt_{max} was applied.

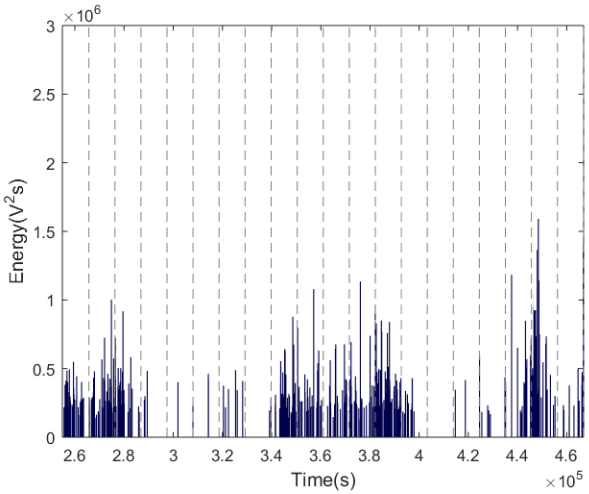

Figure 4-26 The acoustic energy obtained from the signals of the located events when Δt_{max} is used

To establish the *prior* distributions, correlation was made for a range of signal durations and EC values were calculated. The distributions of EC values from a set of pencil lead break (PLB) are shown in a whisker plot (Figure 4-27-b). A larger signal duration results in reduction of the mean values and variances.

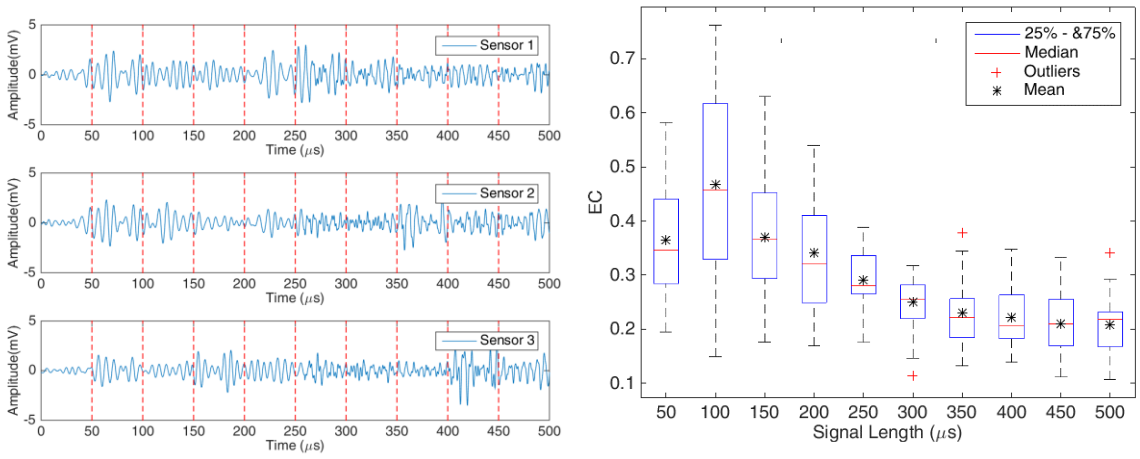

(a) (b)

Figure 4-27 (a) Various signal durations specified across the entire signal duration. (b) Whisker plot of the calculated EC.

As can be seen from Figure 4-27-a, a larger signal duration accommodates larger signal variations. Each signal duration provides important information for Bayesian estimation, thus these distributions are assumed to provide an important reference for crack damage. Therefore the *prior* distributions can be established from this information. The *prior* derived from PLB tests are distributed normally based on the distributions of EC of each signal duration. A summary of these values is tabulated in Table 4-3.

Signal length (μs)	$\overline{EC}$	σ^2	$\tau = \frac{1}{\sigma^2}$
50	0.376	0.01075	93.05
100	0.502	0.02238	44.68
150	0.359	0.01239	80.71
200	0.323	0.01087	92.03
250	0.290	0.00291	343.25
300	0.251	0.00210	477.09
350	0.224	0.00314	318.28
400	0.217	0.00303	330.14
450	0.205	0.00312	320.88
500	0.204	0.00274	364.90

Table 4-3 - The *prior* distributions

The 100μs signal duration has the largest spread of EC values. The arrival signals from each sensor are very similar as shown in Figure 4-27-a. However, the signals below 50μs are small magnitudes within the pre-trigger duration and hence are not considered appropriate to be used as *prior*. Likewise, the means of the distributions above 300μs converge to a single mean value as shown in Figure 4-27-b. Therefore the estimation was made for a signal duration from 100μs to 300μs. The Bayesian estimation was carried out for the signals obtained from the located events. Figure 4-28 shows a history plot of the estimated mean EC denoted by $\overline{EC}$ and standard deviation respectively in WinBUGS for signal length of 300μs. The density plots for both parameters are given in Figure 4-29.

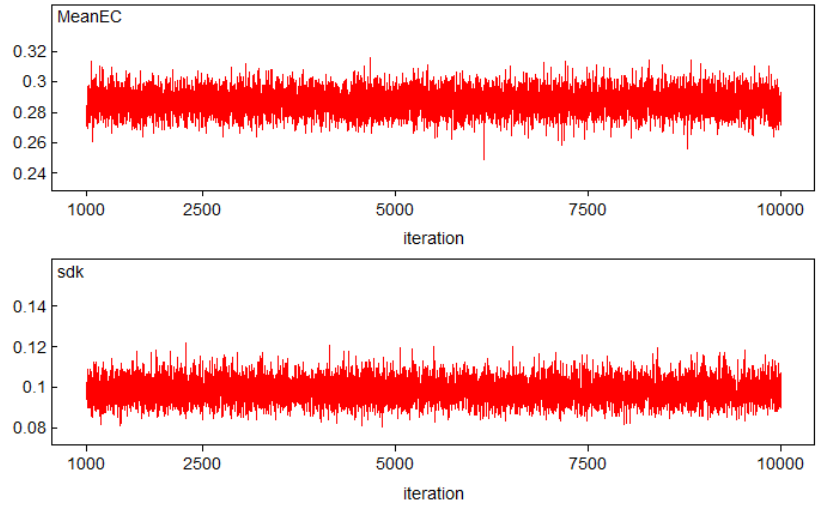

Figure 4-28- History plots of the estimated mean $\overline{EC}$ (top) and standard deviation (bottom).

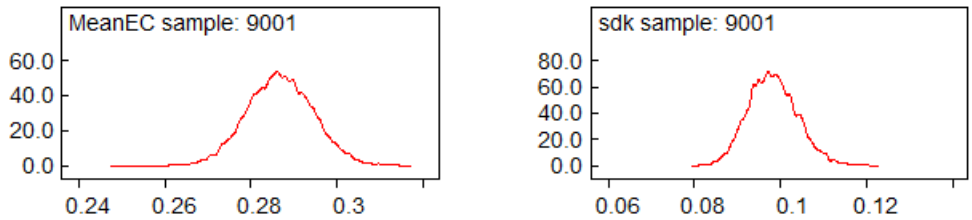

Figure 4-29 – Density plots of mean $\overline{EC}$ (left) and standard deviation (right).

The 95% credible intervals of the estimated means from the *posterior* distributions are plotted with the AE burst energy in Figure 4-30.

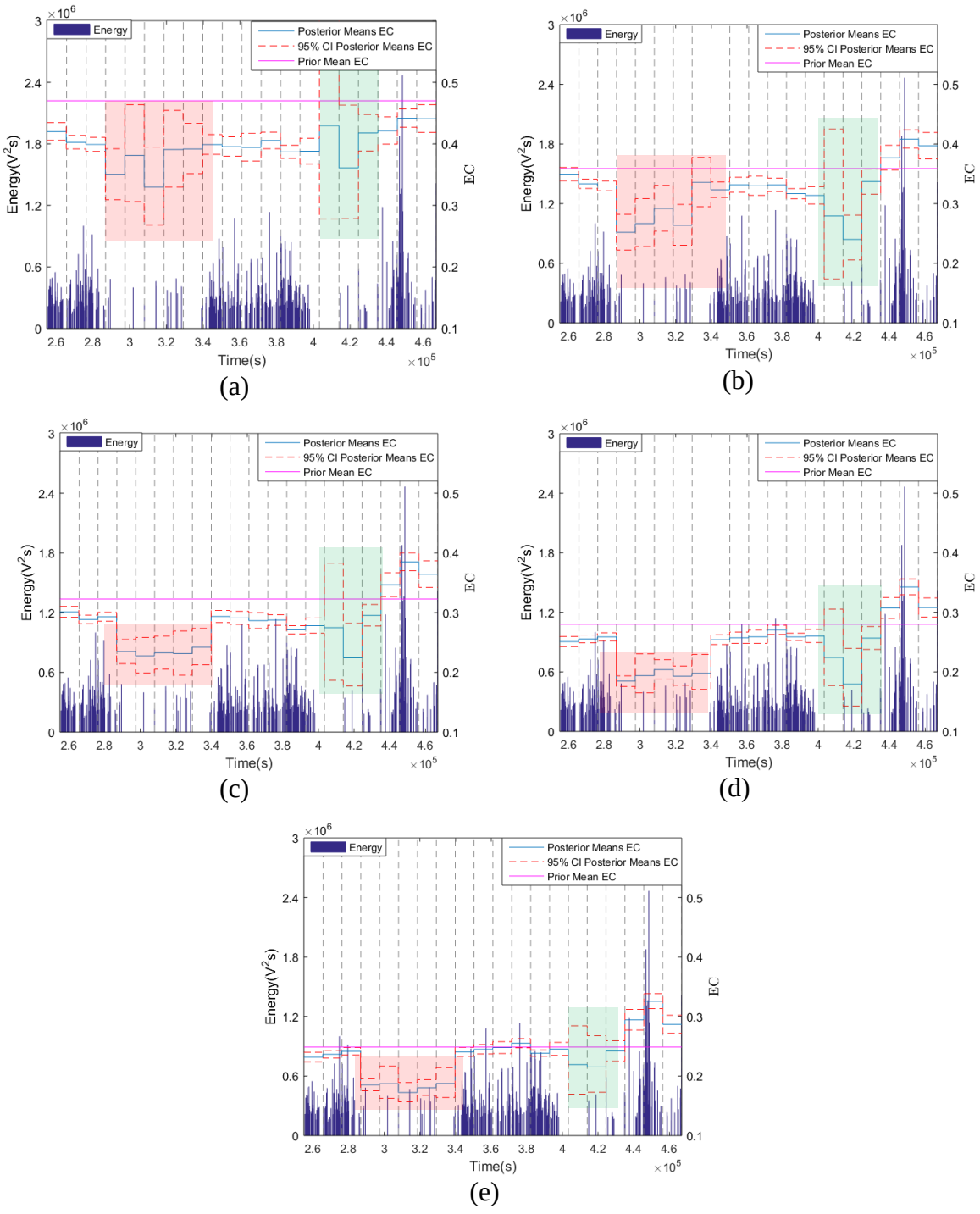

Figure 4-30 The estimated $\overline{EC}$ with 95% credible intervals and the *prior* mean values from the PLB tests for various signal durations (a) 100μs (b) 150μs (c) 200μs (d) 250μs (e) 300μs.

The estimated ECs are plotted with the AE burst energy for comparisons. The highlighted red and green areas are the intervals where the majority of located events are away from the weld area. Interesting observations can be seen from the estimated EC for various signal durations. The estimation for 100μs signal duration has a large EC variance particularly in the highlighted intervals, which is largely contributed by the variance from the prior distribution. Almost all of the estimated means are below the reference mean derived from the PLB tests. The reason is believed to be due to the fact that signals generated by PLB are not perfectly similar to the actual crack signal. The distinction of the waves generated by the PLB on the pipe surface with respect to the actual cracks originally initiated within the weld is also noted. The similarity is more pronounced before the pipe failure since the sources are mainly near the surface. In these intervals the estimated EC for all signal lengths is higher compared to the preceding intervals. For larger signal durations, the estimated EC is lower for all intervals; the means of the highlighted (red) intervals in Figure 4-30 are consistently below the reference means, apart from the highlighted (green) intervals where uncertainties remain due to the large estimation of variance. The AE energy is mostly empty for these intervals, which implies that the low EC values are mainly events generated outside the weld area. The uncertainties of the located events can be justified by studying the 95% confidence level of the estimated means; for the estimated EC within the same intervals as when the AE energy was recorded using the filtering method (i.e. maximum time of arrival Δt_{max}) most of them are very close to the reference means which implies the located events are indeed related to damage.

4.4 CONCLUDING REMARKS

In this chapter acoustic emission and vibration monitoring of resonant fatigue pipe was carried out. The objective was to evaluate whether AE can be considered as an effective method for continuous monitoring of vibration-induced fatigue pipe. In theory the natural frequency of the pipe is expected to reduce when cracks propagate due to reduction in structural stiffness. However there was no reduction observed by carrying out the frequency analysis. The frequency associated with the damage could only be seen as soon

as the excitation was removed from the system after the pipe failed. The emerged frequencies were almost similar with the strain frequencies. These frequencies are believed to be associated with the change in strain modes during damage. A relationship was established using the actual number of cycle and the calculated cycles from strain measurement to represent the damage sensitive feature. The ratio decreased when the strain frequencies increased. The trend shows good agreement with the acoustic emission energy distribution. In summary, strain measurement and AE has proven effective for detection of damage. However errors in source localization by AE are significant due to many false events recorded. The uncertainties associated with the measurement output were observed. In order to evaluate the uncertainties, a Bayesian estimation procedure based on Bayesian theorem was proposed. This method evaluates the most probable effective coefficient (EC) derivable from the cross correlation of signals. EC measures a minimum degree of similarity of the correlated signals taking into account the maximum and minimum coefficients from each signal combination. In this model the mean of the *posterior* distribution is indeed the most probable EC. Twenty intervals of equal length were defined from the test duration for EC estimation and comparison with the AE energy. The *prior* distributions for Bayesian estimation were defined using the results of artificial signals of cracks generated by pencil lead break method (PLB). The *prior* distributions provide a range of $\overline{EC}$ for estimation as well as the reference means (i.e. expectation) for comparison. The estimation was carried out for various signal lengths. The estimated *posterior* $\overline{EC}$ were taken within 95% credible intervals. For larger signal lengths, the estimated *posterior* $\overline{EC}$ are very close to the reference means which implies the AE signals from the generated events are most likely from cracks. The maximum time of arrival Δt_{max} was limited in the acquisition system to limit the events generated near the weld. Using this method, the energy of the signals from the filtered located events were obtained and compared. Both the energy and the *posterior* $\overline{EC}$ are in very close agreement. The energy associated with cracks damage has higher EC values. This observation provides strong evidence that this procedure can be considered as a robust method to quantify the uncertainties of the located events.

CHAPTER 5

ACOUSTIC EMISSION MONITORING OF RESONANCE FATIGUE TEST OF ALUMINIUM PLATES

5.1 BACKGROUND

The motivation of this chapter is to develop a damage sensitive feature for damage identification using AE to be used in SHM. Compared to the techniques used in Chapter 4, damage caused by vibration could be identified using Lamb waves avoiding the localization errors by using systematic experimental setups. This allows the study of severity of damage during the fatigue process comparing the variation of natural frequencies with respect to the undamaged state. In this chapter, acoustic emission monitoring of resonance fatigue tests of 6082-T6 aluminium plates was carried out. The plate was excited at the fundamental frequency of bending mode using an electrodynamic shaker exciting the structure at the maximum stress the mid-span location. A sharp notch was created to accelerate mode I crack propagation. The objective was to characterize damage using fundamental wave modes. A parameter was derived which relate the severity of damage using amplitude difference of the S_0 and A_0 wave modes using correlation of experimental data with Finite Element analysis . The motivation of this chapter is to develop a damage sensitive feature for damage identification using acoustic emission technique that can be used in structural health monitoring.

5.2 EXPERIMENTAL AND ANALYSIS PROCEDURES

The experiment was carefully designed to allow fatigue crack propagation. The following experimental steps were carried out:

1) Determination of the allowable vibration acceleration for the plate to undergo fatigue without immediately fracture of the test specimen upon test start-up
2) Minimization of the extraneous noise generated from the supports to avoid errors in wave modes identification
3) Development of a damage sensitive merit figure using Lamb waves and its validation by using numerical simulations

5.2.1 Experimental Setup

The plates were mounted onto a fixed support at each end as illustrated in Figure 5-1-a. $11mm$ diameter holes were drilled both on the supports and plates (i.e. $2cm$ from plate ends). The fixtures were rigidly mounted on a table shaker to allow only vertical movement being designed such that their natural frequencies are higher and well separated to the fundamental frequency of the plate. A schematic drawing of the fixtures is given in Figure 5-2. A flat rubber was sandwiched between the plates and the supports to remove noise generated due to direct contact with the plates during vibration. The $10mm$ dimeter bolts were covered with rubber sleeves to damp the noise generated at the joints as illustrated in Figure 5-1-b.

(a) (b)

Figure 5-1 (a) A 6082-T6 aluminium plate fixed at both ends. (b) A $10mm$ diameter bolt is covered with rubber mount and sleeves to avoid noise generated at the supports.

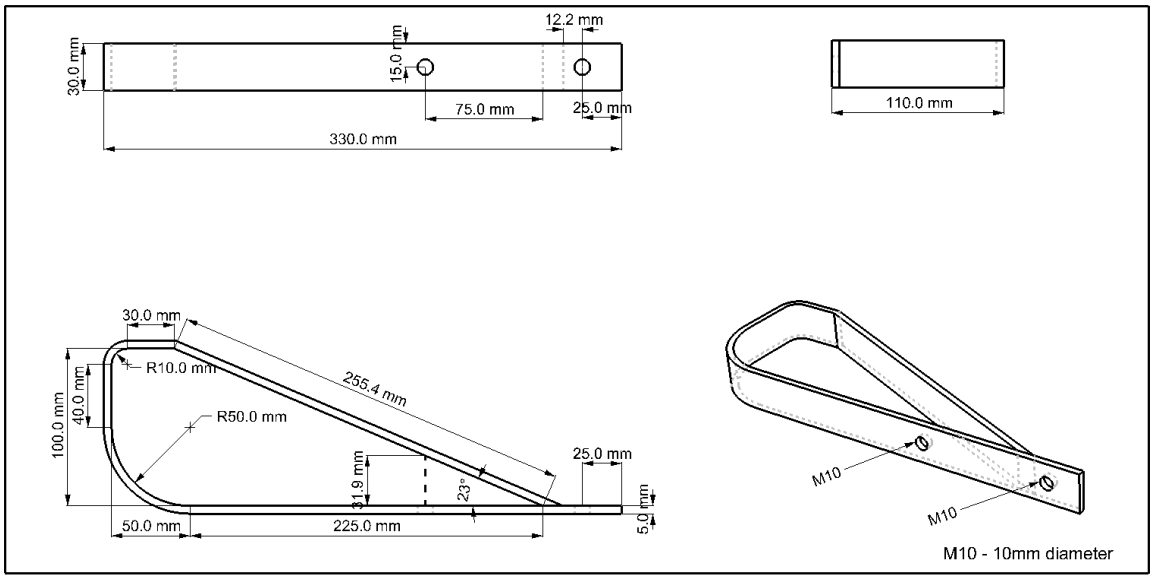

Figure 5-2 Schematic drawing of the fixture.

The natural frequencies of the plates were determined from the measured Frequency Response Function (FRF) [137], using the output/input signals. In this case the output is the response signals subjected to the input signals created using an impact hammer exciting the structure at the plate mid-span. A tri-axial accelerometer was mounted on the opposite side of the plate to capture both resonance and anti-resonance frequencies. An impact hammer (model 086C03) and a PCB PIEZOTRONICS accelerometer (model 356A16) were used in the test setup shown in Figure 5-3-a and Figure 5-3-b and a Bruel and Kaer (B&K) system was used to record vibration signals. The determined FRF is shown in Figure 5-3-c.

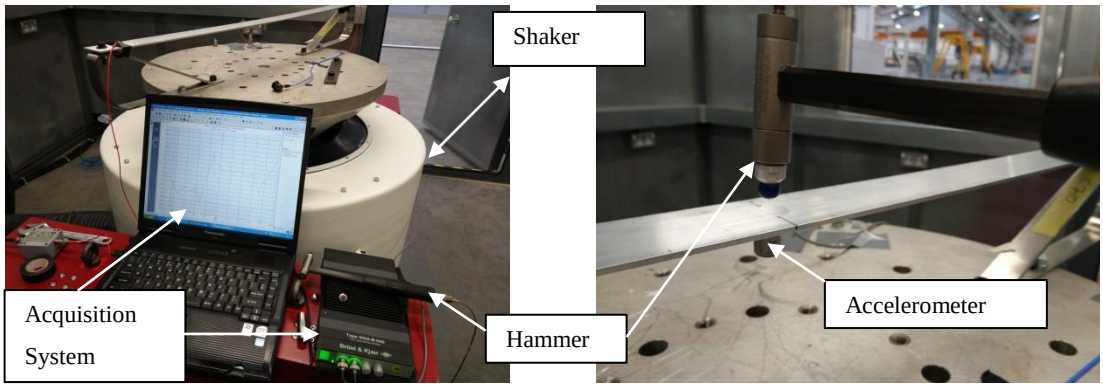

(a) (b)

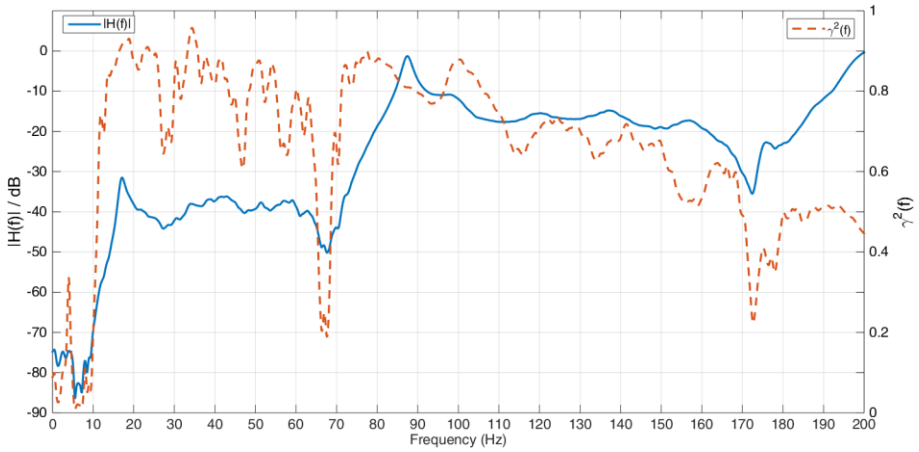

(c)

Figure 5-3 (a) B&K data acquisition system. (b) Impact hammer and accelerometer (c) FRF and coherence of the output/input signals.

The fundamental frequency was measured at $17.125Hz$ as can be seen from the first peak of the FRF $|H(f)|$ curve in Figure 5-1-c. A number of resonances (harmonics) and anti-resonance were recorded at $87.62Hz, 67.62Hz$ and $172.5Hz$ respectively. The fundamental frequency can be calculated analytically using the classical Euler Bernoulli beam theory for both ends clamped as follows [138], [139];

$$\omega_1 = 22.4\sqrt{\frac{EI}{ml^4}} \tag{5-1}$$

where;

ω_1 is the cyclic frequency

I is the second moment of area, $I = bt^3/12$, b is the plate width, t is the plate thickness

m is the mass of the plate

E is the elastic modulus

l is the length between support

From this calculation, the elastic modulus of the plate can be verified. The mass of the accelerometer is included in the calculation as a lump mass (i.e. plate mass, 0.385kg plus accelerometer mass, 0.0074kg). The length between support is $l = 0.965m$ which leads to a determined value $E \cong 70GPa$ similar to the standard material property of 6082-T6 provided in Table 3-1. This verification is important to ensure that the elastic modulus used in FEA is correct.

5.2.2 Finite Element Model

In this section the following aspects are discussed:

1. Estimation of stress and acceleration required for crack propagation
2. Simulation of wave propagation generated using an artificial crack source (i.e. monopole source) on the plate surface for wave modes identification analysis The model was verified experimentally using PLB sources.
3. Simulation of wave propagation generated from crack extension (i.e. through thickness) using a similar model as shown in in 2), to study the effect of crack depth to the fundamental wave modes

5.2.2.1 Stress estimation

The finite element model was created such that the holes were fixed (i.e. bolted) and a point mass was included to account for the mass of an accelerometer. Figure 5-4 shows the boundary condition setup. The structure model was carefully modelled according to

the actual boundary conditions and the analysis was carried out using ANSYS (version 15) Using shell elements (SHELL181) appropriate for the analysis of thin to moderately-thick shell structures.

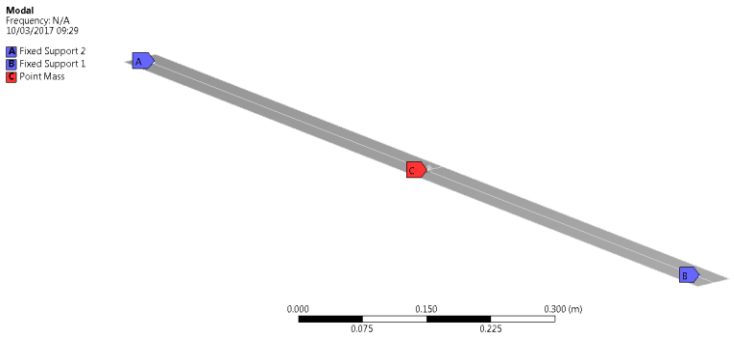

Figure 5-4 Vibration analysis setup.

The deformation of the plate (undamped) in the first bending mode is illustrated in Figure 5-5. The plate mid-span presents minimum and maximum acceleration, respectively stress state. The simulated resonance frequency was slightly higher than the measured value. To improve the correlation with the experimental data, an additional mass was added to account for the mass of wire, glue etc. to achieve similar resonance frequency. The elastic modulus was not changed in this case to avoid errors in the stress calculation. A further model refinement was done by adding damping.

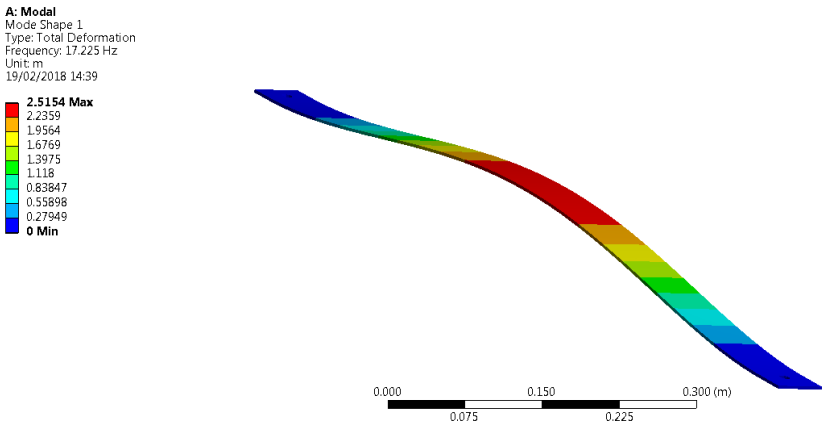

Figure 5-5 Bending mode fundamental frequency at $17.23 Hz$.

The damping associated with the fundamental mode (i.e. bending mode) was calculated from the FRF using half-power bandwidth method [137,140] as given in the following equation:

$$\zeta = \frac{f_b - f_a}{2f_n} \tag{5-2}$$

Where ζ is the critical damping coefficient, f_b and f_a are the forcing frequencies deduced from -3dB from peak amplitude as shown in Figure 5-6. Therefore,

$$\zeta = \frac{f_b - f_a}{2f_n} = \frac{18.15 - 16.4}{2(17.125)}$$

$$\zeta = \frac{f_b - f_a}{2f_n} = 0.05 \tag{5-3}$$

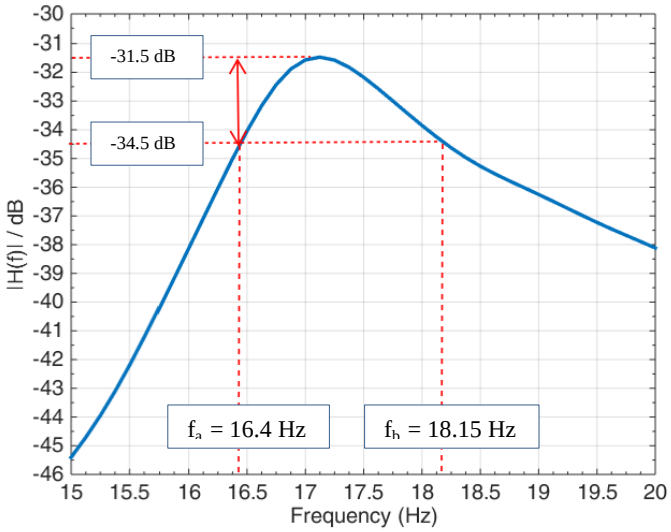

Figure 5-6 3dB Half power method.

The structural model was excited in a similar manner to allow the response comparisons. The estimated principal stresses according to different base acceleration cases are given in Table 5-1.

Base acceleration (g)	Maximum Plate acceleration (g)	Simulated stress (MPa)
0.3	5.06	3.96
0.5	11.63	9.28
0.7	16.95	13.45

Table 5-1 – The simulated stress according to different base acceleration.

5.2.2.2 Noise estimation

A set of vibration tests with various base accelerations were carried out with AE sensors mounted $5cm$ from each plate end including an additional accelerometer mounted on the plate mid-span. The additional accelerometer was used to record continuous acceleration data for comparison with AE measurement. The objective of the test is to estimate the noise level measured by AE. Three base excitation levels were tested at. 0.3g, 0.5g and 0.7g. A slight reduction of natural frequency was noted due to the additional mass of accelerometers and AE sensors. The base was sine-swept with constant acceleration from 10Hz to 20Hz. Figure 5-7 shows the plate response for the three cases and one can note the that the acceleration of the response increases with the excitation level.

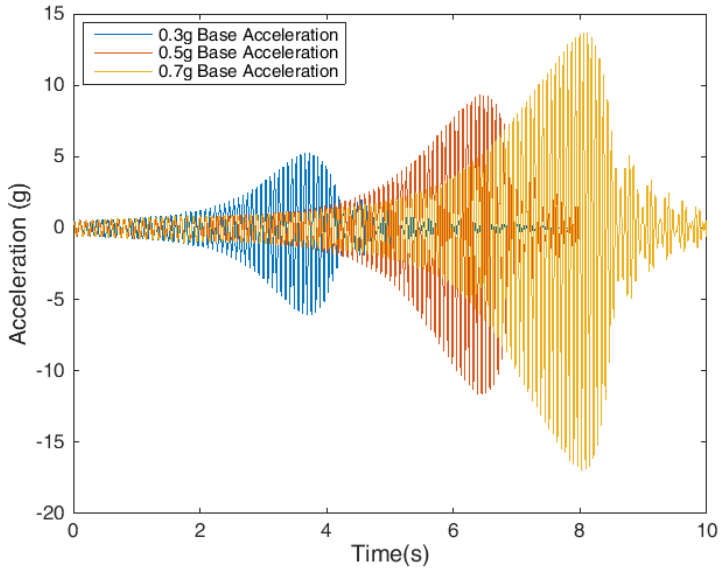

Figure 5-7 The measured plate response subjected to various base acceleration.

The noise level recorded by the AE system is generally above 40dB for 0.7g base acceleration (as shown in Figure 5-8). This is not favourable since a low threshold is desired so that the fatigue test can properly capture AE signals during fatigue damage development. Therefore the 0.5g base acceleration was selected because it was observed that the noise level is generally below 40dB for the test frequency range.

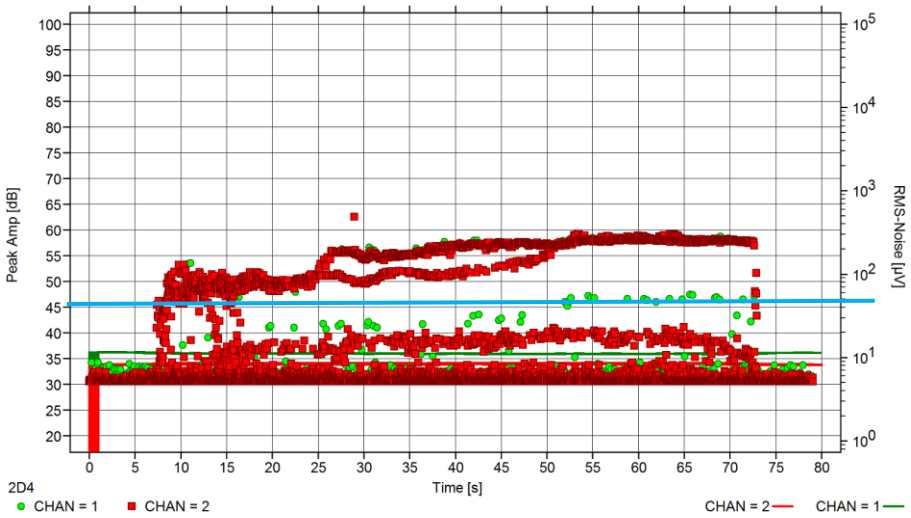

Figure 5-8 Noise level generated due to the attachment of accelerometer for 0.7g base acceleration. Blue coloured line marks the 40dB threshold.

The principle stress simulated according to 0.5g base acceleration was approximately $9.28MPa$ which is very low compared to the stress required for fatigue at 1,000,000 cycles [141] in reference to the S-N curve given in Figure 5-9. In the current work, a sufficient number of cycles is desired to avoid long duration of fatigue test.

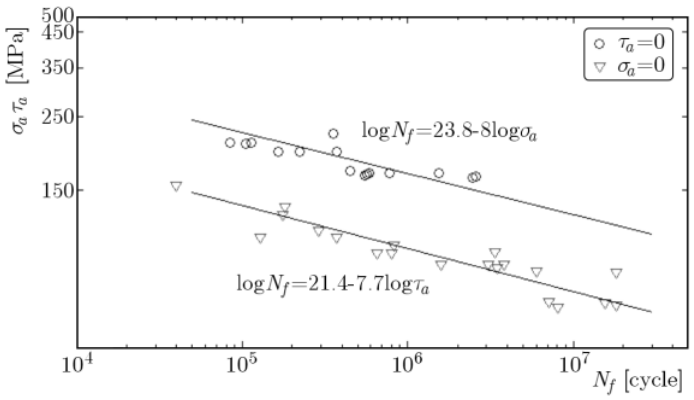

Figure 5-9 The relationship of axial and shear stresses against number of cycles for aluminium 6082-T6 [141].

Using FEA, the maximum stress was measured around the bolt holes, which implies fatigue damage is more imminent at these locations than at the mid-span. Therefore, the width of the plate was reduced as illustrated in Figure 5-10-a, to promote stress concentration. The stress concentration can be estimated using the stress concentration factor ($K_{t\alpha}$) curve for V-shaped notches [142]. The stress can be calculated as follows;

$$\sigma_{\max} = \sigma_{nom} K_{t\alpha} \tag{5-4}$$

where σ_{max} and σ_{nom} are the maximum and nominal stress respectively. The notch angle, α is approximately 110° and the width was reduced to one-third of the original width. Hence the ratio is $2h/H = 0.667$; where h is the distance from the edge as illustrated in Figure 5-11. The stress concentration $k_{t\alpha}$ was derived from the stress concentration for U-shaped notch, k_{tu}. For $h/r \sim 10$, $k_{t\alpha}$ is approximately 2.26. Therefore the maximum stress at the mid-span is approximately $9.28MPa \times 2.26 \sim 21MPa$ which is still low compared to the stress required to cause fatigue at 1,000,000 cycles. Therefore, a sharp notch was created using electrical discharge machining (EDM) along the mid-span as shown in Figure 5-10-b. The crack is expected to initiate at the tip and propagate through thickness.

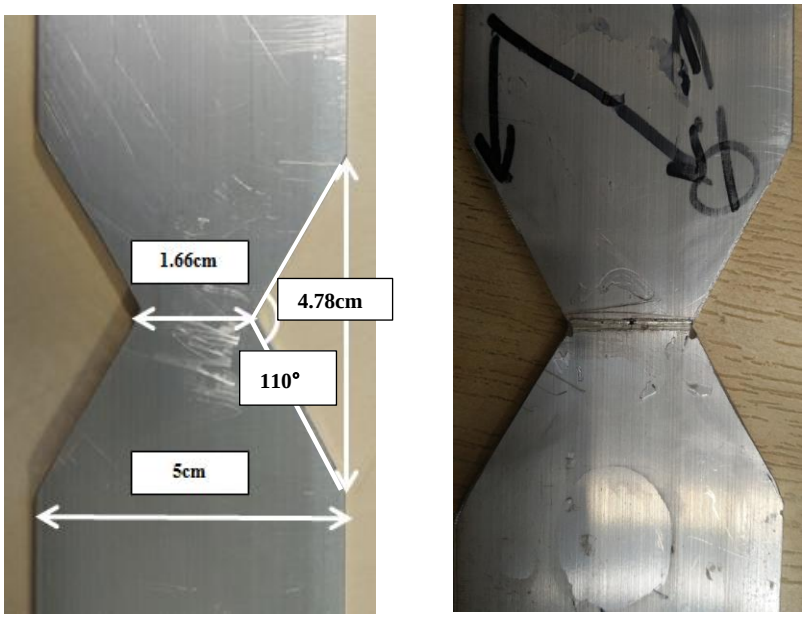

(a) (b)

Figure 5-10 The width of the plate was reduced to concentrate the stress at the notched location.

The objective of the stress analysis is to ensure the applied stress is sufficiently large and does not exceed material fracture toughness, K_C which can lead to sudden rupture. In order to evaluate the stress field near the notch, a simple model based on the Linear Elastic Fracture Mechanics, (LEFM) method proposed by Irwin [143]. This model assumes the material is isotropic and linear elastic and the the stress field is proportional to the stress intensity factor (SIF). When the SIF exceeds the fracture toughness, the cracks will propagate rapidly. Using this approach, the singularity[12] problem occurring in modelling can be avoided.

[12] Stress near the crack tip tend to increase with finer mesh in FEA.

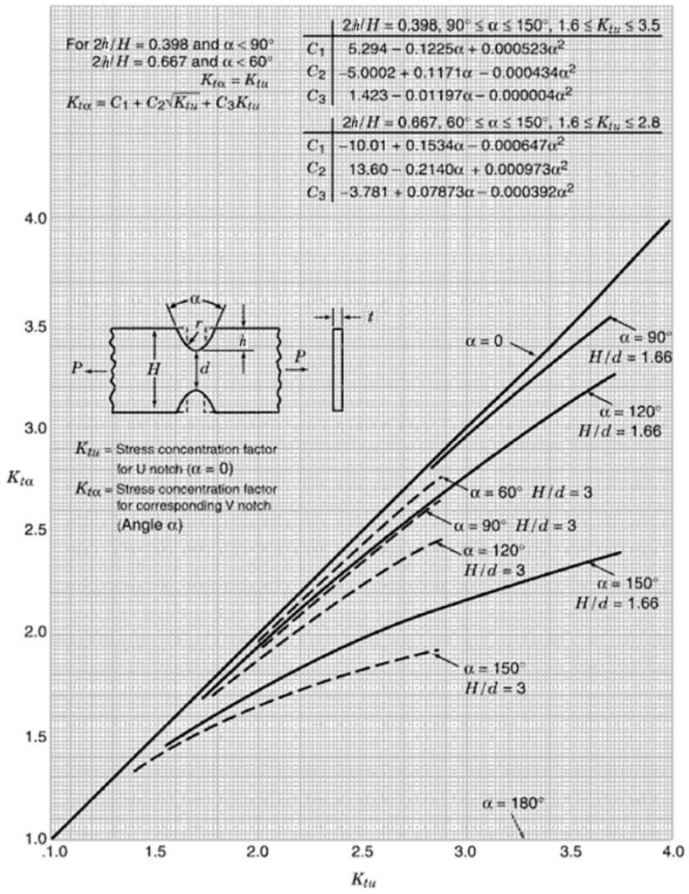

Figure 5-11 Stress concentration factor curve for V-shaped notch [142].

The SIF is conventionally used to measure the strength of local crack-tip fields. The SIF, denoted by K can be mathematically described [144] as follows;

$$K = (Y\sigma)\sqrt{\pi a} \tag{5-5}$$

where;

Y is the stress intensity correction factor

σ is the applied stress

a is the crack length

In the current work, slow propagating cracks are desired and hence a lower value of SIF than the fracture toughness is expected. For an edge crack, the stress intensity can be calculated analytically using (5-6) [144].

$$K_I = (M f_w M_m \sigma)\sqrt{\pi a} \tag{5-6}$$

where;

a is the crack length

M is bulging correction factor; in this case $M = 1$

f_w finite width correction factor; in this case $f_w = 1$

M_m is stress intensity magnification factor, which can be calculated as follows;

$$M_m = 1.12 - 0.23\left(\frac{a}{t}\right) + 10.6\left(\frac{a}{t}\right)^2 - 21.7\left(\frac{a}{t}\right)^3 + 30.4\left(\frac{a}{t}\right)^4 \tag{5-7}$$

Equation (5-7)being valid for $a/t < 0.6$ [144]. For crack size equal or larger than $1.8mm$, the SIF was estimated using the FEA model. The assumption used in the calculation is that the plate was loaded axially during crack opening where SIF is at maximum. The analysis was assumed quasi-static. The SIF values were derived using contour integral estimates [145]. To simplify the problem, a 2-D plane strain finite element model symmetrical about the mid-span (i.e. half of the plate length) was created. The crack was expected to propagate along the edge of symmetric boundary. The section thickness was assigned according to the plate width to form a homogenous solid. Seven crack sizes from $0.375mm - 2.625mm$ with increments of $0.375mm$ were selected. No symmetry boundary condition was assigned at the crack face to allow it to open. The crack front and crack tip was defined at a vertex point and the crack extension direction was set using the q vector (i.e. through thickness as illustrated in Figure 5-12).Since the crack tip is relatively sharp, the strain becomes singular at the crack tip, therefore a strain singularity formulation of the type $1/\sqrt{r}$ was included to improve the contour integral estimation. The mid-side nodes were moved to quarter points (i.e. 0.25) towards the crack tip and the element sides were collapsed. A spider web like mesh with 10 layers was created for the contour integral estimation.

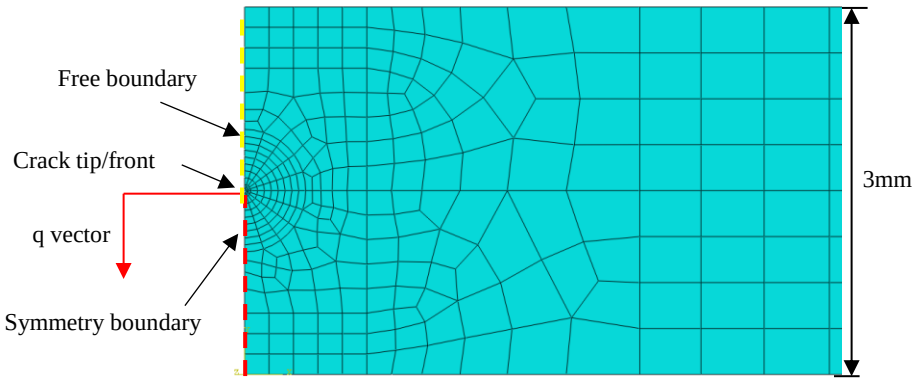

Figure 5-12 FE crack model for SIF estimation ($a = 1.5mm$).

Table 5-2 shows the estimated SIF obtained by analytical calculation and FEA. The errors of the calculated SIF are small and hence the estimated SIF for crack size above $1.8mm$ is considered acceptable. The maximum SIF was calculated for crack size $2.625mm$, which is relatively smaller than the fracture toughness. The fracture toughness of aluminium 6082-T6 is $32.5MPa\sqrt{m}$ [146]. Therefore, the crack is expected to propagate at least until 88% depth based on the applied loading of $21MPa$.

$a\ (mm)$	a/t	M_m	K_I (BS7910) $MPa\sqrt{m}$	K_I (FEA) $MPa\sqrt{m}$	% Diff
0.375	0.125	1.22	0.88	0.88	0.03%
0.75	0.25	1.50	1.53	1.52	1.23%
1.125	0.375	1.98	2.47	2.43	1.81%
1.5	0.5	2.84	4.10	3.93	4.15%
1.875	0.625	-	-	6.69	-
2.25	0.75	-	-	12.46	-
2.625	0.875	-	-	25.36	-

Table 5-2 – Estimated SIF by analytical calculation [144] and FEA.

5.2.2.3 Wave propagation analysis – monopole source

The wave propagation was studied using pencil lead break (PLB) sources and validated using FEA. The objective was to establish a correct baseline model for wave propagation

subjected to various crack depths. In reality it is difficult to replicate the actual signal of crack from PLB test. Therefore, rather than trying to replicate the signal, the objective is more to understand the relationship between the S_0 and A_0 modes that can be used for damage identification.

Mesh and analysis setup

A 2-D plain strain model of the aluminium plate was created in Abaqus FEA (version 6.14). The plate was discretized using quadrilateral element with linear shape function to model the propagating waves. The element size must be able to capture various wavelengths. The time resolution must also sufficient to avoid numerical errors. It has been noted that the frequency of the generated waves originated from crack can be as high as $100MHz$. However typical wave frequencies are within $1MHz$ where most commercial AE sensors are able to detect the signals. Wideband AE sensors from Physical Acoustics (PAC) model NANO30 were used in this experiment. Therefore, the mesh resolution must be able to cover the frequency range according the sensitivity of the sensor between $125kHz - 750kHz$. The mesh size was calculated based on the minimum wavelength derived from the wave velocity at the frequency of interest. The frequency range that is valid for comparisons with the actual AE signal is between $125kHz - 400kHz$ as shown in Figure 5-13.

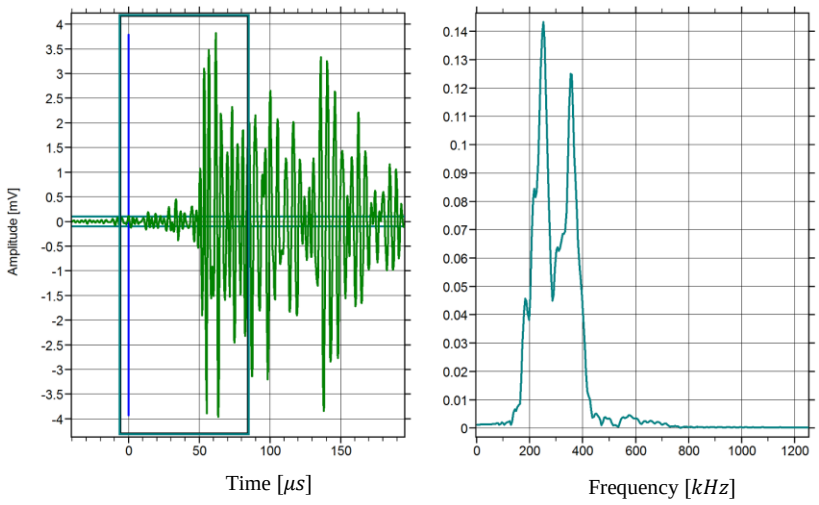

Figure 5-13 An example signal of PLB (left) and its frequency spectrum (right).

The minimum wave velocity at $400kHz$ from the dispersion curve is $3165ms^{-1}$ as given in Figure 3-10. Therefore, the recommended mesh size is $3165/400000/20 \sim 0.39mm$; 10-20 elements are required to capture the propagating waves correctly [75]. In order to have uniform mesh size across thickness, a $0.375mm$ mesh size was chosen. The time resolution is calculated based on the maximum velocity at the frequency of interest and hence, the time is approximately $0.000375/4695 \sim 0.08\mu s$. The time steps can be set as low as $10ns$ where the solution would not be affected by the time resolution [147]. The total number of mesh is approximately $1000mm/0.375mm \times 3mm/0.375mm \sim 21{,}000$ cells.

AE source functions

It has been shown that the source functions can be simulated using a step function [46], a ramp function [66,147–149] or a cosine bell function [150] as presented in Figure 5-14.

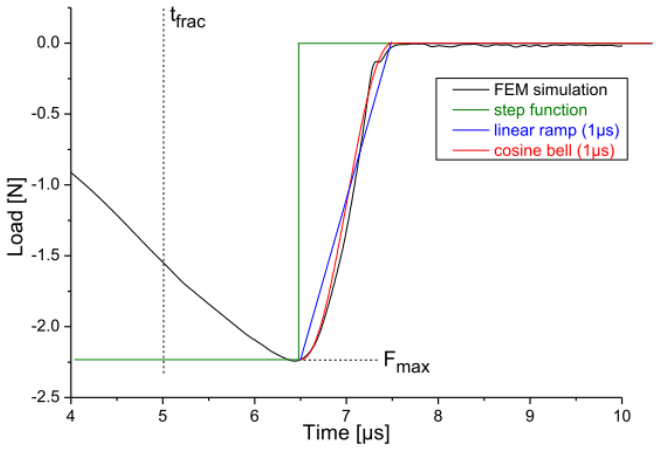

Figure 5-14 The source functions used to simulate a monopole source [147].

Sause [147] made a comparative study of different source functions using FEA. The author noted that a cosine bell function [150] was in close agreement with the waves generated by PLB obtained at far-field location. Therefore, in the present research a cosine bell function was used. The source was excited with 1 Newton force perpendicular to the plate surface at the mid-span. The displacement at $45cm$ (i.e. the location of the sensor) from the plate mid-span was recorded and filtered using a Butterworth filter in MATLAB®. The results were compared with the PLB sources.

5.2.2.4 Wave propagation analysis - crack modelling

Lee et al [151] studied wave propagation in aluminium plate emanating from fatigue cracks. They discovered that the ratio of the A_0 and S_0 amplitudes is relatively constant over the duration of fatigue test. Using a similar approach, the wave propagation subject to different length of crack was studied. Six crack depths (i.e. $0.75mm - 2.625mm$) were selected. A notch of size approximately $0.375mm$ was also created in the model. Each scenario was modelled such that the FEA simulation was initialized with pre-stressed condition in implicit analysis. The nodes at the crack face were released in Abaqus explicit. The response of displacement at $45cm$ (i.e. the location of the sensor) from the plate mid-span was recorded and filtered using a Butterworth filter in MATLAB®.

5.3 RESULTS AND DISCUSSION

5.3.1 FEA Analysis

PLB tests were conducted at the mid-span as illustrated in Figure 3-22-b in the previous section. The signals obtained by FEA and PLB were compared as illustrated in Figure 5-15. Both signals show very close agreement.

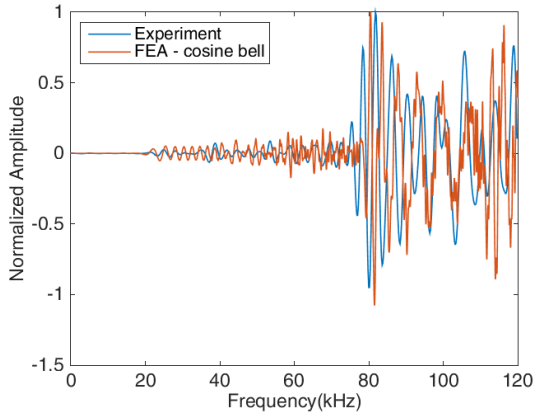

Figure 5-15 Comparison of signals (normalized) obtained by FEA analysis and PLB.

High frequency waves in PLB tests were not captured due to attenuation compared to the signal obtained by FEA. Therefore cross-correlation with Gaussian signal of central frequency $250kHz$ was carried out which follows the analysis done in the previous chapter. The envelope of cross-correlogram is illustrated in Figure 5-16. Apart from the S_0 and A_0 wave modes, a reflection of S_0 can be seen in the figure. The measurement was taken at $5cm$ from the plate ends, therefore the time delay between the first S_0 mode and the reflected S_0 is $10cm/5290ms^{-1} = 18.9\mu s$. However the time delay in the actual signal is smaller since the reflection occurs at the bolted joint (i.e. $3cm$ from the AE sensors rather than at the plate end).

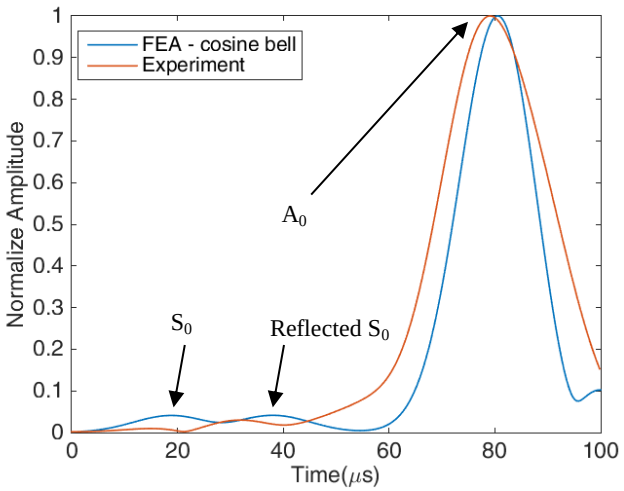

Figure 5-16 The enveloped cross-correlogram for experiment and FEA.

The time difference between the S_0 and A_0 wave modes are approximately 62.3s and 60.8s for the experiment and FEA respectively. Using SSMAL (3-32), the calculated event location is approximately $46.12cm$ (0.45% error) and $44.95cm$ (0.01% error) which is very close to the actual source location (i.e. 45cm). Therefore the model was used for the analysis of wave propagation subjected to various crack depths. Figure 5-17- shows the signals obtained for various crack extensions. Figure 5-17-b shows the enveloped cross-correlogram.

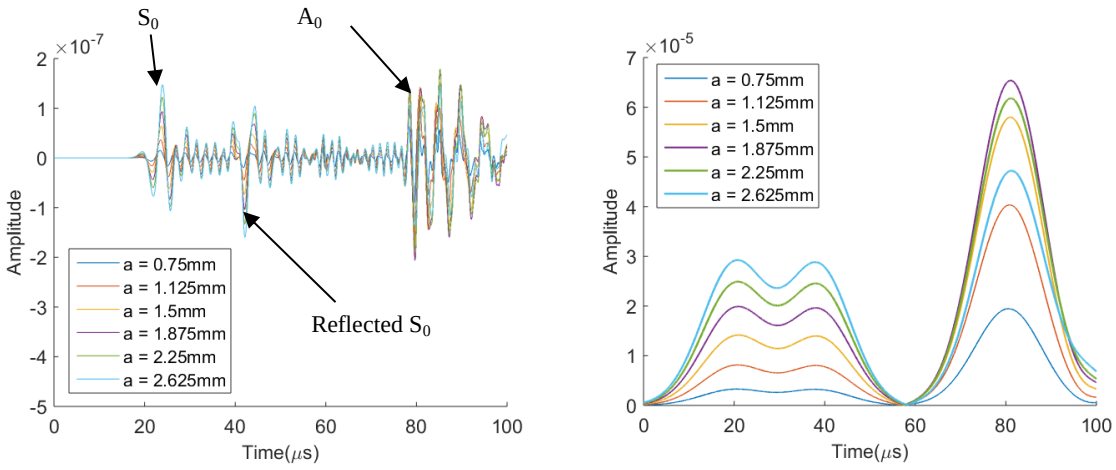

(a) (b)

Figure 5-17 (a) AE signals obtained from various crack extension in FEA. (b) The enveloped cross-correlogram.

The relationship of the S_0 and A_0 amplitudes for different crack depths was studied. The waveform is similar to the baseline apart from difference in signal amplitudes of the S_0 and A_0 with respect crack depths. It is interesting to note that as the cracks reached approximately 62% depth, the A_0 amplitudes starts to decrease as shown in Figure 5-18. A similar trend can be found in [151]. The effect of different applied stress on signal amplitudes was also carried out. The applied stress was varied $\pm 10\%$ from the nominal stress value (i.e. $21MPa$). Although the amplitudes are different for different applied loads, the ratios remain unchanged. Therefore, the ratio A_0/S_0 is independent of stress. The amplitudes of A_0 and S_0 are similar at approximately 90% depth. Using this relationship the damage sensitive features between the S_0 and A_0 modes can be mathematical derived as follows;

$$\alpha = \frac{A_0 - S_0}{A_0} \tag{5-8}$$

α is a dimensionless parameter which takes into account the variation of A_0 and S_0 amplitudes. The damage index α varies almost linearly with crack depths until it reaches 62% depth. The α values drop rapidly beyond this depth and become negative when the A_0 amplitudes are less than the S_0 as shown in Figure 5-19.

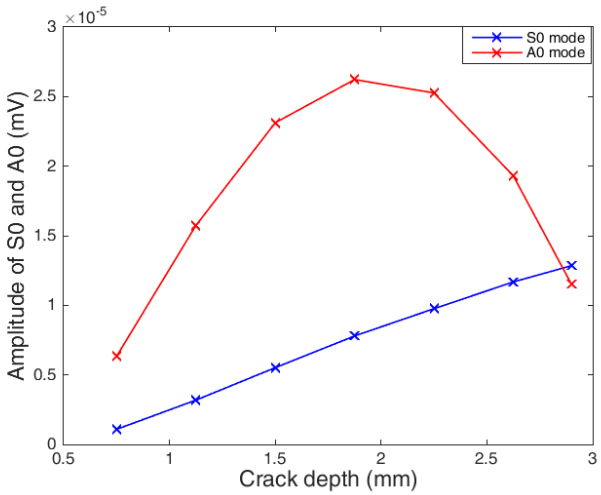

Figure 5-18 Difference in S_0 and A_0 amplitudes with crack depths.

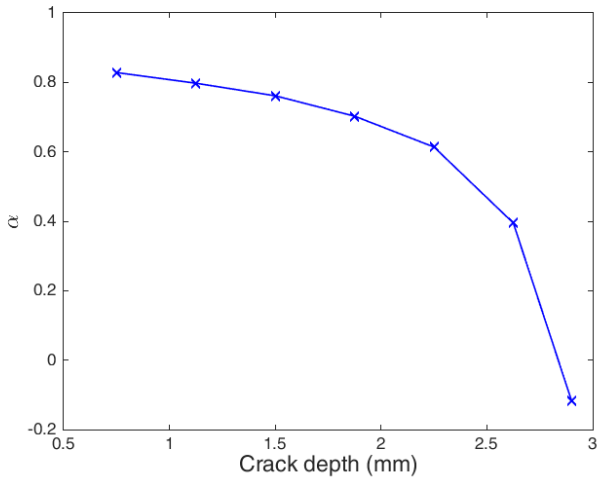

Figure 5-19 α values with crack depth.

5.3.2 Vibration-Induced Fatigue Test

A series of modal analysis was conducted on the plate to determine the resonance frequency during healthy and damage conditions. It was noted at the beginning of the test that the natural frequency of the plate was reduced to $16.31Hz$ due to the additional mass of accelerometer and AE sensors. Therefore, the shaker was set to operate at $16.31Hz$. In the first run, the test lasted for 12,700 cycles (roughly 13 minutes). The acceleration recorded on the plate reduced immediately as the resonance frequency of the plate shifted. The test was stopped and the plate was inspected visually. However, the crack

was not observed, although the natural frequency reduced to $14.03Hz$. The frequency of the shaker was set accordingly and the test was restarted and stopped after 806 cycles. This time the crack emerged. The crack depth was measured about $\cong 2.7mm$ depth as illustrated in Figure 5-20. The resonance frequency was reduced to $13.25Hz$. The procedures were repeated until the plate fractured.

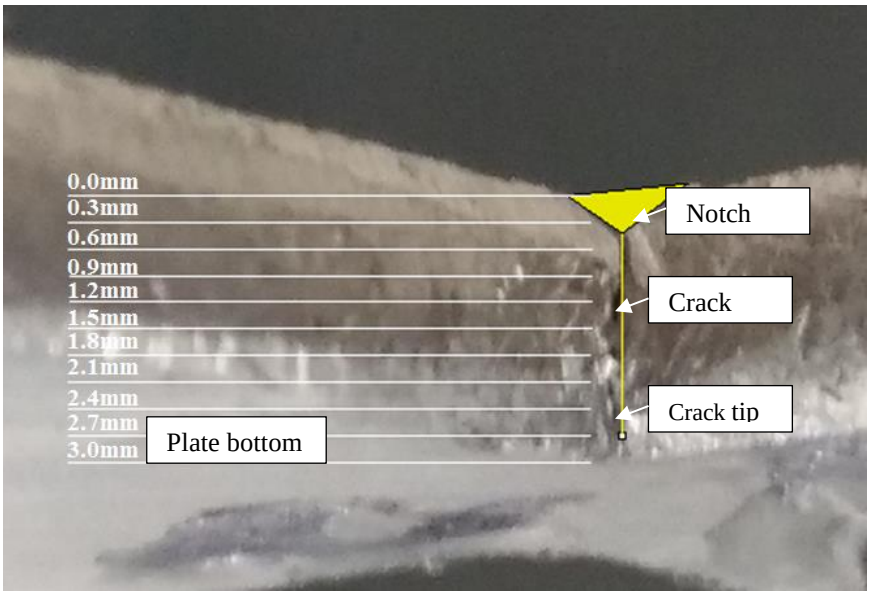

Figure 5-20 Crack extension approximately 93% of plate thickness. Looking from side plate.

AE signals were filtered by durations and amplitudes. The recorded events contain various form of signals correspond to different stages of damage. AE signals from each stage were extracted and loaded in MATLAB®. The signals were correlated with Gaussian modulated cosine signal of $250kHz$ central frequency. Figure 5-21 shows distribution of signal amplitudes from start-up. Signals in the marked region (1) contain small amplitudes of S_0. However majority of the signals are irregular with no distinction of S_0 and A_0. These signals were generated mainly from microscopic activities such as micro fracture in the early stage of damage [135]. Signals in region (2) are most likely correspond to crack initiation and propagation. The plate acceleration reduced abruptly during these events due to reduction in structural stiffness. The natural frequency of the

plate shifted by $2.28Hz$ ($16.31Hz - 14.03Hz$). However, the cracks were not visible during inspection which implies the cracks were buried in the mid-section.

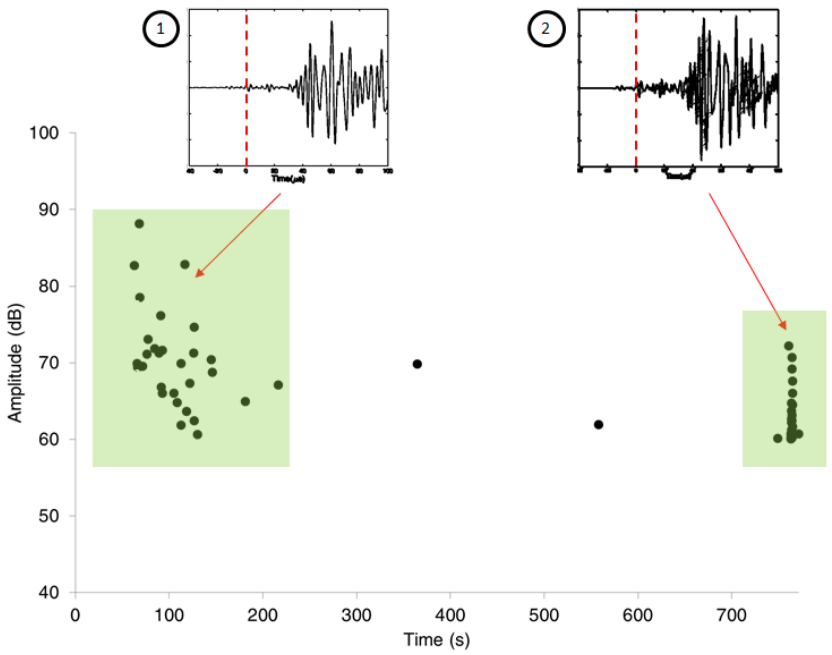

Figure 5-21 Distribution of maximum amplitudes. Signals (1) shows small amplitude of S_0 wave modes compared to A_0. Signals (2) corresponds to crack initiation and propagation but buried in the mid-section.

After the test was restarted, a number of signals emerged at about 80dB i.e. signal (3). It is noted that the A_0 amplitudes are smaller than the S_0. The inference that can be made from this observation is that the cracks in the mid-section continue to propagate above 90% depths. Another set of signals, marked (4) and (5) in Figure 5-22 correspond to crack propagation from the notch. The majority of maximum amplitudes from these signals are higher than that of signal (3). The damage evolution can be seen by the increase of S_0 amplitudes. A reduction of A_0 amplitudes as seen in signal (5) was also observed as soon as the measured acceleration dropped (i.e. 775 seconds of test time). The crack was visible as illustrated in Figure 5-20, after the test was stopped.

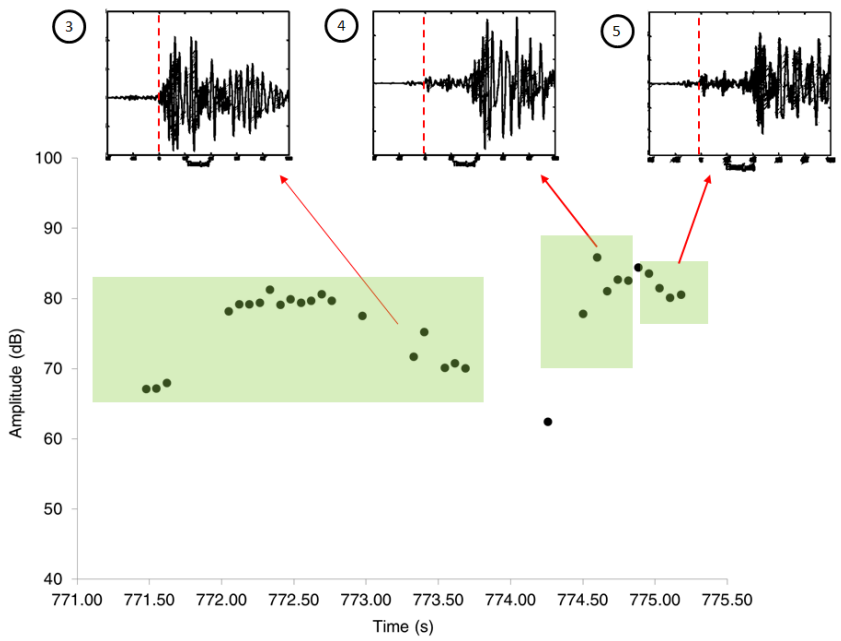

Figure 5-22 Distribution of maximum amplitudes in the second run. Signals (3) have large amplitude of S_0 mode compared to A_0. Signals (4) and (5) correspond to cracks propagation from the notch.

Within the last run of the fatigue test, a number of signals were recorded in the marked area (6) as shown in Figure 5-23. These signals carry larger amplitudes S_0 mode than the A_0 mode until the plate fractured. Signal (7) contains a series of weak pulse-like signals appearing immediately before fracture. An interesting observation can be made from the fracture surface as shown in Figure 5-24. The inclusion that caused crack initiation is depicted by a dark region below the notch close to the centre of the mid-section. This inclusion is believed to be the reason why the crack was not visible after the first run. A slow crack growth region can be seen across the crack face.

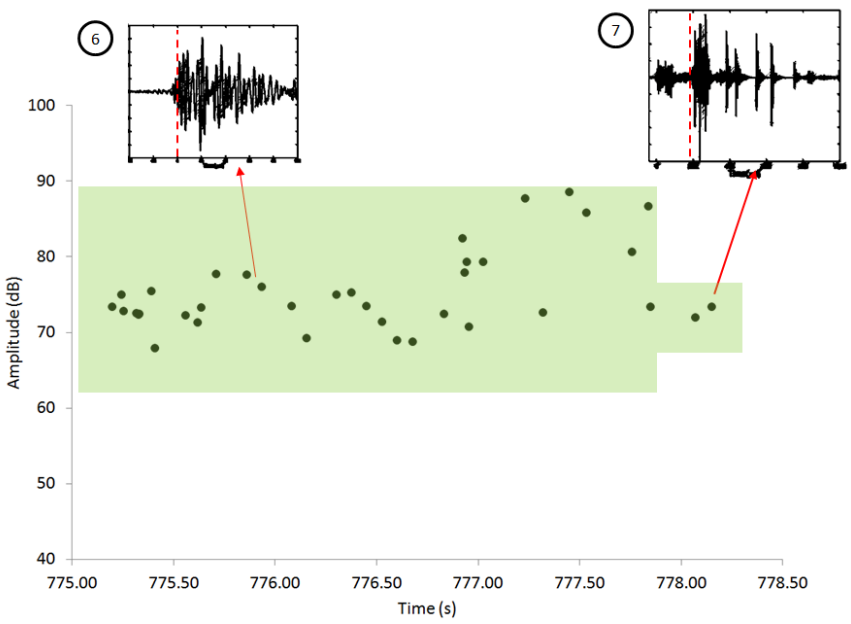

Figure 5-23 Distribution of maximum amplitudes in the final run. Signals (6) correspond to crack propagation in the remaining thickness. Signals (7) are signals emerged immediately before fracture.

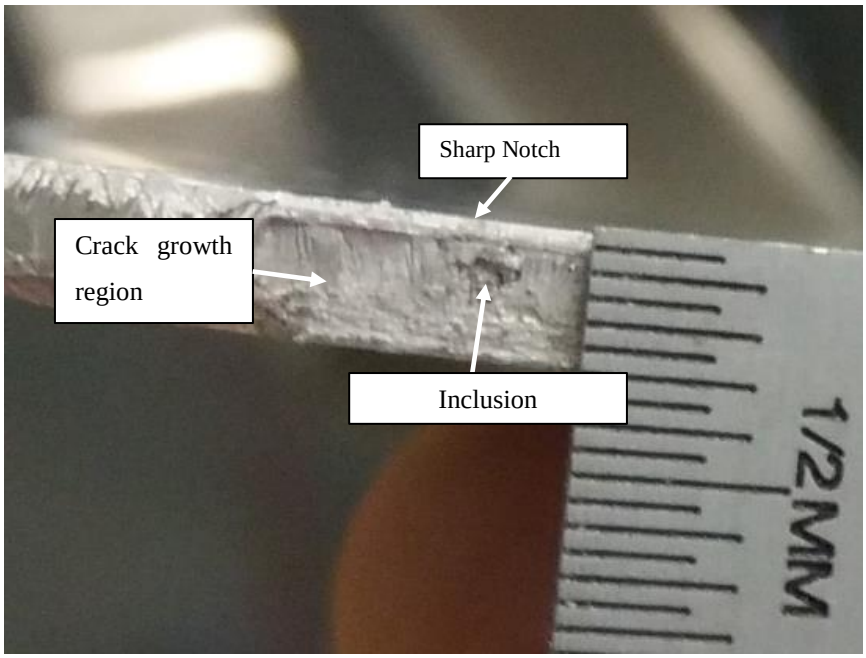

Figure 5-24 Fracture surface

The signals from each damage scenario were extracted and evaluated using the proposed damage sensitive feature. The mean, $\bar{\alpha}$ median, $\tilde{\alpha}$ and standard deviation, were calculated and tabulated in Table 5-3. A whisker plot of each signal is shown in Figure 5-25.

Signal No.	Mean ($\bar{\alpha}$)	Median ($\tilde{\alpha}$)	Standard deviation (σ)
1	0.47	0.13	0.42
2	-0.58	-0.50	1.12
3	-0.46	-0.51	0.42
4	0.91	0.91	0.03
5	0.55	0.78	0.64
6	-0.35	-0.50	0.40

Table 5-3 – The mean, $\bar{\alpha}$ median, $\tilde{\alpha}$ and standard deviations of different signals.

These results suggest a good agreement with the previous observations. The calculated mean and median of Signal (1) are 0.47 and 0.13 respectively. Some of the signals do not have distinct S_0 and A_0 modes. Signal (2) and (3) correspond to crack extension above 90% depth. The $\bar{\alpha}$ and $\tilde{\alpha}$ for both signals are negative. However, there are signals with α values outside interquartile range (IQR) which is regarded as the outliers. The cracks were not visible until signal (5) appeared. Signal (6) and (7) corresponds to crack propagation before fracture. Therefore the majority of α are negative values.

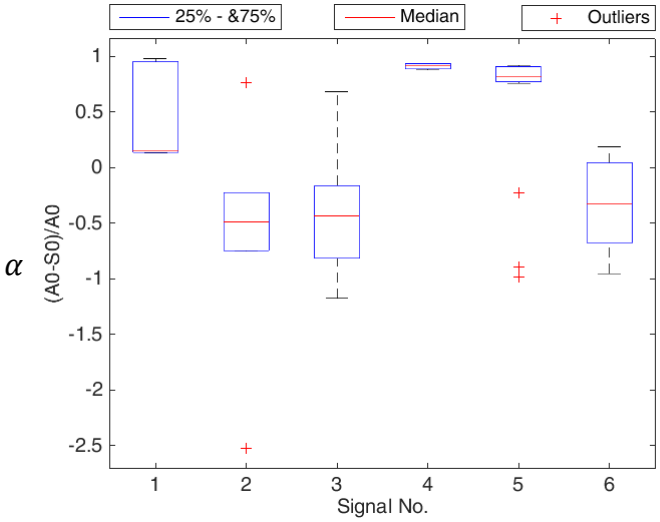

Figure 5-25 Whisker plot of various signal sets.

To explicitly study the signals, cross-correlation was carried out between the signals obtained by FEA of different crack depths and the actual signals of cracks. To ensure a high correlation is achieved, a two-stage correlation is proposed. In the first stage, the signals from each analysis were cross-correlated with Gaussian modulated cosine signals. The cross-correlograms were enveloped using similar method used in section 5.3.1. In the second stage, cross-correlation was then carried out with the enveloped cross-correlograms of FEA and AE signals. Both enveloped cross-correlograms were normalized with their respective maximum value in prior since both analyses were made independently. Therefore each analysis will have similar trend of signals with distinct A_0 and S_0. It is noted that the sampling rate used in the experiment is 5MHz, which is smaller than the time steps used in FEA i.e. 10ns. In order to ensure the number of samples is similar, the enveloped cross-correlograms were averaged for every 20 data points which make total number of 500 samples this being consistent with the AE signal samples. The two-stage cross correlation was done for each set of signal (i.e. signal 1 to signal 6). The calculated values are shown in Figure 5-26.

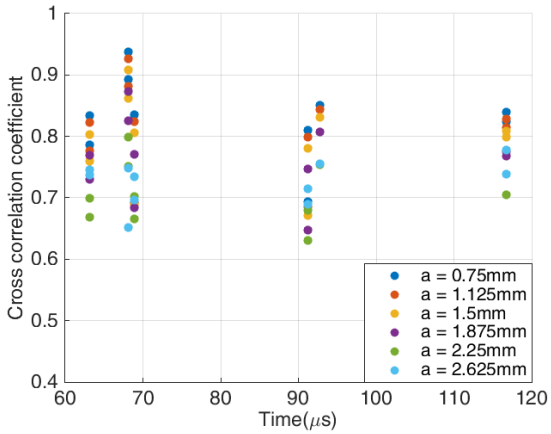

Signal 1

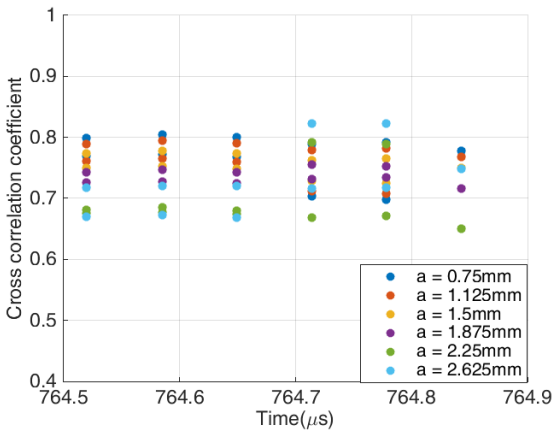

Signal 2

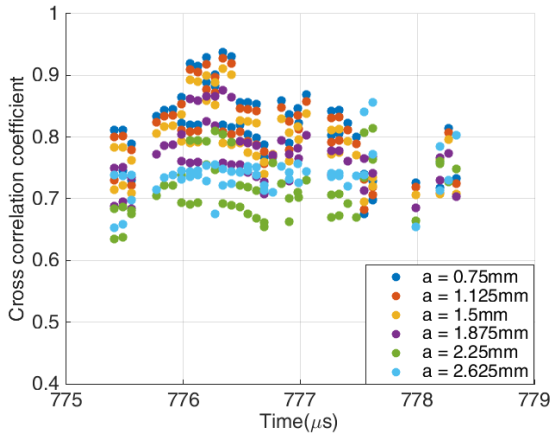

Signal 3

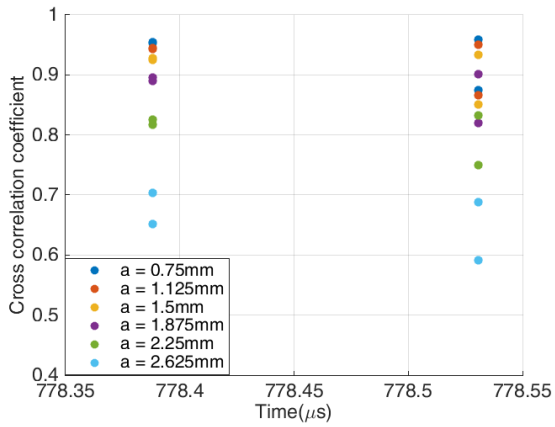

Signal 4

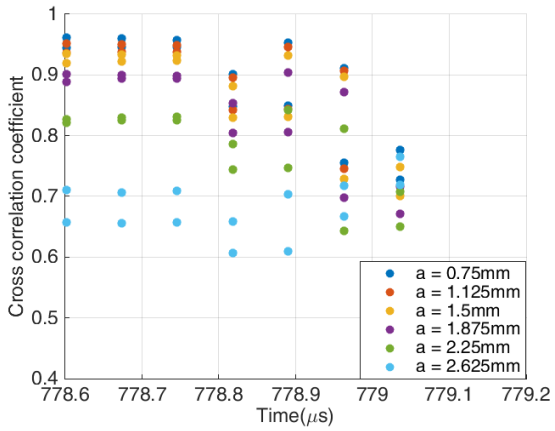

Signal 5

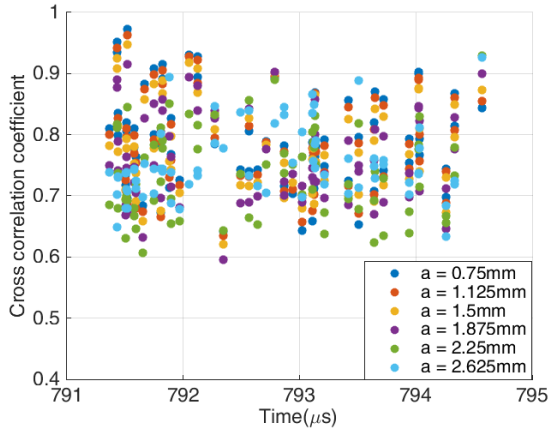

Signal 6

Figure 5-26 Cross-correlation coefficients of the enveloped cross-correlograms between FEA and AE signals for various crack depths.

An interesting observation can be made comparing the calculated coefficient to the means, medians and standard deviations of α values determined in the previous analysis. Clearly the coefficients are scattered presenting some trends that may be related to crack propagation. Signal (2) and (5) consist of signals immediately before the occurrence of the large crack extension that caused the natural frequencies of the plate shifted abruptly. The coefficients related to 0.75mm and 2.625mm crack depths show opposite trend of decreasing and increasing coefficient with time. This is consistent with the reduction of α values as shown in Figure 5-25. After the test restarted, the cracks continued to propagate

slowly. This is proven by the increase of coefficient correspond to 2.625mm depth and the negative α values calculated. The large number of signals/coefficients recorded reflects the high activity of crack propagation. However, the calculated coefficients are even more scattered. High coefficients become noticeable in signal (3) and signal (6) which imply larger cracks. In contrast, less number of signals with clear gap of coefficients calculated for 0.75mm and 2.625mm crack depth can be seen in signal (4) and in the beginning of signal (5). In this scenario, high coefficients were calculated for 0.75mm crack depth while low coefficients were calculated for 2.625mm crack depth which implies the cracks are mainly close to the surface. Therefore, the proposed damage sensitive feature (i.e. α values) is sufficient to quantitatively evaluate the severity of damage. The test was repeated using different plates of similar properties and dimensions. This time the phase track option was used which tracks phase change, and hence the excitation frequency is automatically tuned to match the resonance frequency. This technique eliminates the need to manually change the excitation frequency as damage evolves. A swept-sine test was done in prior to search the natural frequencies. During the test, a low acceleration level was used in order to avoid crack propagation. The shaker was set with a minimum and maximum abort limits that allow the system to automatically stop when the plate fails. Cumulative counts were compared with AE signal energy. During the test, a number of high amplitude signals were recorded. High amplitude signals were recorded at the beginning of the test between 230 – 348 seconds. These signals are believed to be generated from the usual phenomena of early stage of damage such as micro fracture occurring at the beginning of fatigue test. These signals are less obvious in terms of S_0 and A_0. From the plot in the middle of the test duration an indication of crack propagation is depicted by the increase of cumulative energy and counts between 1500-2200 seconds or 25 – 37 minutes of the test duration. Using similar approach as in the previous chapter, the AE signals of the events were extracted and the severity of damage was evaluated using the proposed damage sensitive features. The parameter was evaluated for a number of intervals. The located events were only recorded between 230 - 348 seconds, 1181 - 2300 seconds, and 3300 – 3900 seconds as depicted by the peaks of signal counts in Figure 5-27.

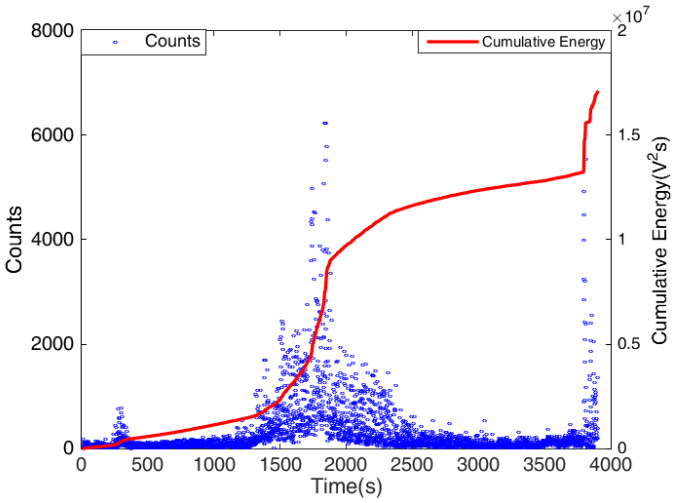

Figure 5-27 Counts (left axis) and cumulative energy (right axis) recorded for plate 2.

A block of signals of every 100 seconds were extracted and analysed. Figure 5-28 (top) shows a whisker plot of α for 1181 - 2300 seconds interval. The median $\tilde{\alpha}$ for each block is above zero with the highest recorded values between 1550 – 1750 seconds. The signal amplitudes are consistently above 60dB and sustained for a longer duration which contributed by the large amplitudes of A_0 mode. The high $\tilde{\alpha}$ values imply the crack started to initiate and propagated from the notch. The negative α are mostly outliers of these data sets.

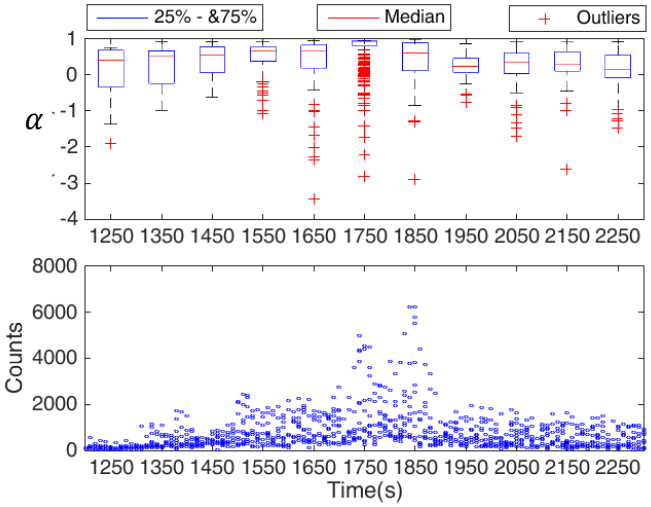

Figure 5-28 A whisker plot of α (top) and counts (bottom) recorded for plate 2 between 1181 – 2300 seconds.

The median $\tilde{\alpha}$ and mean $\bar{\alpha}$ started to reduce after 1750 seconds. These parameters close to zero which implies damage reached above 62% depth. There are no located events after 2300 seconds. A reduction of resonance frequency was also noted.

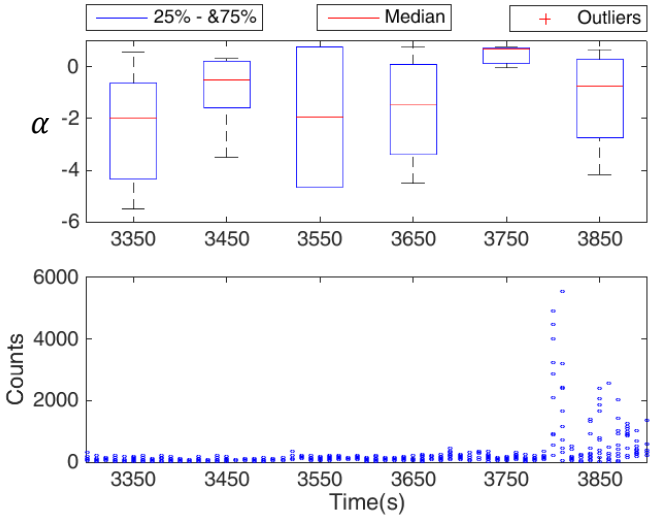

Figure 5-29 A whisker plot of α (top) and counts (bottom) recorded for plate 2 between 3300 – 3900 seconds.

The $\tilde{\alpha}$ and $\bar{\alpha}$ reduced to negative values between 3300 – 3900 seconds. The inference can be made such that the cracks have propagated above 90% depth. However a positive $\tilde{\alpha}$ was calculated between 3750-3850 seconds. The high amplitude signals are mainly contributed by the A_0 mode above 60dB. However the signal counts are relatively low compared to 1181 - 2300 seconds interval.

5.4 CONCLUDING REMARKS

Acoustic emission monitoring of vibration-induced fatigue of an Aluminium 6082-T6 plate specimen has been successfully carried out. The experiment was designed using hybrid approach which involved vibration model correlation crack modelling, and wave propagation study using FEA. The fatigue test was designed such that the plate was excited in bending mode which promotes mode I fracture (i.e. opening mode). The methodology was to first evaluate the dynamic properties of the plate using modal analysis. The FEA simulations were carried out to evaluate stress distribution and stress

intensity factor for various crack depths. Thus, the applied load required for crack propagation to at least 90% depth was estimated. This allows damage assessment using the proposed damage sensitive feature over a wider range of crack lengths. The severity of damage was estimated using a dimensionless parameter derived from the difference of amplitudes of the fundamental wave modes. The relationship was established based on the fact that the A_0 and S_0 amplitudes decrease and increase respectively with crack depth, as reported in the literature. Using this relationship, damage extent can be predicted directly from the acquired signals. The frequency of waves that travel in the aluminium plate was identified through wave propagation analysis. Cross correlation with Gaussian modulated cosine signal of central frequency $250kHz$ improved wave mode identification. Signals corresponding to AE source/cracks generated at mid-span were evaluated. Two different plates of similar properties and geometry were tested. The first test was done by manually changed the excitation frequency to match the resonance frequency of the plate. Using this approach, the signals corresponding to crack propagation could be identified as soon as the acceleration measured on the plate dropped. The second plate specimen was tested using phase track technique to ensure the excitation frequencies automatically tuned to match the resonance frequencies as damage evolved without stopping the test until the plate failed. The AE signals from both tests were extracted and the proposed damage sensitive feature was used to predict damage extent. The results obtained from the analysis of mean, $\bar{\alpha}$ median, $\tilde{\alpha}$ of the proposed feature, throughout the test show that the positive α values are generally related to crack propagation from the notch. The spread of α are clustered with small standard deviation. The A_0 amplitudes started to decrease relative to S_0 during crack propagation. The mean, $\bar{\alpha}$ and median, $\tilde{\alpha}$ are negative when cracks already reached 90% depth. This trend was observed towards the end of the test. The calculated damage sensitive features were compared with cross-correlation between FEA and the actual cracks signals for various depths in a two stage cross-correlation process. The first stage was done between FEA signals and Gaussian modulated cosine signals. The cross-correlation was also carried out between the actual signals of cracks and Gaussian modulated cosine signals. The enveloped cross-correlograms from each analysis were then cross-correlated in the second stage to find similarity of the signals. Consistent observation was found with the

calculated coefficients and the proposed damage sensitive feature particularly before the abrupt reduction of acceleration and natural frequencies. Therefore, the analysis of damage sensitive feature alone is sufficient to measure the severity of damage. However this technique is only limited to mode 1 crack and thin structures where the fundamental wave modes are significant.

CHAPTER 6

RESEARCH SUMMARY, CONTRIBUTIONS AND FUTURE WORKS

6.1 SUMMARY

The current research is motivated by the recent problems of vibration-induced fatigue of piping system reported by the Health and Safety Executive (HSE) [1] for offshore process plants in the North Sea. Guidelines have been published by the Energy Institute [3] which provides assistance for operators in the development of their own management system related to vibration problems in process piping. The guidelines involve qualitative assessment of determining the likelihood of failure (LOF) as a basis to identify potential threats which priorities more formal quantitative methods. However the LOF is not an absolute probability of failure. One of the recommended methods to quantify damage is by measuring dynamic strain. However, it is learnt that using strain gauges can neither detect nor locate damage unless the location of damage is known a *priori*. The strain measurement can be insensitive to crack propagation if damage is small and embedded deep in the structure. Their usage allows only identifying whether fatigue issue exists. Therefore, other feasible options are suggested without the requirement of a specific method, this being open to further research. Currently, "passive" non-destructive techniques (NDT) are considered useful over "active" techniques because do not require continuous supply of artificial sources/signals. The sources are only detected upon growing defects. The important benefit of "passive" techniques is that the detection is obtained at a very early stage of damage and in this study, this consideration led to the use and study of Acoustic Emission (AE) technique. AE is related to energy dissipation due to rapid change of stress state within a material such crack initiation or crack extension. These advantages promote their usage in a wider application of damage identification that is paramount in Structural Health Monitoring (SHM). SHM focuses on

damage identification and prediction through observation over time using damage sensitive features derived from measurements. The features are parameters related to structural degradation or changes in process performance overtime. The SHM strategies adopted in the current research follow the hierarchal structure of damage identification proposed by Rytter [65] which cover three levels as follows;

- Level 1 - Damage detection and signals discrimination
- Level 2 - Damage localization
- Level 3 - Damage extent assessment

The above strategies combine detection and signal discrimination/classification in level 1. Damage detection in AE requires dedicated signal processing techniques to obtain meaningful information, and the classification of signals according to various damage stages is very important. The discrimination of signal in level 1 allows only the filtered signals to be used for localization, in Level 2. Since localization in AE is based on the time of arrival (TOA), it is important to obtain the correct TOA to minimize the source localization errors. Level 3 requires a combination of techniques to predict the damage extent. Normally, level 3 is conducted by ultrasound technique (UT) where the geometric shapes of damage are deduced from the received signals (reflection). It has been shown in the literature that AE is capable to characterize damage by studying the relationship of AE count rate with crack propagation rate [57,59]. This method is however limited to simple problems using standard test methods and involves some limiting assumptions. To extend the research in Level 3, a dedicated experimental setup using AE monitoring is required which is able to monitor the fatigue damage evolution in a simple structure under vibration loading. Given the current vibration problem in the oil and gas industry, the objectives were established mainly to develop a SHM technique for detection, localization and identification of vibration-induced fatigue taking into account the environmental noises based on the study of vibration and elastic wave propagation in structures with simple geometries. A few research gaps have been identified in these research areas. There are two aspects of novelty developed in this research Some specific aspects were reported including experimental design of a non-standard fatigue test and finite element modelling of wave propagation. In the literature review chapter, an

overview of damage identification methods and their implementation in piping system was explored. AE is commonly generated in response to structural deformation and degradation. Their advantage in detecting damage at the same time it occurs is important which allows analysis of signals generated from fatigue damage during the onset of crack extension. In the current research, crack extension under mode I loading was studied due to its importance in most of the cases met in the industry. It is understood that there are many types of waves in mechanical structures, which depend on crack type, size, and orientation. And wave identification is important in this type of signal analysis. It is known that Rayleigh waves can be seen in thick structures having wavelength equivalent or less than the structural thickness. Rayleigh waves were observed in a carbon steel pipe of 50mm thickness. Waves that are guided by geometrical boundaries having wavelength larger than the structural thickness, exhibit so-called Lamb waves. In general there are two types of Lamb waves (i.e. symmetry and asymmetry about mid-plane). The wave velocity is no longer constant but depends on wave frequency and these types of waves were observed in 6082-T6 aluminium plates of 3mm thickness. It was learnt that the number of wave modes in pipes is greater than in plates. However the L(m,n) family modes in pipes consist of all Lamb waves in thin plates. Hence the wave modes identification in pipes is more complex than in plates. To understand different type of waves in both structures, a study was carried out using pencil lead break (PLB) sources (i.e. artificial crack signals). A number of measurement distances from AE sources were studied on the thick pipe to identify the wave modes that trigger the acquisition system using low threshold and high threshold settings. The average velocity measured in close-arranged AE sensors was very consistent. In this setup, the wave that triggered the acquisition system was identified to be the L(0,5) mode from the wavelet transformation. However for far-field sensor arrangement, the waves that triggered the sensors were no longer the L(0,5) mode due to attenuation. Some sensors were triggered by different wave modes which travel at different wave speed. This inconsistency caused errors to the located events. Using high threshold, the events generated by PLB tests around the pipe were accurately located. High threshold allows only the time of arrival (TOA) triggered by the larger amplitudes signals. The velocity calculated was approximately $3000ms^{-1}$ in all sensors, which is similar to the Rayleigh wave velocity i.e. approx. 90% of the

velocity of S-waves in steel. This study shows that Rayleigh waves are in fact useful in source localization in thick structure. In the second part of the study, the Single Sensor Modal Analysis Location (SSMAL) technique was used for locating AE sources on thin aluminium plates. This technique uses Lamb waves by manipulating time delay of symmetric and asymmetric waves. A shortcoming of using SSMAL is that the technique depends on the arrival time of the S_0 and A_0 which is difficult to obtain due to dispersion of flexural waves (i.e. asymmetric waves), this motivating the use of cross correlation of AE with Gaussian modulated cosine signals. One of the parameters defining the spread of the Gaussian distribution is the standard deviation σ. Effectively, the spread of the distribution has to be equivalent to the spread of the S_0 and A_0 waves to obtain the correct signal peaks corresponding to these wave modes this leading to the study on this parameter for damage detection. It was found that Gaussian modulation of central frequency $250kHz$ with $\sigma = 9/10\mu s$, which corresponds to signal bandwidth of $60Hz$ provides the least error (i.e. 0.7%) of the located events compared to the actual PLB locations. This study has shown that the wave mode identification could be enhanced using cross correlation, and hence improve the source localization. It is known that in SHM applications, the output from continuous monitoring and online measurement can be prohibitively large. A similar problem has been encountered in the fatigue test of the carbon steel pipe conducted in the present research. This problem requires a dedicated signal analysis and statistics tools to estimate the features obtained either directly from AE signals or indirectly from explicit parameters derived from the measurement. The objective of the fatigue test was to evaluate whether AE can be an effective method for continuous monitoring of vibration-induced fatigue pipe. Although in theory, the change of physical and dynamic characteristics can be related to damage, however, this is not obvious from the frequency analysis of the damaged pipe. The frequency associated with damage could only be seen as soon as the excitation was removed from the system. The emerging frequencies are similar with the increase of the recorded strain frequencies. A damage sensitive feature was established using the actual number of cycle and the calculated cycles from the strain measurement. The trend shows good agreement with the acoustic emission energy distribution. However the errors of the located events are significant due to many false events recorded although a high detection

threshold was used. Therefore, a study of the uncertainties associated with source localization was done by using the Bayesian estimation. Bayesian estimation evaluates the most probable effective coefficient (EC) derived using the cross correlation of signals of the located events. EC measures the minimum degree of similarity of the correlated signals taking into account the maximum and minimum coefficients from each signal combination. Using this relationship, if all signals are similar then EC equals to one. The Bayesian estimation was carried out for a number of time intervals considering the mean of the posterior distribution as the most probable EC. The *prior* distribution was taken from a set of artificial signals of cracks generated by pencil lead break (PLB). The use of signals from PLB tests as the *prior* is considered novel since such approach has never been done in the past to the knowledge of this author. The *prior* distribution is updated with the data obtained from the located AE events. The estimated *posterior* means EC were taken within 95% credible intervals, and compared with the means obtained from PLB tests. For comparison with the signals generated from damage, the maximum time of arrival Δt_{max} was limited in the acquisition system to only capture the events generated near the weld, where damage accumulated. It is learnt that the asymmetric sensor arrangement on the pipe created four different sets of isosceles triangle. From this arrangement the weld intersects with the circumcentre and hence Δt_{max} can be effectively applied which limits the assessment area near the weld. This technique could be used in real application for damage detection with known locations in prior. The energy of the signals from the filtered located events were obtained and compared with the estimated EC. Both the energy and the estimated EC are in very close agreement and shows higher EC values. This observation provides strong evidence that Bayesian estimation can be an effective method to quantify the uncertainties of the located events. The proposed method is considered novel since it only requires the minimum number of sensors for planar localization compared to the conventional method which require many sensors (i.e. overdetermined system of equations) to estimate the uncertainties. Another benefit of using cross correlation is that it does not rely of the time of arrival of signals reported by acquisition system as in conventional methods, and hence remove the dependency on signal threshold. The work so far has covered Level 1 and 2 of the SHM strategy. To qualitatively estimate damage extent under Level 3, an experiment trial of

acoustic emission monitoring of vibration-induced fatigue for a set of 6082-T6 Aluminium plates were carried out. The plates were relatively thin to ensure Lamb waves can be detected during fatigue damage. The plates were excited in bending mode which promotes mode I fracture. It was identified that the extraneous noises were mainly generated from the joints, fixtures and sensors mounted on the plate during the test. Thus, a non-standard test method was designed to ensure the noise is eliminated from the measurement. To achieve this, a hybrid approach which involved vibration analysis, cracks modelling, and wave propagation using FEA was conducted. From these studies, a low noise level below 40dB was achieved to ensure low amplitude signals associate with damage could be obtained. This threshold value is relatively small compared to many fatigue test conducted in the literature (i.e. common signal threshold used above 50dB due to noise from the supports). This achievement provides a platform for future analysis if a noise level below 30dB is desired. The experiment also enabled the cracks to propagate for at least 90% depth. The severity of damage was estimated using a dimensionless parameter with damage sensitive features (α) derived from the amplitude difference of the fundamental wave modes. The relationship was established based on the fact that the A_0 and S_0 amplitudes decrease and increase with crack depth as reported in the literature [151]. Using this relationship, damage extent can be predicted directly from the signals. Cross correlation with Gaussian modulated cosine signal of central frequency $250kHz$ was carried out for wave mode identification. The AE signals recorded from the fatigue tests were extracted and the proposed damage sensitive feature was used to predict damage extent from the analysis of mean, $\bar{\alpha}$ median $\tilde{\alpha}$, and standard deviation, σ. It was concluded that the positive α values are generally related to crack propagation from the notch. The A_0 amplitudes started to decrease relative to S_0 during crack propagation. The mean, $\bar{\alpha}$ and median, $\tilde{\alpha}$ are negative which implies cracks already reached 90% depth. The negative values were calculated due to the A_0 amplitudes being less than the S_0 amplitudes. To validate the proposed feature, the AE signals were correlated with FEA model of different crack depths in a two stage cross process. The first stage involves correlation of signals obtained from the experimental test and FEA with Gaussian modulated cosine signals of central frequency $250kHz$. In the second stage, cross-correlation of the enveloped correlogram from the first stage was carried out

to obtain coefficients for each AE signal with respect to various crack depths. High levels of correlation were calculated for a 2.625mm crack depth immediately before large reduction of the resonance frequency occurred which implies fast crack propagation. This is consistent with the negative α values obtained. The opposite trend was observed for 0.75mm crack depth where low levels of correlations were obtained. In contrast, high level of correlation for the 0.75mm crack depth was calculated for positive α values. This method is considered novel for the assessment of crack extension or severity of damage under Level 3. The method is however valid for thin plates where Lamb waves exist, and the crack is assumed to propagate through thickness under mode I. In short, the outputs from the current research provided various opportunities to be applied in industry by using Acoustic Emission monitoring.

6.2 CONTRIBUTIONS

The main contributions from this research are as follows:

1) A novel technique was developed to measure the uncertainties associated with source localization. An effective coefficient (EC) was proposed which evaluates similarity of AE signals using cross-correlation technique. The most likely EC values were determined using Bayesian estimation having as prior information the artificial signals of cracks. This technique is useful for acoustic emission in the event of large error of source localization.
2) The use of an asymmetric sensor arrangement allowing limitation of arrival time for source localization that can be segregated around the weld regions. The AE sensors set up is useful in monitoring vibration problem since the high levels of acceleration for pipes during vibrations can make different areas difficult to access for measurements, creating problems for sensor attachment and personnel safety. Therefore the proposed methods used in this research can be used in real application to assess the condition of the welds subjected to any type of damage not limited to fatigue cracks.

3) A novel method was developed to assess damage severity for plate analysis. A damage sensitive feature α was proposed which manipulates symmetry S_0 and asymmetry A_0 modes of Lamb waves. This feature is basically a parameter less than unity which decreases as crack depth increases. Negative α means the crack has propagated over 90% thickness. The feature was validated numerically.
4) A non-standard vibration-induced fatigue test for simple plate geometry was designed using both experimental testing and numerical simulations. The methodology allowed to reduce noise level below 40dB, which is crucial in wave mode identification. The setup can be used to study Acoustic Emission signals generated in the early stage of damage such as dislocation of slip bands prior to micro/macro fracture or crack initiation.
5) The accuracy of source localization using a Single Sensor Modal Analysis Localization (SSMAL) was improved using a cross-correlation methodology with Gaussian modulated cosine signals. The dispersion of A_0 was reduced using signal enveloping. This method eliminates for this specific study, the error of the calculated time difference between the S_0 and A_0
6) A methodology to carry out acoustic emission monitoring for resonance fatigue test of a large pipe in extreme environment was reported. This includes system and instrumentation setups.
7) The importance of Rayleigh waves in thick pipe and their significance in source localization using high threshold setting was demonstrated.
8) Wave propagation analysis in finite element using node release method to allow crack extension through thickness in pre-stressed structure was reported. The signals obtained has been successfully correlated with the actual signals of cracks

A number of papers have been published from the outputs of the present research;

1) Shamsudin, M. F., Mares, C., Johnston, C., Edwards, G., & Gan, T. -H. Vibration and Acoustic Emission Monitoring of a Girth Weld during a Resonance Fatigue Test. *In 24th International Congress on Sound and Vibration 23-27 July, 2017*. London

2) Shamsudin, M. F., Mares, C., Gan, T. -H., & Edwards, G. (2017). Bayesian Estimation for Crack Monitoring of a Resonant Pipe using Acoustic Emission Method. *In International Conference on Structural Engineering Dynamics*. Ericeira, Portugal
3) Shamsudin, M. F., Mares, C., Gan, T. -H., & Edwards, G. The Application of Bayesian Estimation for Structural Health Monitoring of Fatigue Crack in a Welded Steel Pipe. *Journal of Mechanical System and Signal Processing(accepted)*

6.3 RECOMMENDATION FOR FUTURE WORKS

A number of future steps such as improvement of the current acoustic emission monitoring setup for the resonance fatigue test can be done. It is learnt that high acceleration vibration caused problems to mount AE sensors. One of the solutions is to design a dedicated sensor mount so that the sensors can be placed close to the weld. The mount has to be fixed directly to the pipe to avoid displacement of sensors during fatigue test. This arrangement is expected to improve cross-correlation of signals and hence higher EC values related to cracks occurrence could be obtained. This allows different parameters derivable from signals that are associated with different types of damages and noises. Multiple Bayesian models can be used to predict these parameters. Therefore model selection of different scenarios can be studied such as using such Bayesian Model Averaging (BMA) to select the best model for a particular dataset. The advantage of having multiple models is that it can provide adequate description of distribution of the observed data. The analysis of EC is useful to measure the uncertainties associated with source localization. This parameter can be used as an additional feature to quantify the uncertainty of the located events in conjunction with the standard AE features. In another separate study, wave mode identification using cross-correlation with Gaussian modulated cosine signals was proven useful for thin plates damage detection. This method can also be applied to analyze wave propagation on thick pipe. However to clearly identify the fundamental waves in any thick structure, low resonant frequency sensors are required. This increases complexity of continuous monitoring in extreme test

condition; low frequency noises from the surrounding will be recorded as well, which may result in large data and hence requiring in-depth analysis. The non-standard experimental setup using elastodynamic shaker shows a promising avenue for early stage of fatigue damage identification. It was noted that the study related to the movement of slip bands and dislocation in fatigue receive less attention due to noise from surroundings. Using the current setup, the noise could be reduced to as low as 30dB during fatigue testing. The analysis of damage sensitive feature of various crack depths was shown to be useful for the damage detection analysis. The study can be extended using regression or classification of the calculated coefficients/features and establish the threshold for damage detection. One of the advantage of using regression and classification for the current experiment is that the training data is already available. The test could be repeated for different crack modes and validated with correlated finite element models. A fusion of information can be made with vibration data such that as using the rate of natural frequency change over time with the rate of change of proposed features. This provides multitudes of information to better characterize the damage mechanisms if random vibrations are studied.

BIBLIOGRAPHY

[1] Health & Safety Executive, "Offshore Hydrocarbon Releases Statistics And Analysis," Health & Safety Executive, 2003.

[2] *https://www.hse.gov.uk/hcr3/report/graphs_public.asp, accessed on 1 June 2016*. .

[3] Energy Institute, "Guidelines of the Avoidance of Vibration Induced Fatigue Failure in Process Pipework," Second edition, 2003.

[4] Marine Technology Directorate, "Guidelines for the Avoidance of vibration Induced Fatigue in Process Pipework," MTD Publication 99/100, 1999.

[5] D. N. Veritas, "Fatigue design of offshore steel structures," *No. DNV-RP-C203*, 2010.

[6] D. N. Veritas, "Recommended Practice DNV-RP-F204-Riser Fatigue," *Hovik, Norway*, 2005.

[7] N. Veritas, *Free spanning pipelines*. DNV, 2002.

[8] A. M. Moussa and others, "Acoustic-Induced-Vibration Case Study for WDDM Onshore Facilities," *Oil and Gas Facilities*, vol. 2, pp. 47–51, 2013.

[9] *http://www.exponent.com/kielland_platform/, accessed on 4/10/2015*. .

[10] M. Baker and B. Descamps, "Reliability-based methods in the inspection planning of fixed offshore steel structures," *Journal of Constructional Steel Research*, vol. 52, no. 1, pp. 117–131, 1999.

[11] D. Adams, *Health monitoring of structural materials and components: methods with applications*. John Wiley & Sons, 2007, p. 19.

[12] S. W. Doebling, C. R. Farrar, M. B. Prime, and D. W. Shevits, "A summary review of vibration-based damage identification methods," *Shock and vibration digest*, vol. 30, no. 2, pp. 91–105, 1998.

[13] S. W. Doebling, C. R. Farrar, M. B. Prime, and D. W. Shevitz, "Damage identification and health monitoring of structural and mechanical systems from changes in their vibration characteristics: a literature review," Los Alamos National Lab., NM (United States), 1996.

[14] H. Sohn, C. R. Farrar, F. M. Hemez, D. D. Shunk, D. W. Stinemates, B. R. Nadler, and J. J. Czarnecki, *A review of structural health monitoring literature: 1996-2001*. Los Alamos National Laboratory Los Alamos, NM, 2004.

[15] E. P. Carden and P. Fanning, "Vibration based condition monitoring: a review," *Structural health monitoring*, vol. 3, no. 4, pp. 355–377, 2004.

[16] W. Fan and P. Qiao, "Vibration-based damage identification methods: a review and comparative study," *Structural Health Monitoring*, vol. 10, no. 1, pp. 83–111, 2011.

[17] K. Worden and J. Dulieu-Barton, "An overview of intelligent fault detection in systems and structures," *Structural Health Monitoring*, vol. 3, no. 1, pp. 85–98, 2004.

[18] L. Qiao, A. Esmaeily, and H. G. Melhem, "Signal pattern recognition for damage diagnosis in structures," *Computer-Aided Civil and Infrastructure Engineering*, vol. 27, no. 9, pp. 699–710, 2012.

[19] J. Mottershead and M. Friswell, "Model updating in structural dynamics: a survey," *Journal of sound and vibration*, vol. 167, no. 2, pp. 347–375, 1993.

[20] C. Mares, J. Mottershead, and M. Friswell, "Stochastic model updating: part 1—theory and simulated example," *Mechanical Systems and Signal Processing*, vol. 20, no. 7, pp. 1674–1695, 2006.

[21] C. R. Farrar, T. A. Duffey, S. W. Doebling, and D. A. Nix, "A statistical pattern recognition paradigm for vibration-based structural health monitoring," in *2nd International Workshop on Structural Health Monitoring, Stanford, CA*, 1999.

[22] H. Sohn, J. A. Czarnecki, and C. R. Farrar, "Structural health monitoring using statistical process control," *Journal of Structural Engineering*, vol. 126, no. 11, pp. 1356–1363, 2000.

[23] H. Sohn and C. R. Farrar, "Damage diagnosis using time series analysis of vibration signals," *Smart materials and structures*, vol. 10, no. 3, p. 446, 2001.

[24] H. Sohn, K. Worden, and C. R. Farrar, "Statistical damage classification under changing environmental and operational conditions," *Journal of Intelligent Material Systems and Structures*, vol. 13, no. 9, pp. 561–574, 2002.

[25] W. Tang, "Probabilistic updating of flaw information(flaw prediction and control in welds," *Journal of Testing and Evaluation*, vol. 1, pp. 459–467, 1973.

[26] A. B. Thien, H. C. Chiamori, J. T. Ching, J. R. Wait, and G. Park, "The use of macro-fibre composites for pipeline structural health assessment," *Structural control and health monitoring*, vol. 15, no. 1, pp. 43–63, 2008.

[27] S. Dezfouli and A. Zabihollah, "Structural health monitoring of buried pipelines under static dislocation and vibration," in *Mechatronics and Embedded Systems and Applications (MESA), 2010 IEEE/ASME International Conference on*, 2010, pp. 325–329.

[28] J. Out, D. Kronemeijer, P. Van de Loo, and A. De Sterke, "The integrity of flexible pipe: search for an inspection strategy," *Engineering structures*, vol. 17, no. 4, pp. 305–314, 1995.

[29] R. Jacques, T. Clarke, S. Morikawa, and T. Strohaecker, "Monitoring the structural integrity of a flexible riser during dynamic loading with a combination of non-destructive testing methods," *NDT & E International*, vol. 43, no. 6, pp. 501–506, 2010.

[30] T. Clarke, R. Jacques, A. Bisognin, C. Camerini, S. Damasceno, and T. Strohaecker, "Monitoring the structural integrity of a flexible riser during a full-scale fatigue test," *Engineering Structures*, vol. 33, no. 4, pp. 1181–1186, 2011.

[31] A. G. Beatie, "Acoustic Emission Non-Destructive Testing of Structures using Source Location Techniques," Sandia National Laboratories, 2013.

[32] J. Kaiser, "Untersuchung über das Auftreten von Geräuschen beim Zugversuch (A study of Acoustic Phenomena in Tensile Tests), Ph.D Thesis," Technische Hochschule, Munich, Germany, 1950.

[33] H. M. Tensi, "The Kaiser-effect and its scientific background," in *26th European conference on acoustic emission testing*, 2004, pp. 31–42.

[34] T. Drouillard, "A history of acoustic emission," *Journal of acoustic emission*, vol. 14, no. 1, pp. 1–34, 1996.

[35] K. ONO, H. CHO, and M. Takuma, "THE ORIGIN OF CONTINUOUS EMISSIONS," *Journal of Acoustic Emission*, vol. 23, p. 206, 2005.

[36] K. Ono and M. Ohtsu, "A generalized theory of acoustic emission and Green's functions in a half space," *Journal of Acoustic Emission*, vol. 3, pp. 27–40, 1984.

[37] ASTM, "Standard for Leak Detection and Location using Surface-Mounted Acoustic Emission Sensors, E1211-02," ASTM International, Book of Standards Vol. 03.03.

[38] ASTM, "Standard Practice for Continuous Monitoring of Acoustic Emission from Metal Pressure Boundaries, E1139-02," ASTM International, Book of Standards Vol. 03.03.

[39] American Society for Non-destructive Testing, *Acoustic Emission Testing*. NDT Handbook, Third Edition, Vol. 6, 2005.

[40] K. M. Holford and D. Carter, "Acoustic emission source location," *Key Engineering Materials*, vol. 167, pp. 162–171, 1999.

[41] H. Dunegan, "Modal analysis of acoustic emission signals," *Journal of Acoustic emission*, vol. 15, pp. 53–61, 1997.

[42] M. R. Gorman and W. H. Prosser, "AE source orientation by plate wave analysis," *J. Acoust. Soc. Am.*, vol. 90, 1991.

[43] M. G. Baxter, R. Pullin, K. M. Holford, and S. L. Evans, "Delta T source location for acoustic emission," *Mechanical systems and signal processing*, vol. 21, no. 3, pp. 1512–1520, 2007.

[44] *http://www.vallen.de/downloads*. .

[45] E. Wolf, "Fatigue crack closure under cyclic tension," *Engineering Fracture Mechanics*, vol. 2, no. 1, pp. 37–45, 1970.

[46] M. Lysak, "Development of the theory of acoustic emission by propagating cracks in terms of fracture mechanics," *Engineering fracture mechanics*, vol. 55, no. 3, pp. 443–452, 1996.

[47] C. Heiple and S. Carpenter, "Acoustic emission produced by deformation of metals and alloys-A review.," *Journal of Acoustic Emission*, vol. 6, pp. 177–204, 1987.

[48] T. Lindley, I. Palmer, and C. Richards, "Acoustic emission monitoring of fatigue crack growth," *Materials Science and Engineering*, vol. 32, no. 1, pp. 1–15, 1978.

[49] S. Smith and T. Morton, "Acoustic-emission detection techniques for high-cycle-fatigue testing," *Experimental Mechanics*, vol. 13, no. 5, pp. 193–198, 1973.

[50] Q. Ai, C.-X. Liu, X.-R. Chen, P. He, and Y. Wang, "Acoustic emission of fatigue crack in pressure pipe under cyclic pressure," *Nuclear Engineering and Design*, vol. 240, no. 10, pp. 3616–3620, 2010.

[51] W. G. Byers, M. J. Marley, J. Mohammadi, R. J. Nielsen, and S. Sarkani, "Fatigue reliability reassessment procedures: state-of-the-art paper," *Journal of Structural Engineering*, 1997.

[52] H. Dunegan, D. Harris, and C. Tatro, "Fracture analysis by use of acoustic emission," *Engineering Fracture Mechanics*, vol. 1, no. 1, pp. 105–122, 1968.

[53] J. Masounave, J. Lanteigne, M. Bassim, and D. Hay, "Acoustic emission and fracture of ductile materials," *Engineering Fracture Mechanics*, vol. 8, no. 4, pp. 701–709, 1976.

[54] W. H. Prosser, "Advanced AE techniques in composite materials research," 1996.

[55] D. G. Aggelis, E. Z. Kordatos, and T. E. Matikas, "Acoustic emission for fatigue damage characterization in metal plates," *Mechanics Research Communications*, vol. 38, pp. 106–110, 2011.

[56] P. Paris and F. Erdogan, "A critical analysis of crack propagation laws," *Journal of Fluids Engineering*, vol. 85, pp. 528–533, 1963.

[57] M. Bassim, "Detection of fatigue crack propagation with acoustic emission," *NDT & E International*, vol. 25, no. 6, pp. 287–289, 1992.

[58] T. Roberts and M. and Talebzadeh, "Acoustic emission monitoring of fatigue crack propagation," *Journal of Constructional Steel Research*, vol. 59, no. 6, pp. 695–712, 2003.

[59] T. Roberts and M. Talebzadeh, "Fatigue life prediction based on crack propagation and acoustic emission count rates," *Journal of Constructional Steel Research*, vol. 59, no. 6, pp. 679–694, 2003.

[60] C. R. Farrar and N. A. Lieven, "Damage prognosis: the future of structural health monitoring," *Philosophical Transactions of the Royal Society of London A: Mathematical, Physical and Engineering Sciences*, vol. 365, no. 1851, pp. 623–632, 2007.

[61] B. A. Zárate, J. M. Caicedo, J. Yu, and P. Ziehl, "Probabilistic prognosis of fatigue crack growth using acoustic emission data," *Journal of Engineering Mechanics*, vol. 138, no. 9, pp. 1101–1111, 2012.

[62] A. Carpinteri, G. Lacidogna, and N. Pugno, "Structural damage diagnosis and life-time assessment by acoustic emission monitoring," *Engineering Fracture Mechanics*, vol. 74, no. 1, pp. 273–289, 2007.

[63] Y. Ling and S. Mahadevan, "Integration of structural health monitoring and fatigue damage prognosis," *Mechanical Systems and Signal Processing*, vol. 28, pp. 89–104, 2012.

[64] B. A. Zárate, J. M. Caicedo, J. Yu, and P. Ziehl, "Probabilistic prognosis of fatigue crack growth using acoustic emission data," *Journal of Engineering Mechanics*, vol. 138, no. 9, pp. 1101–1111, 2012.

[65] A. Rytter, "Vibrational Based Inspection of Civil Engineering Structures," Ph. D. Dissertation, Department of Building Technology and Structural Engineering, Aalborg University, Denmark, 1993.

[66] J. Gary and M. A. Hamstad, "On the far-field structure of waves generated by a pencil lead break on a thin plate," *Journal of acoustic emission*, vol. 12, no. 3–4, pp. 157–170, 1994.

[67] M. Hamstad, "Acoustic emission source location in a thick steel plate by Lamb modes," *Journal of acoustic emission*, vol. 25, pp. 194–214, 2007.

[68] M. A. Hamstad, "SOME OBSERVATIONS ON RAYLEIGH WAVES AND ACOUSTIC EMISSION IN THICK STEEL PLATES.," *Journal of Acoustic Emission*, vol. 27, 2009.

[69] M. Hamstad, J. Gary, and A. O'GALLAGHER, "Far-field acoustic emission waves by three-dimensional finite element modeling of pencil-lead breaks on a thick plate," *Journal of acoustic emission*, vol. 14, no. 2, pp. 103–114, 1996.

[70] K. F. Graff, *Wave motion in elastic solids*. Courier Corporation, 2012, p. 6.

[71] S. Stein and M. Wysession, "An introduction to seismology, earthquakes, and earth structure," 2003.

[72] Lord Rayleigh, "On waves propagated along the plane surface of an elastic solid," *Proceedings of the London Mathematical Society*, vol. 1, no. 1, pp. 4–11, 1885.

[73] J. L. Rose, *Ultrasonic Guided Waves in Solid Media*. Cambridge University Press, 2014.

[74] H. Lamb, "On waves in an elastic plate," *Proceedings of the Royal Society of London. Series A, Containing papers of a mathematical and physical character*, pp. 114–128, 1917.

[75] S. Sorohan, N. Constantin, M. Găvan, and V. Anghel, "Extraction of dispersion curves for waves propagating in free complex waveguides by standard finite element codes," *Ultrasonics*, vol. 51, pp. 503–515, 2011.

[76] B. Alzahabi, "Non-uniqueness in cylindrical shells optimization," *Advances in Engineering Software*, vol. 36, no. 9, pp. 584–590, 2005.

[77] H. Yun and W. Zhang, "Damage detection based on the propagation of longitudinal guided wave in a bimetal composite pipe," *Theoretical and Applied Mechanics Letters*, vol. 1, no. 2, p. 021004, 2011.

[78] M. Silk and K. Bainton, "The propagation in metal tubing of ultrasonic wave modes equivalent to Lamb waves," *Ultrasonics*, vol. 17, no. 1, pp. 11–19, 1979.

[79] P. Cawley and R. Adams, "The location of defects in structures from measurements of natural frequencies," *The Journal of Strain Analysis for Engineering Design*, vol. 14, no. 2, pp. 49–57, 1979.

[80] P. Cawley and D. Alleyne, "The use of Lamb waves for the long range inspection of large structures," *Ultrasonics*, vol. 34, no. 2–5, pp. 287–290, 1996.

[81] R. Dalton, P. Cawley, and M. Lowe, "Propagation of acoustic emission signals in metallic fuselage structure," in *Science, Measurement and Technology, IEE Proceedings-*, 2001, vol. 148, no. 4, pp. 169–177.

[82] P. Cawley, M. Lowe, D. Alleyne, B. Pavlakovic, and P. Wilcox, "Practical long range guided wave inspection-applications to pipes and rail," *Mater. Eval*, vol. 61, no. 1, pp. 66–74, 2003.

[83] D. Worlton, "Experimental confirmation of Lamb waves at megacycle frequencies," *Journal of Applied Physics*, vol. 32, no. 6, pp. 967–971, 1961.

[84] I. A. Victorov, *Rayleigh and Lamb Waves, Physical Theory and Applications*. 1967.

[85] M. J. Lowe, "Matrix techniques for modeling ultrasonic waves in multilayered media," *IEEE transactions on ultrasonics, ferroelectrics, and frequency control*, vol. 42, no. 4, pp. 525–542, 1995.

[86] I. Bartoli, A. Marzani, F. L. di Scalea, and E. Viola, "Modeling wave propagation in damped waveguides of arbitrary cross-section," *Journal of Sound and Vibration*, vol. 295, no. 3, pp. 685–707, 2006.

[87] M. Åberg and P. Gudmundson, "The usage of standard finite element codes for computation of dispersion relations in materials with periodic microstructure," *The Journal of the Acoustical Society of America*, vol. 102, no. 4, pp. 2007–2013, 1997.

[88] F. Moser, L. J. Jacobs, and J. Qu, "Modeling elastic wave propagation in waveguides with the finite element method," *Ndt & E International*, vol. 32, no. 4, pp. 225–234, 1999.

[89] B. Pavlakovic, M. Lowe, D. Alleyne, and P. Cawley, "Disperse: a general purpose program for creating dispersion curves," in *Review of progress in quantitative nondestructive evaluation*, Springer, 1997, pp. 185–192.

[90] B. P. Michael Lowe, *DISPERSE*, 2.0.20a ed. Non-Destructive Testing Laboratory, Department of Mechanical Engineering, Imperial Colleage London, 2013.

[91] A. A. Pollock, "Classical wave theory in practical AE testing," *Progress in Acoustic Emission III-JAP Society of Non-Destructive Testing*, pp. 708–721, 1986.

[92] A. Graps, "An introduction to wavelets," *IEEE computational science and engineering*, vol. 2, no. 2, pp. 50–61, 1995.

[93] M. Vetterli and C. Herley, "Wavelets and filter banks: Theory and design," *IEEE transactions on signal processing*, vol. 40, no. 9, pp. 2207–2232, 1992.

[94] G. Strang, "Wavelets," *American Scientist*, vol. 82, no. 3, pp. 250–255, 1994.

[95] I. Daubechies, *Ten lectures on wavelets*. SIAM, 1992.

[96] A. Haar, "Zur theorie der orthogonalen funktionensysteme," *Mathematische Annalen*, vol. 69, no. 3, pp. 331–371, 1910.

[97] H. Suzuki, T. Kinjo, Y. Hayashi, M. Takemoto, K. Ono, and Y. Hayashi, "Wavelet transform of acoustic emission signals," *Journal of Acoustic Emission*, vol. 14, pp. 69–84, 1996.

[98] A. C. Okafor, K. Chandrashekhara, and Y. Jiang, "Location of impact in composite plates using waveform-based acoustic emission and Gaussian cross-correlation techniques," in *1996 Symposium on Smart Structures and Materials*, 1996, pp. 291–302.

[99] S. M. Ziola and M. R. Gorman, "Source location in thin plates using cross-correlation," *The Journal of the Acoustical Society of America*, vol. 90, no. 5, pp. 2551–2556, 1991.

[100] *Acoustic Emission Sensors,Released 12-2012, Vallen Systeme*. .

[101] C. U. Grosse, H. W. Reinhardt, and F. Finck, "Signal-based acoustic emission techniques in civil engineering," *Journal of materials in civil engineering*, vol. 15, no. 3, pp. 274–279, 2003.

[102] E. P. Carden and J. M. Brownjohn, "ARMA modelled time-series classification for structural health monitoring of civil infrastructure," *Mechanical systems and signal processing*, vol. 22, no. 2, pp. 295–314, 2008.

[103] C. Huang, S. Hung, C. Lin, and W. Su, "A Wavelet-Based Approach to Identifying Structural Modal Parameters from Seismic Response and Free Vibration Data," *Computer-Aided Civil and Infrastructure Engineering*, vol. 20, no. 6, pp. 408–423, 2005.

[104] J.-T. Kim, Y.-S. Ryu, H.-M. Cho, and N. Stubbs, "Damage identification in beam-type structures: frequency-based method vs mode-shape-based method," *Engineering structures*, vol. 25, no. 1, pp. 57–67, 2003.

[105] J. B. Kosmatka and J. M. Ricles, "Damage detection in structures by modal vibration characterization," *Journal of Structural Engineering*, vol. 125, no. 12, pp. 1384–1392, 1999.

[106] C.-P. Fritzen, D. Jennewein, and T. Kiefer, "Damage detection based on model updating methods," *Mechanical systems and signal processing*, vol. 12, no. 1, pp. 163–186, 1998.

[107] C. Mares, B. Dratz, J. Mottershead, and M. Friswell, "Model updating using Bayesian estimation," in *International Conference on Noise and Vibration Engineering, ISMA2006, Katholieke Universiteit Leuven*, 2006, pp. 18–20.

[108] J. E. Mottershead, M. Link, and M. I. Friswell, "The sensitivity method in finite element model updating: a tutorial," *Mechanical systems and signal processing*, vol. 25, no. 7, pp. 2275–2296, 2011.

[109] T. A. Netto, M. Lourenco, and A. Botto, "Fatigue performance of pre-strained pipes with girth weld defects: Full-scale experiments and analyses," *International Journal of Fatigue*, vol. 30, no. 5, pp. 767–778, 2008.

[110] J. Van Wittenberghe, P. De Baets, W. De Waele, W. Ost, M. Verstraete, and S. Hertelé, "Resonant bending fatigue test setup for pipes with optical displacement measuring system," *Journal of Offshore Mechanics and Arctic Engineering*, vol. 134, no. 3, p. 031702, 2012.

[111] *Non-destructive testing. Terminology. Terms used in acoustic emission testing*. BS EN 1330-9:2009.

[112] M. Bassim, S. S. Lawrence, and C. Liu, "Detection of the onset of fatigue crack growth in rail steels using acoustic emission," *Engineering Fracture Mechanics*, vol. 47, no. 2, pp. 207–214, 1994.

[113] P. Vanniamparambil, U. Guclu, and A. Kontsos, "Identification of crack initiation in aluminium alloys using acoustic emission," *Experimental Mechanics*, vol. 55, no. 5, pp. 837–850, 2015.

[114] Y. MURAKAMI, "RECORDER (MINI-RAINFLOW CORDER) AND APPLICATION TO FATIGUE DESIGN OF CAR WHEELS," *Fatigue Design and Reliability*, vol. 23, p. 135, 1999.

[115] A. S. J. Swamidas and Y. Chen, "Monitoring Crack Growth Through Change of Modal Parameters," *Journal of Sound and Vibration*, vol. 186, pp. 325–343, 1995.

[116] A. S. J. S. Yin Chen, "Change of modal parameters due to crack growth in a tripod tower platform," *Canadian Journal of Civil Engineering*, vol. 20, pp. 801–813, 1993.

[117] H. Cui, X. Xu, W. Peng, Z. Zhou, and M. Hong, "A damage detection method based on strain modes for structures under ambient excitation," *Measurement*, vol. 125, pp. 438–446, 2018.

[118] Z. Zhang, "Strain modal analysis and fatigue residual life prediction of vibrating screen beam," *Journal of Measurements in Engineering*, vol. 4, no. 4, pp. 217–223, 2016.

[119] G. Pavi, "Measurement of vibrations by strain gauges, Part I: theoretical basis," *Journal of Sound and vibration*, vol. 102, no. 2, pp. 153–163, 1985.

[120] G. Pavi, "Measurement of vibrations by strain gauges, Part II: Selection of measurement parameters," *Journal of Sound and Vibration*, vol. 102, no. 2, pp. 165–188, 1985.

[121] E. J. Wilson, "Strain-gage Instrumentation," *Harris' Shock and Vibration Handbook, S*, pp. 17–1, 1976.

[122] S. Loutridis, E. Douka, and L. Hadjileontiadis, "Forced vibration behaviour and crack detection of cracked beams using instantaneous frequency," *Ndt & E International*, vol. 38, no. 5, pp. 411–419, 2005.

[123] A. Pollock, "Critical AE Problems for the Researcher," *Journal of Acoustic Emission*, vol. 9(2), pp. 140–141, 1990.

[124] F. J. Harris, "On the use of windows for harmonic analysis with the discrete Fourier transform," *Proceedings of the IEEE*, vol. 66, no. 1, pp. 51–83, 1978.

[125] J. L. Beck and S.-K. Au, "Bayesian updating of structural models and reliability using Markov chain Monte Carlo simulation," *Journal of Engineering Mechanics*, vol. 128, no. 4, pp. 380–391, 2002.

[126] J. L. Beck and L. S. Katafygiotis, "Updating models and their uncertainties. I: Bayesian statistical framework," *Journal of Engineering Mechanics*, vol. 124, no. 4, pp. 455–461, 1998.

[127] A. Rao, "Acoustic emission and signal analysis," *Defence Science Journal*, vol. 40, no. 1, p. 55, 1990.

[128] M. Shehadeh, J. Steel, and R. Reuben, "Acoustic emission source location for steel pipe and pipeline applications: the role of arrival time estimation," *Proceedings of the Institution of Mechanical Engineers, Part E: Journal of Process Mechanical Engineering*, vol. 220, no. 2, pp. 121–133, 2006.

[129] W. K. Hastings, "Monte Carlo sampling methods using Markov chains and their applications," *Biometrika*, vol. 57, no. 1, pp. 97–109, 1970.

[130] N. Metropolis and S. Ulam, "The monte carlo method," *Journal of the American statistical association*, vol. 44, pp. 335–341, 1949.

[131] D. J. Lunn, A. Thomas, N. Best, and D. Spiegelhalter, "WinBUGS-a Bayesian modelling framework: concepts, structure, and extensibility," *Statistics and computing*, vol. 10, no. 4, pp. 325–337, 2000.

[132] S. Geman and D. Geman, "Stochastic relaxation, Gibbs distributions, and the Bayesian restoration of images," *Pattern Analysis and Machine Intelligence, IEEE Transactions on*, no. 6, pp. 721–741, 1984.

[133] E. I. George and R. E. McCulloch, "Variable selection via Gibbs sampling," *Journal of the American Statistical Association*, vol. 88, no. 423, pp. 881–889, 1993.

[134] M. R. Kaphle, A. Tan, D. Thambiratnam, and T. H. Chan, "Damage quantification techniques in acoustic emission monitoring," 2011.

[135] M. Huang, L. Jiang, P. K. Liaw, C. R. Brooks, R. Seeley, and D. L. Klarstrom, "Using acoustic emission in fatigue and fracture materials research," *JOM 50.11*, vol. 1–14, 1998.

[136] R. O. Ritchie, "Mechanisms of fatigue-crack propagation in ductile and brittle solids," *International Journal of Fracture*, vol. 100, no. 1, pp. 55–83, 1999.

[137] W. Thomson, *Theory of vibration with applications*. CRC Press, 1996.

[138] C. M. Harris, *Harris' Shock and Vibration Handbook*. Mcgraw-Hill, pp. 21.1–21.72.

[139] W. Thomson, *Theory of Vibrations with Applications, fifth Edition*. Pearson Education, 1997.

[140] A. K. Chopra, *Dynamics of structures: theory and applications to earthquake engineering. 2007*. Prentice-Hall, 2007.

[141] A. Karolczuk, M. Kurek, and T. Lagoda, "Fatigue life of aluminium alloy 6082 t6 under constant and variable amplitude bending with torsion," *Journal of Theoretical and Applied Mechanics*, vol. 53, 2015.

[142] W. D. Pilkey and D. F. Pilkey, *Peterson's stress concentration factors*. John Wiley & Sons, 2008.
[143] G. R. Irwin, "Analysis of stresses and strains near the end of a crack traversing a plate," *Spie Milestone series MS*, vol. 137, no. 167–170, p. 16, 1997.
[144] B. S. BS7910, "Guidance on methods for assessing the acceptability of flaws in metallic structures," British Standards Institution, 2005.
[145] *Section 11.4.2 Contour integral evaluation of the Abaqus 6.14 Analysis User's Guide*. .
[146] S. Missori and A. Sili, "Mechanical behaviour of 6082-T6 aluminium alloy welds," *Metallurgical Science and Tecnology*, vol. 18, no. 1.
[147] M. G. Sause, "Investigation of pencil-lead breaks as acoustic emission sources.," *Journal of Acoustic Emission*, vol. 29, 2011.
[148] M. Hamstad, "Acoustic emission signals generated by monopole (pencil lead break) versus dipole sources: finite element modeling and experiments," *Journal of Acoustic Emission*, vol. 25, pp. 92–106, 2007.
[149] W. Prosser, M. Hamstad, J. Gary, and A. O'gallagher, "Finite element and plate theory modeling of acoustic emission waveforms," *Journal of Nondestructive Evaluation*, vol. 18, no. 3, pp. 83–90, 1999.
[150] M. A. Hamstad, A. O'Gallagher, and J. M. Gary, "Modeling of buried monopole and dipole sources of acoustic emission with a finite element technique," *Journal of acoustic emission*, vol. 17, no. Journal of Acoustic Emission, 1999.
[151] C. Lee, J. J. Scholey, P. D. Wilcox, M. Wisnom, M. I. Friswell, and B. Drinkwater, "Guided wave acoustic emission from fatigue crack growth in aluminium plate," in *Advanced Materials Research*, 2006, vol. 13, pp. 23–28.
[152] PHYSICAL ACOUSTIC CORPORATION, NANO30 Sensor, Product Datasheet. .
[153] PCB PIEZOTRONICS Model 66212ANZ1 ICP® TO-5 Accelerometer Installation and Operating Manual. .
[154] PCB PIEZOTRONICS Model 086C03 ICP® Impact Hammer Installation and Operating Manual. .

APPENDIX A

EQUIPMENT AND SENSORS

A.1 AE SENSORS

A.1.1 NANO30

The AE sensor of NANO30 is manufactured by Physical Acoustics Corporation (PAC). The sensitivity curves of the sensor are given in A.1 and the details of the sensor specifications are given in Table A.1 [152].

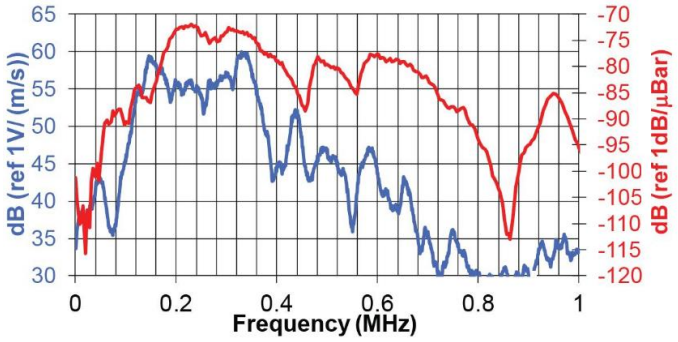

Figure A.1 shows NANO30 sensitivity curves [152]

Peak Sensitivity, Ref V/ms^{-1} (dB)	62
Peak Sensitivity, Ref $V/\mu bar$ (dB)	-72
Resonance Frequency V/ms^{-1} (KHz)	140
Resonance Frequency $V/\mu bar$ (KHz)	300
Freq. Range (KHz)	125 – 750

Table A.1 NANO30 sensor specifications

A.1.2 VS900-RIC

The VS900-RIC sensor is manufactured by Vallen Systeme. The sensitivity curves of the sensor are given in Figure A.2 and the details of the sensor specifications are given in Table A.2 [100].

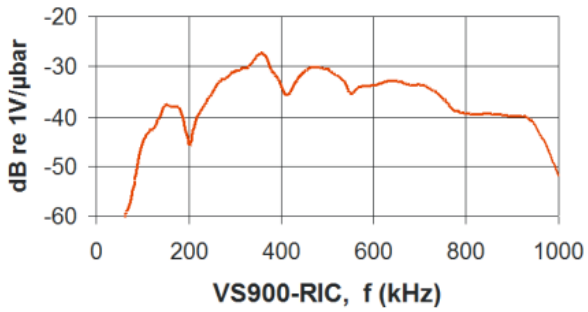

Figure A.2 show the VS900-RIC sensitivity curves [100]

Peak Sensitivity, Ref $V/\mu bar$ (dB)	-28
Resonance Frequency $V/\mu bar$ (KHz)	350
Freq. Range (KHz)	100 – 900
Weight	

Table A.2 VS900-RIC sensor specifications

A.2 ACCELEROMETERS

A.2.1 66212ANZ1

The 66212ANZ1 is manufactured by IMISENSORS. The specifications of the sensors are given in Table A.3.

Sensitivity $\pm 20\%$ (mV/ms^{-2})	1.02
Measurement Range (ms^{-2})	± 490

Frequency Range $\pm 30dB$ (Hz)	0.5 to 10,000
Resonant Frequency (KHz)	25

Table A.3 66212ANZ1 accelerometer specifications [153]

A.3 IMPACT HAMMER

A.3.1 086C03

The transient load is excited by an impact hammer manufactured by PCB PIEZOTRONICS. The specification is given in Table A.4 and the sensitivity curves is shown in Figure A.3.

Sensitivity $\pm 15\%$ (mV/N)	2.25
Measurement Range (N)	± 2224 N pk
Resonant Frequency (KHz)	22

Table A.4 Impact hammer specification

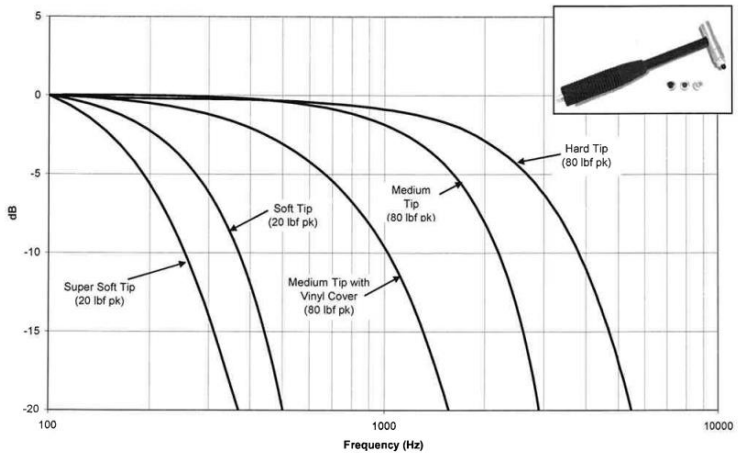

Figure A.3 Impact hammer sensitivity curves [154]